Technische Universität München
Physik-Department
Chemische Physik fern vom Gleichgewicht

Self-organization phenomena during the electrodissolution of silicon

Dissertation
Konrad Schönleber

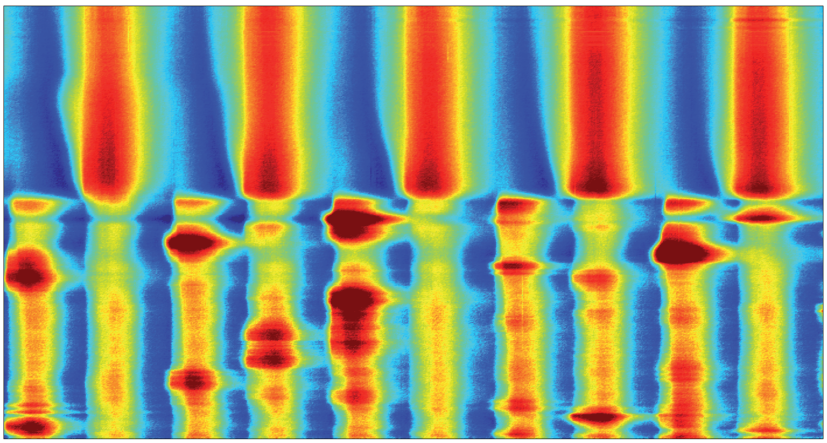

Dezember 2015

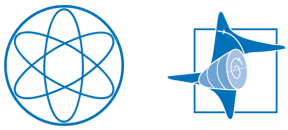

Technische Universität München
Physik-Department
E19a - Chemische Physik fern vom Gleichgewicht

Self-organization phenomena during the electrodissolution of silicon

Konrad Schönleber

Vollständiger Abdruck der von der Fakultät für Physik der Technischen Universität München zur Erlangung des akademischen Grades eines

Doktors der Naturwissenschaften (Dr. rer. nat.)

genehmigten Dissertation.

Vorsitzender: Univ.-Prof. Dr. M. Zacharias

Prüfer der Dissertation:

1. Univ.-Prof. Dr. K. Krischer
2. Univ.-Prof. Dr. M. Stutzmann
3. Prof. Dr. O. Steinbock, Florida State University/USA (schriftliche Beurteilung)

Die Dissertation wurde am 03.09.2015 bei der Technischen Universität München eingereicht und durch die Fakultät für Physik am 16.12.2015 angenommen.

Danksagung

An erster Stelle geht mein besonderer Dank an Prof. Dr. Katharina Krischer dafür, dass sie mir ermöglicht hat, an zwei hoch interessanten Forschungsthemen zu arbeiten. Dies sowohl an einem Thema, von dem ich bereits wusste, dass es mir gefallen würde, als auch an einem, von dem nur sie das wusste. In meiner gesamten Zeit hatte sie stets ein offenes Ohr und hilfreiche Anregungen und hat in vielen anregenden Diskussionen mein wissenschaftliches Verständnis stark verbreitert und bereichert. Nicht zuletzt war auch die Möglichkeit, ein Lehrbuch mit ihr zusammen zu schreiben, eine sehr wertvolle und spannende Erfahrung. Lennart Schmidt möchte ich für die enge und fruchtvolle Zusammenarbeit danken. Seine theoretischen Ergebnisse haben entscheidend geholfen, meine experimentellen Ergebnisse in einen größeren Zusammenhang einzuordnen. Weiterhin danke ich Carla Zensen, Maximilian Patzauer, Andreas Heinrich, Felix Kemeth, Elmar Mitterreiter, Martin Wiegand, Irene Grill und Michael Bohrmann für die schöne und anregende gemeinsame Arbeit inner- und außerhalb ihrer Abschlussarbeiten. Qi Li, Simon Filser und Dr. Katrin Bickel möchte ich für die lange, intensive und gute Zusammenarbeit und das Aufpassen auf mein Herzensthema danken. Für seine stete Hilfsbereitschaft möchte ich mich bei Philipp Bauer bedanken. Weiterhin danke ich allen Kollegen, mit denen ich das Vergnügen hatte, im Laufe der Jahre in unserer Arbeitsgruppe zusammenzuarbeiten, für die freundschaftliche und äußerst angenehme Atmosphäre. Meinen Freunden Dr. Karsten Donnay und Severin Benz möchte ich für die spannende gemeinsame Reise durch das Reich der Wissenschaft danken. Meiner Familie, besonders Bodil und Sophie, Friedrich und Felix, danke ich für die unendlich vielen kleinen und großen Freuden, mit denen sie unser gemeinsames Leben erfüllen.

Abstract

In this thesis the oscillatory electrodissolution of silicon is investigated. We systematically study and classify the different types of oscillations and identify high amplitude oscillations in the voltage drop across the electrode as a unified class of oscillations present under potentiostatic, galvanostatic and mixed control. Under appropriate coupling these oscillations then exhibit a rich variety of patterns forming spontaneously in the oxide layer covering the electrode including such complex patterns as 'chimera states', i.e. the coexistence of synchronized and desynchronized regions. We investigate these patterns in detail and, by means of comparing them to theoretical simulations obtained with a generic ansatz, identify them as genuine dynamical phenomena.

Table of Contents

1 Introduction

Das Gebiet, welches der unbedingten Herrschaft der vollendeten Wissenschaft unterworfen werden kann, ist leider sehr eng, und schon die organische Welt entzieht sich ihm größtenteils.

The area which can be fully captured by pure science is unfortunately very narrow and already the organic world is almost fully exempt from it.
(Hermann von Helmholtz)

The scientific understanding of any subject requires some level of categorization, modeling and simplification. Often, the most important part is to distinguish between the relevant parts of a given system, or the model thereof, and the irrelevant ones which can then be followed up by neglecting the latter. This leads many scientists to a philosophy of methodological reductionism which states that the best understanding of a system can be gained by an understanding of its fundamental constituent parts and their basic interactions [1]. There is, however, a very fundamental problem with the idea that methodological reductionism allows for a full understanding of a given system which is captured in the statement by Helmholtz at the beginning of this chapter and was wonderfully laid out in a seminal article by P. W. Anderson [2]. While the study of the fundamental entities of a given system is certainly of interest, there is no guarantee that this will tell the researcher anything meaningful at all about the behavior of this system. This is only true if the system is the mere sum of its parts, i.e. that it is in a sense linear and that thus the superposition principle holds. Instead, for ever larger and larger systems the scientist will encounter new physical laws which emerge due to the scale of the system and the complexity of the relevant interactions and each of these law is, as Anderson puts, it "*... as fundamental as any other*". In this view, there is no hierarchy of the different disciplines of science but each follows its own set of fundamental rules. It is then interesting to consider another type of scientific inquest complementary to the search of fundamental entities at each given level: The study of complex interactions which neglects the exact nature of the constituent parts and considers a higher degree of complexity in their interactions instead. This field of research is called nonlinear dynamics.

A prime example for a theory not understandable without a nonlinear dynamical approach is Darwin´s theory of evolution [3, 4]. Here, from a dynamical point of view, the most important characteristics of the basic constituents, i.e. the individual life forms, is that they are self-replicating agents which achieve this feat in an only almost perfect manner and all other features are neglected [5]. In a large ensemble of these agents then phenomena like diversification and subsequent speciations are found to be outcome of the dynamics of the entire system by the mechanism of 'survival of the fittest'. This mechanism is a dynamical phenomenon and highly nonlinear as it clearly includes self-enhancing effects. Under this nonlinear mechanism then new laws emerge spontaneously. An example is the occurrence of biological niches which in turn seem to impose rather strict rules on how a species occupying this niche should look like as a new law. To envision this, just compare the superficial features of dolphins and other large, carnivore sea-living animals like tuna or between marsupial and eutherian moles.

Despite their vastly different ancestral history these species share central design characteristics which are dictated by the fact that they share a similar biological niche. Note that the individual life forms themselves are also excellent examples for nonlinear, dynamical systems as self-replicating agents necessarily involve auto-catalytic, i.e. self-enhancing, cycles [6].

To proceed in the understanding of many aspects of nature, and to thus overcome the barrier to our scientific knowledge perceived by Helmholtz and also James Clerk Maxwell [7], it is then important to find fundamental laws and principles governing the parts of nonlinear dynamics relevant for natural phenomena. Unfortunately, although this was pointed out almost four decades ago in a widely received article by R. M. May, it is probably still mostly true that the curriculum typically taught in physics '*... ill equips the student to confront the bizarre behavior exhibited by even the simplest of discrete nonlinear systems...*' [8]. Nevertheless, a lot of progress has been made and some parts of it relevant to this work will be briefly discussed in the following.

There are perhaps two main, mutually non-exclusive, lines of inquest into the topic of nonlinear dynamics one starting from thermodynamics and one from pure mathematics. The former can perhaps be best separated again into two broad schools of thought: 'Synergetics' prominently advanced by H. Haken [9] and the Brussels school of thermodynamics most prominently put forth by I. Prigogine [10]. Synergetics focuses on the mechanism how new laws of physics spontaneously emerge from the interaction of many constituents, i.e. how the many body interactions impose rules for all the constituents of the system [11]. The Brussels school of thermodynamics expands the field of thermodynamics to more general, non-equilibrium systems and puts a strong emphasis on dissipative structures, i.e. structures spontaneously forming in a self-organized manner far from equilibrium. For both, the occurrence of instabilities and irreversibilities is crucial to the understanding of the systems described. They are thus building on a notion already put forth by Maxwell in some depth many decades earlier [7, 9, 12]. The second line of inquiry into the topic of nonlinear dynamics starts from a purely mathematical perspective. It was pioneered by H. Poincaré at the beginning of the 20^{th} century and has been greatly helped by the development of computers in recent decades [12, 13]. Again the focal point of the research interest are critical points where the dynamical behavior of a given system changes qualitatively, the so-called bifurcations. The surprising richness of dynamics found in even relatively simple nonlinear systems includes spontaneous pattern formation [14, 15], deterministic chaos [16, 8] or spontaneous synchronization of oscillators [17, 18, 19]. Insights thus gained were then applied to many fields of science such as various aspects of biology [20, 21], the human body [22, 23, 24], neural networks [25], weather and climate [16, 26], the electrical grid and other real world networks [27, 28, 29, 30] or hydrodynamics [31, 32, 11].

For a deeper understanding and also for the development of an improved intuition about complex, nonlinear systems it is very instructive to have experimental model systems which express certain features in a defined way and give hints on the universality of certain phenomena. One class of such systems which play a great role for biological and chemical processes are so-called reaction-diffusion systems. Famous model systems here are the Belousov-Zhabotinsky reaction, an inorganic chemical reaction [33, 34, 35] and the oxidation of CO on Pt surfaces in UHV [36]. Both systems express oscillatory dynamics as well as a rich variety of self-organized pattern formation at appropriate experimental parameters.

In this work we are concerned with the oscillatory electrodissolution of silicon as an electrochemical model system for nonlinear reaction-diffusion dynamics. While this system has

been well known and intensely studied for decades [37, 38], its character as a model system for nonlinear reaction-diffusion systems and rich spatio-temporal dynamics, especially self-organized pattern formation, was only pointed out more recently in our group by Miethe et al. [39, 40]. The present thesis builds upon both the experimental apparatus and key experimental findings from these works. It broadens and structures the initial findings and aims at firmly understanding the silicon electrodissolution system from a nonlinear dynamical point of view.

For an instructive visualization of the thread of this thesis we borrow a qualitative scheme introduced by Prigogine for non-equilibrium thermodynamics [12]. The qualitative changes in the dynamics of a given system are visualized in a sketch reminiscent of a bifurcation diagram. The initial state closest to equilibrium is then the 'thermodynamic branch', i.e. the regime where only linear perturbations from thermodynamic equilibrium are present and the system is thus in a steady-flow equilibrium. In Fig.(1.1) such an illustration is shown for the silicon electrodissolution system.

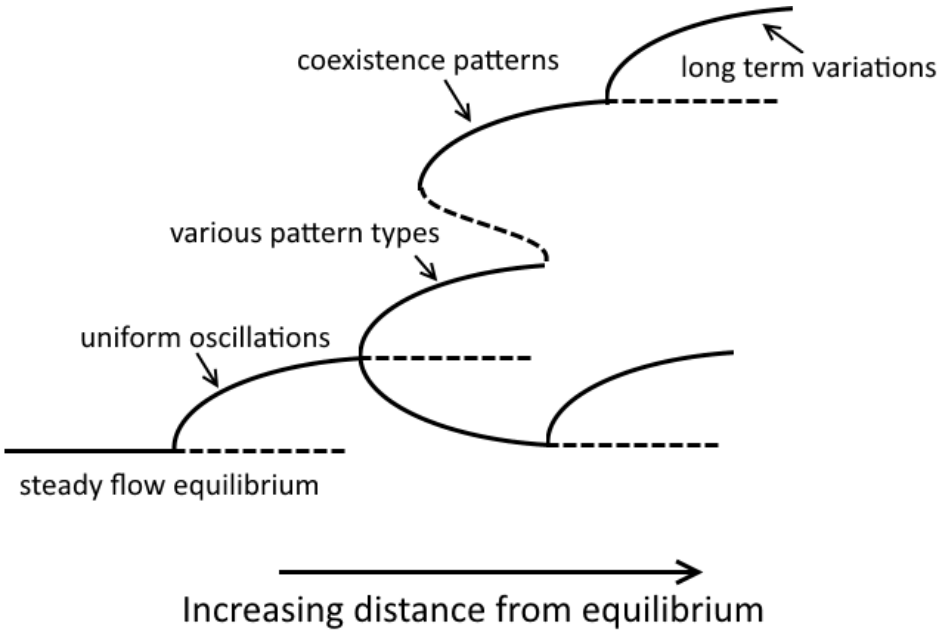

Figure 1.1: Schematic diagram indicating increasing complexity with the distance from equilibrium as the bifurcation parameter as an overview of the different dynamical states encountered throughout this work. Solid lines indicate stable and dashed lines unstable states.

With increasing distance from equilibrium, we identify a stepwise increasing level of complexity of the dynamics in the system which then in turn provide the structure of this work.

In Chap.(2) the electrochemical system, i.e., the anodic (photo-)electrodissolution of silicon and the experimental setups used for its investigation are introduced. Furthermore, data recording and processing are described.

This is followed in Chap.(3) by a description of the spatially uniform dynamics of the system which are experimentally found when p-doped silicon samples or highly illuminated n-doped silicon samples are studied. In Fig.(1.1) this corresponds to a description of the dynamics on the branch denoted 'uniform oscillations'.

Although the oscillatory dynamics during the electrodissolution of silicon have been studied for decades, a mechanism for the basic instability underlying the oscillatory state is still missing. In Chap.(4) requirements for explanations for the occurrence of the oscillations are discussed and a dominant line of explanation often discussed in the literature is falsified. In turn, requirements for a mathematical model capturing the experimental findings are introduced.

In Chap.(5) the effect of type and range of the experimental coupling parameters between the individual points on the electrode surface is presented. In doing so the groundwork for the interpretation of the pattern formation described later is laid.

Chap.(6) is then devoted to the intriguing phenomenon of spontaneous pattern formation encountered in the experiments. It is thus concerned with the branches of higher complexity on the right hand side of Fig.(1.1). Here the patterns are classified and a theoretical interpretation of their occurrence is given. In doing so the specifics of the system are left behind and it is shown to be a potential model system for a variety of dynamical systems.

2 Experimental

In this chapter the experimental system under consideration is presented starting from the general and moving into the particular. In this vein, first, a short, general introduction into semiconductor electrochemistry is given. This is followed by a description of the specific electrochemical system considered, the anodic electrodissolution of silicon. The chapter then finishes with a description of the experimental setups and the data processing employed for its study.

The experimental design was done by Iljana Miethe during her PhD thesis and was mostly in place when this work started [40]. The measurement recording software was written by Andreas Heinrich as part of his Master thesis and the graphical user interface and parts of the MATLAB-code for the data analysis were written by Carla Zensen as a part of her Master thesis [41, 42]. Both works were supervised as part of this work.

2.1 Semiconductor electrochemistry

In electrochemistry charge carrier transfers between an electrode and an electrolyte are considered. In such an electrochemical process the charge carriers in a form mobile in the solid state electrode are interchanged with charge carriers mobile in the electrolyte. The former are typically electrons but, in the case of semiconductors, are sometimes better described as defect electrons or holes, while the latter are solvated ions. The transformation of the charge carrier type is accompanied by a chemical reaction in the electrolyte. If a quantity such as electrostatic potential or current is associated with the emission of a positive charge from the electrode it is called **anodic** while in the opposite case, i.e., when a negative charge is emitted from the electrode it is called **cathodic**. This means that an anodic current is accompanied by the oxidation of some chemical species in the electrolyte and a cathodic current, correspondingly, by a reduction reaction. In short, prototypical reaction schemes for anodic and cathodic reactions involving a chemical species A read:

$$\begin{aligned} \mathrm{A_{red}} &\rightarrow \mathrm{A_{ox}} + e^- \quad \text{anodic} \\ \mathrm{A_{ox}} + e^- &\rightarrow \mathrm{A_{red}} \quad \text{cathodic,} \end{aligned} \tag{2.1}$$

where $\mathrm{A_{ox,red}}$ represent species A in its oxidized and reduced form, respectively. Under equilibrium conditions no net current flows across the interface and the energy gained by transferring a charge carrier into the electrolyte is identical to the energy gained in the inverse process, the transfer of a charge carrier into the electrode.

2.1.1 The electrochemical potential

The energy level of the charge carriers in the electrode at position $\vec{x}$ is given by their electrochemical potential $\widetilde{\mu}(\vec{x})$ which is defined in the following way:

$$\widetilde{\mu}(\vec{x}) = \mu(\vec{x}) + ze\phi(\vec{x}), \tag{2.2}$$

where $\mu(\vec{x})$ is the chemical potential of the charge carriers, $z \in \mathbb{Z}$ the charge number per charge carrier and $\phi(\vec{x})$ the electrostatic potential. In equilibrium the electrochemical potential is constant over any volume provided that the charge carriers can move unhindered. Only in this case is the free energy of the system minimized.

In the bulk of a doped semiconductor the value of the electrochemical potential with respect to the band edges is determined by the doping concentration n_D for electron donors in n-type doping and n_A for electron acceptors in p-type doping, respectively. At a temperature T in the order of room temperature it is then given by:

$$\begin{aligned} \widetilde{\mu} &= E_\mathrm{CB} - kT \cdot \ln\left(\frac{N_\mathrm{C}}{n_\mathrm{D}}\right) \quad ; \quad \mathrm{n-doped} \\ \widetilde{\mu} &= E_\mathrm{VB} + kT \cdot \ln\left(\frac{N_\mathrm{V}}{n_\mathrm{A}}\right) \quad ; \quad \mathrm{p-doped}, \end{aligned} \tag{2.3}$$

where $E_\mathrm{CB,VB}$ are the conduction and valence band edge levels with respect to the vacuum, respectively, $k = 8.617 \cdot 10^{-5}$ eV/K is the Boltzmann constant and $N_\mathrm{C,V}$ are the so-called effective densities of states in the conduction and valence band, respectively. The latter are material specific and independent of the doping level. In the case of silicon they take the values $N_\mathrm{C} = 2.9 \cdot 10^{19}$ cm^{-3} and $N_\mathrm{V} = 3.1 \cdot 10^{19}$ cm^{-3} at room temperature [43]. For an isolated, uncharged piece of silicon the electron affinity, i.e., the position of the conduction band edge with respect to the vacuum level is $E_\mathrm{CB} = -4.0$ eV [44]. At moderate doping levels of $n_\mathrm{D,A} \approx 10^{15}$ cm^{-3} as used in this work this then leads to the following values of the electrochemical potential for n- and p-doped silicon, respectively

$$\begin{aligned} \widetilde{\mu} &\approx -4.3 \text{ eV} \quad ; \quad \mathrm{n-doped} \\ \widetilde{\mu} &\approx -4.8 \text{ eV} \quad ; \quad \mathrm{p-doped}. \end{aligned} \tag{2.4}$$

These values are shifted when any space charge layers with associated drops in the electrostatic potential occur at the interfaces. In this case the bulk of the material has an electrostatic potential ϕ not equal to zero and the band edges shift their absolute energies $E_\mathrm{CB,VB} \to E_\mathrm{CB,VB} - e\phi$. The electrochemical potentials then shift accordingly.

The definition of the electrochemical potential of the transferable charge carriers, e.g., electrons, in the electrolyte requires some more elaboration. The reason for this is that free electrons do not exist in the electrolyte. On the electrolyte side it is therefore necessary to express the energetics of the electrochemical reaction in terms of chemical quantities. In doing so it becomes necessary to introduce another reference point than the vacuum level used in solid states physics. The use of the vacuum level would have the big disadvantage that the solvation process involved in the transfer of the chemical species in question from the vacuum to the location close to the interface in question is rather difficult to handle, both mathematically and experimentally. Typically, the standard hydrogen level is used as a reference energy for the electrochemical potential in the electrolyte instead. With respect to the vacuum level it has a value of -4.4 eV [45, 46]. Introducing this level means that any electron exchanged with the electrode is assumed to stem from the following reaction taking place in a solution of the same solvent:

$$1/2\mathrm{H_2} \to \mathrm{H^+} + e^-, \tag{2.5}$$

with an activity of 1 for both the H_2 gas and the H^+ ions. The original electrochemical reaction is thereby formally replaced by the following reaction:

$$A_{ox} + e^- \rightleftharpoons A_{red} \quad \Rightarrow \quad A_{ox} + 1/2H_2 \rightleftharpoons A_{red} + H^+. \tag{2.6}$$

The introduction of the standard hydrogen level can be technically realized by a two compartment electrochemical cell as shown in Fig.(2.1).

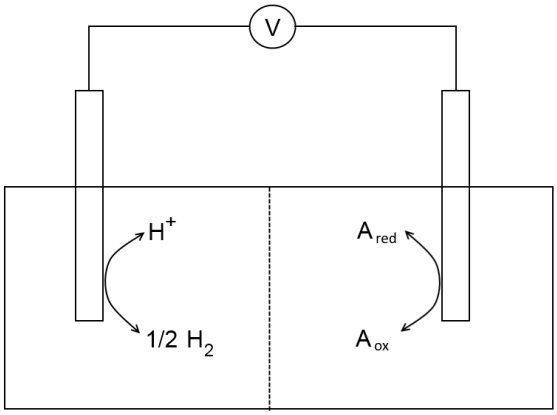

Figure 2.1: Schematic of an electrochemical cell consisting of the electrode measured, immersed in the electrolyte under consideration on the right hand side and an electrode immersed in a standard hydrogen electrolyte on the left hand side. The two compartments are separated by a membrane that prevents a mixing of the different electrolytes.

In such a cell the two chemical environments of the two electrodes are separated by a membrane which prevents the mixing of the electrolytes. It is, however, crucial that the membrane is electrically conductive and that, thus, the electrostatic potential is constant throughout the entire liquid phase taking a value of ϕ_s. If a platinum electrode is used on the left hand side of Fig.(2.1) the electrode is called a **standard hydrogen electrode (SHE)**. The electrode on the right hand side is typically the one under investigation and is thus called **working electrode**. The electrochemical potential $\widetilde{\mu}_s$ of the electrons in the electrolyte solution in the standard hydrogen scale can then be linked to the chemical potentials of the chemical species involved in the reaction, $\mu_{A_{red}}$ and $\mu_{A_{ox}}$

$$\begin{aligned} \widetilde{\mu}_s &= \mu_{A_{red}} - \mu_{A_{ox}} - e\phi_s - (1/2\mu_{H_2} - \mu_{H^+} - e\phi_s) \\ &= \mu_{A_{red}} - \mu_{A_{ox}} + \mu_{H^+} - 1/2\mu_{H_2}. \end{aligned} \tag{2.7}$$

In equilibrium the electrochemical potentials of all particle species that can cross an interface align across this interface. Therefore, in the standard hydrogen scale the electrochemical potential of the electrons in the electrolyte is identical to the potential difference measured between the two electrodes in Fig.(2.1). This potential difference is then called the equilibrium electrode potential E_{el}^{eq}. This electrode potential can then in turn for a general electrochemical reaction involving the transfer of n charge carriers be linked to the activities of the chemical species involved in the redox reaction taking place at the working electrode via the Nernst equation:

$$E_{el}^{eq} = E^0 + \frac{RT}{nF} \ln \left(\frac{\prod_{ox,i} a_i^{\nu_i}}{\prod_{red,j} a_j^{\nu_j}} \right), \tag{2.8}$$

where $F = 96485$ C/mol is the Faraday constant, E^0 is the standard electrode potential, i.e. the potential in the case that the activity of all chemical species is unity and $a_{i,j}$ and $\nu_{i,j}$ the activities and stoichiometric coefficients of the oxidized and reduced species, respectively.

2.1.2 Semiconductor electrodes

When a semiconductor is brought into contact with an electrolyte the electrochemical potentials of the electrons in both material phases align. This alignment is microscopically brought about by the formation of a space charge region on both sides of the interface. The material with the higher electrochemical potential prior to contact will emit electrons or absorb holes and will thus by charged positively, while the other material will be charged negatively. As the bulk of a conductive material is never charged, these charges are in the vicinity of the interface. The extension of the space charge layer into the semiconductor electrode is rather large ($\approx 1 - 10$ μm) and depends on the doping level. The reason for this is that only a small fraction of the lattice atoms, the dopant atoms, are ionized. The charge density of the lattice is thus rather small and it takes a comparatively large space charge region to accommodate the necessary charging of the electrode. In contrast, the charge density of the electrolyte is carried by all ions in the solution. The charge carrier density can thus be much higher, leading to a much smaller extension of the space charge layer in the order of ≈ 1 nm. The space charge layer in the electrolyte is typically referred to as double layer. Precisely at the interface, the energetic position of the band edges of the semiconductor with respect to the vacuum level is unaffected by the presence of the interface. In the bulk it is, however, changed by the potential drop in the semiconductor leading to a band bending in the space charge region. Typically this band bending introduces an energetic barrier that has to be overcome by any charge carrier that is to be interchanged across the interface. In the dark, for p-doped silicon the charge carrier concentration in the valence band exceeds the charge carrier concentration in the conduction band by several orders of magnitude and vice versa for n-doped silicon. This means that one normally expects only one band to exchange charges with the electrolyte at a significant rate. This is true for both anodic and cathodic processes. In equilibrium, the barrier for both current directions is identical and a small current, the dark saturation current j_{ds}, flows in both directions. It is exponentially dependent on the equilibrium barrier height $E_{\mathrm{b}}^{\mathrm{eq}}$

$$j_{\mathrm{ds}} \propto e^{-E_{\mathrm{b}}^{\mathrm{eq}}/kT}. \tag{2.9}$$

If an external bias η is applied, the net current flowing is still dependent on the barrier height and it is thus the behavior of the barrier height as a function of the external bias, i.e., $E_{\mathrm{b}}(\eta)$, that determines the current. Assuming that the external bias only drops across the interface, its effect on the barrier height is qualitatively shown in Fig.(2.2). As apparent from Fig.(2.2) neither the anodic barrier height for an n-doped nor the cathodic barrier height for a p-doped semiconductor are affected by the external driving force. Instead, the external bias drops across the space charge layer in the semiconductor which is widening in this case. Conversely, the anodic barrier height for a p-doped and the cathodic barrier height for an n-doped semiconductor are linearly dependent on the external bias. The overall ηj-characteristic in both cases is thus a diode characteristic and takes the following form:

$$\begin{aligned} j &= j_{\mathrm{ds}} \left(e^{-e\eta/kT} - 1 \right) \quad ; \quad \mathrm{n-doped} \\ j &= j_{\mathrm{ds}} \left(e^{e\eta/kT} - 1 \right) \quad ; \quad \mathrm{p-doped.} \end{aligned} \tag{2.10}$$

The semiconductor electrolyte interface thus behaves like a diode where the cathodic reaction corresponds to the forward bias direction for n-doped samples and the anodic reaction cor-

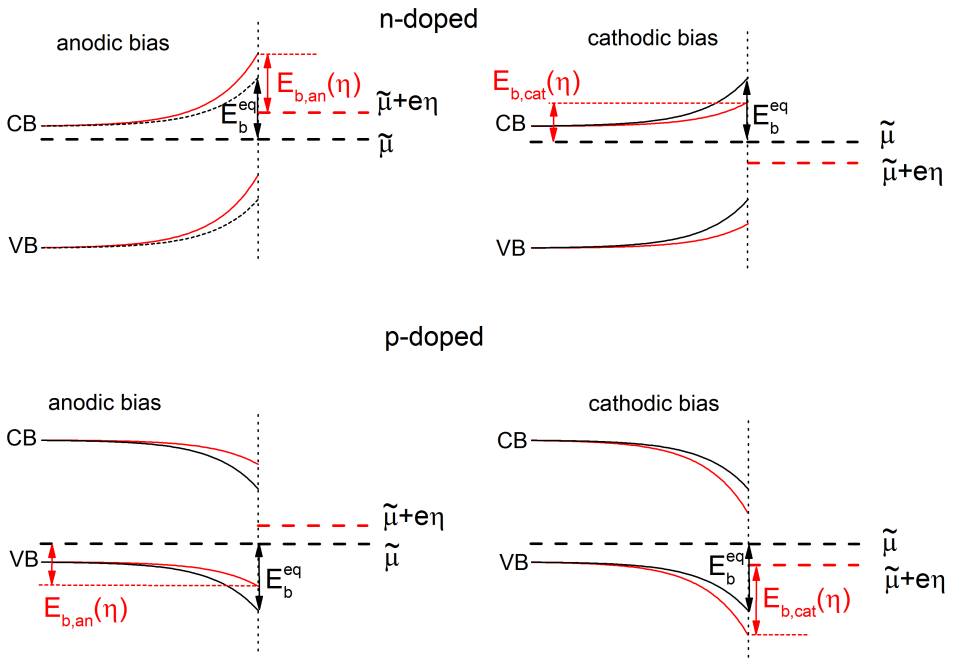

Figure 2.2: Influence of the external bias on the barrier height for an n- (top) and p-doped (bottom) semiconductor for an anodic bias (left) and a cathodic bias (right).

responds to the forward bias for p-doped samples. In general for a doped semiconductor the forward bias direction is thus accompanied by an emission of its majority charge carriers.

2.1.3 Non-equilibrium conditions

When a stationary state out of equilibrium is maintained, the electrochemical potential changes as a function of position and these changes can be identified with the driving force of the electrical current j. This current requires an active external driving force which throughout this work will be achieved by an active potentiostatic control. In the easiest case a steady state with a constant current is then established. This case corresponds to the branch denoted 'steady flow equilibrium' in the left hand side of Fig.(1.1). Here, all quantities are time independent and a certain fixed profile of the electrochemical potential throughout the system is established. In more general cases, further away from equilibrium, the profile of the electrochemical potential is itself varying in time and a certain profile of the electrochemical potential can only be given for a fixed point in time. An example are oscillatory states which play a central role in this thesis. We now proceed to visualize the spatial evolution of the electrochemical potential $\widetilde{\mu}(z)$, z being the direction perpendicular to the electrode surface, for a given non-equilibrium state at a point in time for the complex interface involved in the silicon electrodissolution. This is shown in Fig.(2.3). The nomenclature introduced in this figure will be used throughout the rest of this thesis. For given potentiostatic conditions the voltage U is fixed by the potentiostat between the silicon working electrode and the reference electrode, which means that the system is thereby forced to establish a state where the voltage drop across the external resistance, IR_{ext}, and the voltage drop across the electrode, U_{el}, are equal to the total voltage drop U. The total driving force for the current crossing the system $\Delta\widetilde{\mu}_{\text{tot}}(j)$ is then given by:

$$\Delta\widetilde{\mu}_{\text{tot}} = e(U - E_{\text{Si}}^{\text{eq}}), \tag{2.11}$$

where $E_{\text{Si}}^{\text{eq}}$ is the equilibrium electrode potential in the given state of the surface. This driving force is required to overcome the various impedances in the system such as kinetic barriers

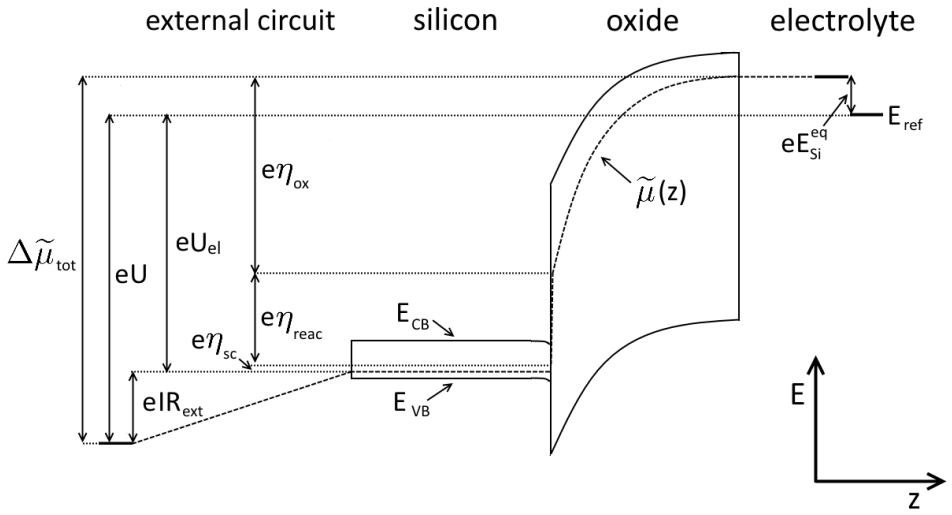

Figure 2.3: Schematic of the spatial profile of the electrochemical potential $\widetilde{\mu}(z)$ for the anodic electrodissolution of p-type silicon. The applied voltage U, the voltage drop across the electrode U_{el}, the equilibrium electrode potential $E_{\mathrm{Si}}^{\mathrm{eq}}$ and the overpotentials necessary to drive the given current through the impedances of the space charge layer, η_{sc}, the electrochemical oxidation reaction, η_{reac}, and the oxide layer, η_{ox}, are shown together with the energy levels of the reference electrode, E_{ref}, and the valence and conduction band edges, E_{VB} and E_{CB}.

in space charge layers and the electrochemical reaction itself and transport inhibitions in the oxide layer. The corresponding drops in the electrochemical potential are then denoted with $e\eta_{\mathrm{sc}}$ for the space charge layer in the silicon, $e\eta_{\mathrm{reac}}$ for the kinetic inhibition of the reaction and $e\eta_{\mathrm{ox}}$ for the transport through the oxide, respectively. The different parts of the system show different driving force/current (ηj-)characteristics which, in turn, determine the overall current at a given external drive at a given time. The five most important important types of ηj-characteristics which determine the overall reaction of the silicon electrodissolution system in this work are given in the following.

1. **Ohmic resistances:** An ohmic resistance has a linear characteristic, i.e., the drop in the electrochemical potential $\Delta\widetilde{\mu}$ across this resistance is linearly dependent on the current

$$j \propto \Delta\widetilde{\mu}. \tag{2.12}$$

   This type of resistance occurs in any bulk phase of the system and the external resistance. As the chemical potential is constant in each bulk material phase, the drop in the electrochemical potential can be identified with a drop in the electrostatic potential, i.e. $\Delta\widetilde{\mu} = -e\Delta\phi$.

2. **Electrochemical reaction:** As any chemical reaction, an electrochemical reaction is proceeding at a finite speed. In equilibrium the rates in both directions are identical and thus no net current flows through the electrode. In order to drive a net current in either the cathodic or anodic direction an applied voltage of $U_{\mathrm{el}} \neq E_{\mathrm{el}}^{\mathrm{eq}}$ is required. The drop in electrochemical potential required to drive the electrochemical reaction at a given current is called the overpotential and is here denoted with $\Delta\widetilde{\mu} =: -e\eta_{\mathrm{reac}}$. At small overpotentials the current increases approximately linearly with the overpotential. More importantly, at higher overpotentials the dependence becomes exponential

$$j \propto e^{e\eta_{\mathrm{reac}}/kT}. \tag{2.13}$$

3. **Space charge layers:** Space charge layers at the electrode interface can introduce additional kinetic barriers for the current transport. The overcoming of these barriers then also requires overpotentials, very similar as in the case of reaction kinetics. For semiconductor electrodes these barriers lead to a diode behavior of the interface as was discussed in Sec.(2.1.2). In forward bias direction the ηj-characteristic is then again exponential.

$$j \propto e^{e\eta_{\mathrm{sc}}/kT}. \tag{2.14}$$

4. **Ionic transport:** In general, in a steady state changes in ion concentrations will be present. The reason for this is that some ionic species are constantly produced at the electrode surface while others are constantly consumed there. This change in concentration then leads to a change in the electrochemical potential of the electrons as a function of the concentrations of the respective ionic species according to Eq.(2.8). In an unstirred isotropic medium in a steady state this change is then linear, while inhomogeneities in the electrolyte medium or the its flow field may lead to nonlinear characteristics. A case of special importance in this work is the strongly inhibited ionic transport through a passivating oxide layer.

5. **Current cut-off:** A last contribution to the total overpotential required to drive a given current through the system is either achieved by a restricted illumination of n-doped silicon or by the introduction of a current limiter. In both cases this contribution has no effect if the total current is below a certain threshold value $I < I_{\mathrm{lim}}$ and takes up all the driving force not required for the other overpotentials for currents above this threshold value $I > I_{\mathrm{lim}}$. Current voltage characteristics of the current limiter used in this work are shown in Fig.(2.4) for various levels of I_{lim}.

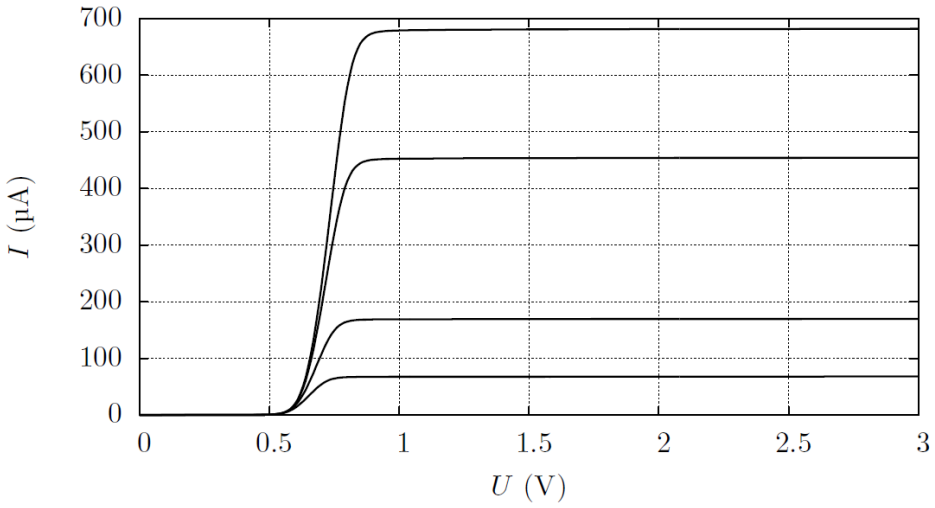

Figure 2.4: UI-characteristics of the current limiter used in this work for 4 levels of the limiting current (Graphic taken from [41]).

As apparent from the UI-characteristics in Fig.(2.4), even in the unlimited case a voltage drop of ca. 0.5 V occurs at the limiter. For this reason measurements with limiter are conducted with a correspondingly higher applied voltage, typically $U = 9.15$ V vs. SHE.

2.2 Anodic electrodissolution of silicon

The experimental system under consideration is the potentiostatic electrodissolution of silicon under high anodic voltage in the presence of a fluoride containing electrolyte. In this process, the silicon is first electrochemically oxidized and the oxide layer is subsequently etched away purely chemically by the fluoride in the electrolyte. As a result of this interplay, depending on the external voltage, a stable oxide layer may or may not form. The experiment is a controlled corrosion experiment and it is natural to describe the system in a moving frame where in this work the silicon|silicon oxide interface is used as the origin in growth direction.

2.2.1 Anodic oxidation

The anodic oxidation follows either a tetravalent or a divalent mechanism, where in both cases the first stage is an electrochemical and the second stage a chemical process [37, 47]:

$$\begin{aligned} \mathrm{Si} + 4\mathrm{H_2O} + \nu_{\mathrm{VB}} h^+ &\rightarrow \mathrm{Si(OH)_4} + 4\mathrm{H^+} + (4-\nu_{\mathrm{VB}})e^- \\ \mathrm{Si(OH)_4} &\rightarrow \mathrm{SiO_2} + 2\mathrm{H_2O} \quad \text{(tetravalent)} \\ \mathrm{Si} + 2\mathrm{H_2O} + \nu_{\mathrm{VB}} h^+ &\rightarrow \mathrm{Si(OH)_2} + 2\mathrm{H^+} + (2-\nu_{\mathrm{VB}})e^- \\ \mathrm{Si(OH)_2} &\rightarrow \mathrm{SiO_2} + \mathrm{H_2} \quad \text{(divalent).} \end{aligned} \tag{2.15}$$

Here, ν_{VB} is the amount of charge carriers stemming from the valence band of the silicon. As the divalent oxidation mechanism is accompanied by $\mathrm{H_2}$ evolution, the relative prevalence of both oxidation valences can be well distinguished. A significant contribution of the divalent mechanism is only found for relatively low anodic voltages and the average reaction valency ν in the parameter regime considered in this work is close to $\nu = 4$ [48].

As the silicon electrode acts as an anode it can only interact with the electrolyte at a significant rate via valence band processes as discussed in Sec.(2.1.2). For this reason n-doped silicon samples have to be illuminated to permit the anodic oxidation reaction. Due to the presence of the silicon oxide layer this restriction is only valid for the initial charge transfer step, leading to $\nu_{\mathrm{VB}} \geq 1$ in Eq.(2.15) [49]. Electron injections from the oxide into the conduction band can lead to an overall current higher than the one induced by the photon flux incident on the surface, i.e., to internal quantum efficiencies larger than 1 [50]. This current multiplication effect increases with decreasing illumination intensity and the limiting value of $\nu_{\mathrm{VB}} = 1$ has been experimentally realized in the literature [50, 48]. This trend can be understood when considering the respective rates of the hole capture and electron injection, where the former is decreased for decreasing illumination while the latter could remain unaffected. While this trend is also present in the experiments presented in this work, the values typically found are in the range of $2 \leq \nu_{\mathrm{VB}} \leq 4$ and thus only a limited current multiplication effect is found [42].

2.2.2 Etching

The etching of the oxide is mainly due to the species HF and $\mathrm{HF_2^-}$ in dimolecular processes where the following three reactions have been identified [51]:

$$\begin{aligned} \mathrm{SiO_2} + 6\mathrm{HF} &\rightarrow \mathrm{SiF_6^{2-}} + 2\mathrm{H_2O} + 2\mathrm{H^+} \\ \mathrm{SiO_2} + 3\mathrm{HF_2^-} + \mathrm{H^+} &\rightarrow \mathrm{SiF_6^{2-}} + 2\mathrm{H_2O} \\ \mathrm{SiO_2} + 2\mathrm{HF} + 2\mathrm{HF_2^-} &\rightarrow \mathrm{SiF_6^{2-}} + 2\mathrm{H_2O}. \end{aligned} \tag{2.16}$$

The etch rate $\dot{\mu}_E$ can best be measured electrochemically in a steady state where oxidation and etching are proceeding equally fast. In this case it is tied to the measured oxidation current j in the following way:

$$\dot{\mu}_E = \frac{j}{F\nu}. \tag{2.17}$$

As the distribution of the fluoride to the species HF, HF_2^- and F^- is pH dependent and the rates for all dimolecular reaction pathways of the two etching species are different, the pH value as well as the total fluoride concentration c_F determine the total etch rate. It is thus possible experimentally to vary the etch rate as well as the dominant etching pathway by the variation of the pH value of the solution and c_F. The pH dependence of the distribution of fluoride to the different relevant molecules and the resulting etch rates at an applied voltage of $U_{el} = 2.44$ V vs. SHE according to literature values are shown in Fig.(2.5) [51].

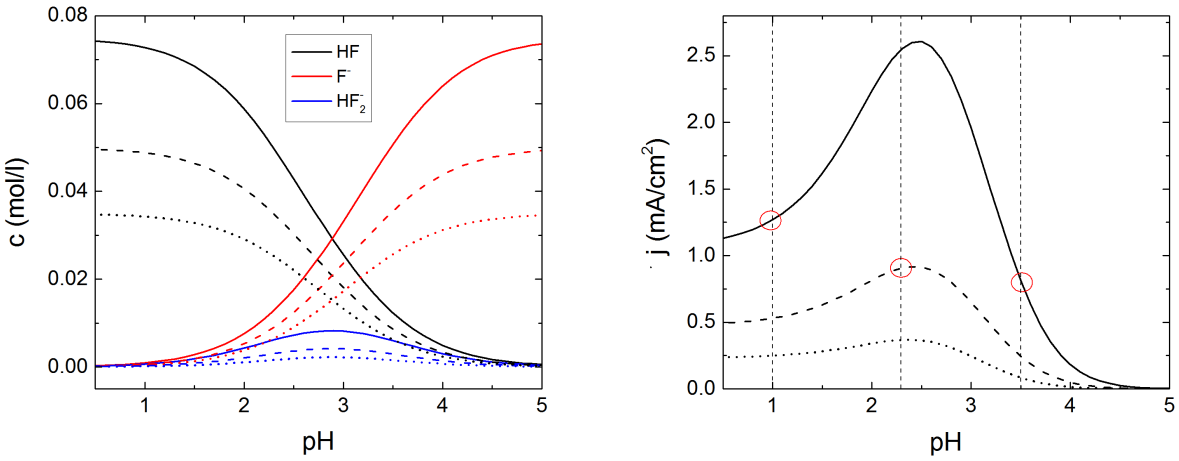

Figure 2.5: Distribution of the different fluoride species as a function of the pH value for a total fluoride concentration of: $c_F = 75$ mM (solid), $c_F = 50$ mM (dash) and $c_F = 35$ mM (dot) (left). Steady state oxidation current at $U_{el} = 2.44$ V vs. SHE for $c_F = 75$ mM (solid), $c_F = 50$ mM (dash) and $c_F = 35$ mM (dot) (right). The vertical dashed lines mark the three pH values used throughout the experiments in this work and the red circles the three most common electrolyte compositions. The curves are calculated using literature constants [51].

At a relatively low pH value the etching process is dominated by the neutral species HF, while at higher pH values the etching with HF_2^- becomes more important. All etching processes together lead to a maximum in the overall etch rate at a pH value of ≈ 2.5 [52, 51]. Note that this is not consistent with all literature findings [53], but very much in line with our own experiments. At applied voltages where the electrode is in an oscillatory state it is not straight forward to map the etch rate to the measured oxidation current. Still, as the oscillatory state is still a stable state even in this case it is instructive to take a look at the pH dependence of the average etch rate $\bar{\dot{\mu}}_E$ which can be measured using the average oxidation current j_{av} analog to Eq.(2.17):

$$\bar{\dot{\mu}}_E = \frac{j_{av}}{F\nu}. \tag{2.18}$$

When comparing states directly at the onset of the oscillatory parameter regime in different electrolytes, a similar dependence of the average etch rate with respect to the pH value as in the steady flow equilibrium shown in Fig.(2.5) is found.

2.3 Experimental setups

To study the properties of the oxide layer during the potentiostatic (photo-)electrodissolution of silicon, a three electrode electrochemical cell equipped with an ellipsometric imaging system providing in-situ spatially resolved information on the optical path through the oxide layer is used. A schematic is shown in Fig. 2.6.

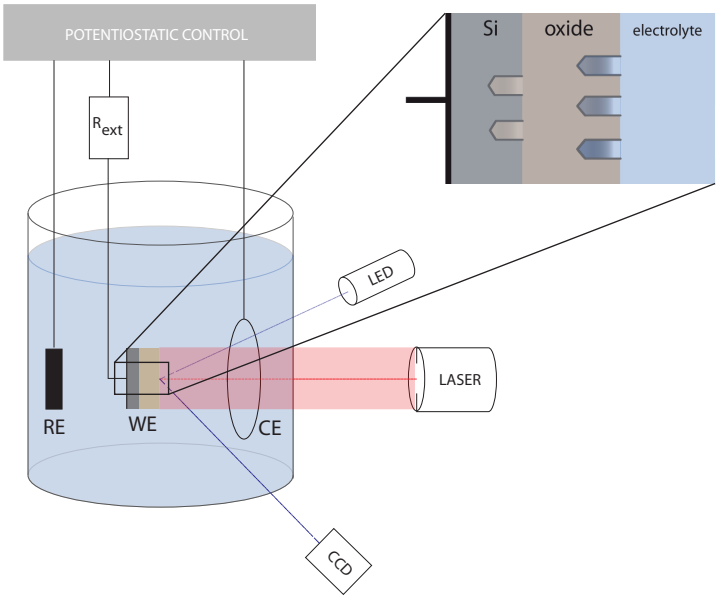

Figure 2.6: Sketch of the experimental setup showing the arrangement of the three electrodes and the external resistance together with the optical paths for the sample illumination (red) and the spatially resolved ellipsometric imaging (blue). A cross section of the interface and the growth direction of the oxide is shown in the inset.

In order to withstand corrosion in the fluoride containing electrolyte the electrochemical cell is built from PTFE and the optical windows are made of sapphire. Before each experiment the electrolyte is bubbled with argon while constantly stirred at approximately 10 Hz with a magnetic stirrer for ca. 30 min. For the measurements the glass bubblers are then removed to prevent an undefined change of the fluoride concentration and an argon overpressure is maintained in the cell with an additional gas inlet. The working electrode is approximately rectangular and typically has a size of $15 - 25$ mm^2. A circular bent (diameter $\approx$5 cm) platinum wire (99,99 %, Chempur) placed symmetrically in front of the working electrode at a distance of about 5 cm is used as the counter electrode and a saturated $Hg|Hg_2SO_4$ reference electrode ($U_{\mathrm{ref}} = 0.64$ V vs. SHE [54]) is placed behind the working electrode. The stirring is retained during the experiments to ensure a spatially uniform concentration of the relevant chemical species at the surface of the working electrode. A potentiostat (FHI-2740, electronics laboratory of the Fritz-Haber-Institut, Berlin, Germany) is used for the potentiostatic control of the experiments and the current and voltage data are digitized using a data acquisition board (PCI-6221, National Instruments).

As dynamical phenomena are of interest, there are three possibilities to adjust dynamical parameters. First, a tunable resistance is connected in series to the working electrode and, second, a spatially uniform illumination with variable intensity is implemented. The former introduces a global coupling between all points by changing the voltage drop across the work-

ing electrode as a function of the current, while the latter introduces an upper limit to the total current. In addition to this, in some experiments a current limiter is connected in series with the external resistance and the working electrode. This current limiter has no effect as long as the current is below a tunable threshold value j_{lim} and introduces an effectively infinite resistance which takes up all excess voltage when the current reaches the threshold. The voltage drop across the limiter is also measured and thus the voltage drop across the working electrode U_{el} can still be given. The main purpose of the current limiter is to mimic the behavior of the illumination limitation, but it is also introducing interesting effects apart from this.

2.3.1 Ellipsometric imaging

The optical path used for the ellipsometric imaging is schematically shown in Fig.(2.7) as a top view of the electrochemical cell.

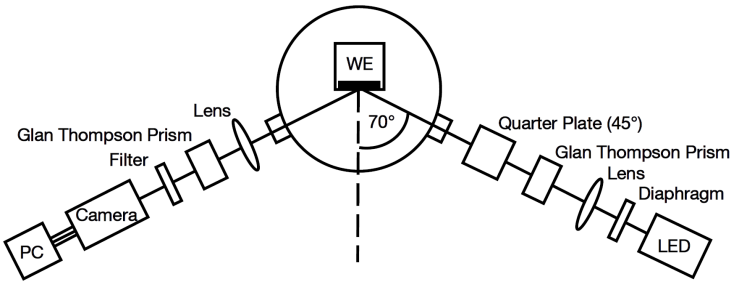

Figure 2.7: Schematic of the light path used for the in-situ ellipsometric imaging of the oxide layer on the silicon samples.

The polarization of elliptically polarized light incident on the surface is changed upon reflection at the Si|SiO_2|electrolyte interface and this change is then converted into an intensity signal by a polarizer (Glan-Thompson prism). Insertion of an imaging optic in the reflected light path gives an image of the electrode on a CCD chip with 640×480 pixels (JAI CV-A50). The data are then digitized using a frame grabber card (PCI-1405, National Instruments). This system allows the in-situ measurement of the optical path through the silicon oxide at a given area on the surface with a spatial resolution in the 10 μm range. We call the intensity at each pixel relative to the overflow limit of the CCD the ellipsometric intensity $\xi(\vec{x})$. For an optimal contrast an angle of incidence on the sample surface close to the Brewster angle of the Si|water system (ca. 70°) has to be chosen. The intensity signal is in general not linearly dependent on the oxide layer thickness [55]. We approximate it, however, linearly during the oscillations as the amplitude of the oscillations is typically small compared to the total dynamical range of the intensity signal.

2.3.2 Illumination

The illumination system realized in the experimental setup was established in the course of this work and is schematically shown in Fig.(2.8). In this setup the laser beam is widened to a diameter of ca. 2 cm and only a part from its middle with a diameter of ca. 0.5 cm is incident on the silicon sample. In this way a spatial variation of the illumination intensity due to the gradually decreasing laser intensity towards the edge of the illuminated area is prevented and the illumination has a good uniformity. The additional sensor in the light path allows for an in-situ measurement and recording of the illumination intensity once calibrated. For the calibration procedure the sample is replaced by a hand-held wattmeter and the aperture size

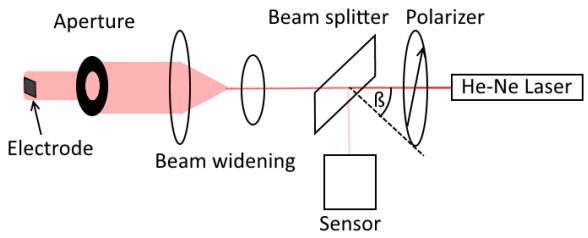

Figure 2.8: Schematic of the light path used for the illumination of the silicon samples.

is fixed to a diameter of 4 mm. The intensity in the respective light paths is then determined by the polarizer angle ϑ and the total transmitivities and reflectivities for the parallel and perpendicular components of the light at the beam splitter $T_{\perp/\parallel,\text{total}}$ and $R_{\perp/\parallel,\text{total}}$. The latter two are dependent on the angle of incidence β of the laser at the beam splitter and multiple reflection within the beam splitter have to be taken into account. Using the Fresnel equations the respective intensities on sensor I_{sens} and wattmeter I_{sample} are then given by:

$$\begin{aligned} I_{\text{sens}} &= I_0 \cdot cos^2(\vartheta)\left(R_{\perp,\text{total}}(\beta)\cdot cos^2(\vartheta) + R_{\parallel,\text{total}}(\beta)\cdot sin^2(\vartheta)\right) \\ I_{\text{sample}} &= I_0 \cdot cos^2(\vartheta)\left(T_{\text{s}\perp,\text{total}}(\beta)\cdot cos^2(\vartheta) + T_{\parallel,\text{total}}(\beta)\cdot sin^2(\vartheta)\right). \end{aligned} \tag{2.19}$$

In our setup the incident angle is precisely $\beta = \pi/4$. The calibration curve used throughout this work is shown in Fig.(2.9).

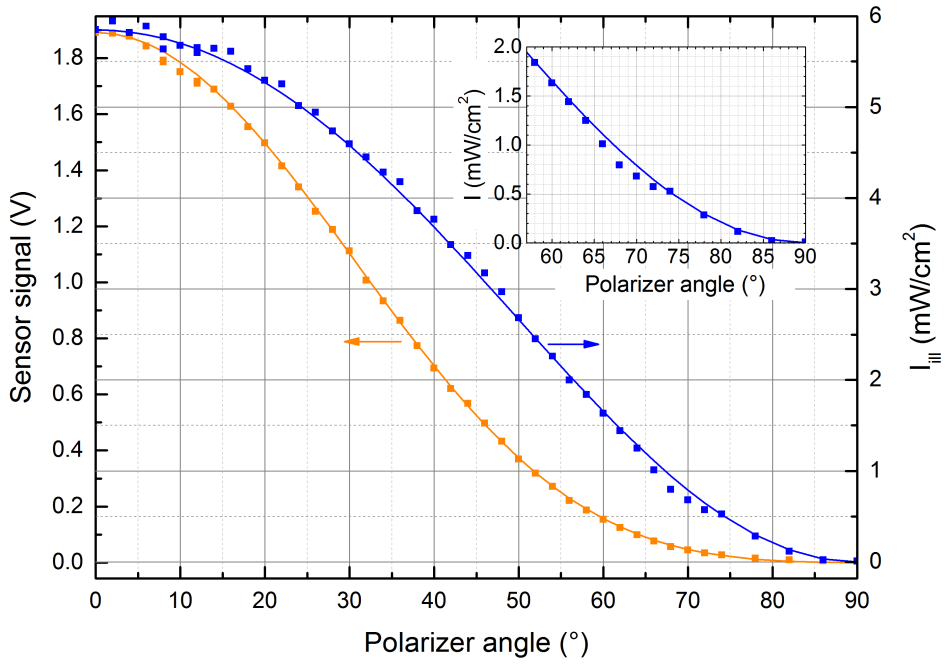

Figure 2.9: Calibration measurement of the He-Ne laser intensity for sample illumination as a function of the polarizer angle. Left: CCD voltage measured in reflection of the beam splitter (red); Right: Intensity measured with wattmeter in transmission through the beam splitter at the position of the sample (blue). A zoom in on the polarizer angle values most frequently used is shown in the inset.

It is often instructive to divide the current density j by the number of absorbed photons $(1-R)\cdot\dot{N}/A_{\text{abs}}$, where R is the reflectivity of the sample, $\dot{N}$ the total incoming photon

flux and A_{abs} the sample area. This quantity is called the internal quantum efficiency Φ. As the laser emits monochromatic light with a fixed photon energy of $E_{\mathrm{ph}} = 1.96$ eV and the reflectivity can be approximated by its value for the air silicon surface of $R \approx 0.3$ [56] its value is given by:

$$\Phi = \frac{j}{(1-R)\cdot \dot{N}/A_{\mathrm{abs}}} = \frac{jE_{\mathrm{ph}}}{(1-R)\cdot I_{\mathrm{ill}}} \approx \frac{(1.96\ \mathrm{V})\cdot j}{0.7\cdot I_{\mathrm{ill}}}. \tag{2.20}$$

2.3.3 Sample preparation

For all experiments single crystalline silicon is used. In the case of p-doped samples the measurements are either conducted at the (100)-surface of samples with a resistivity of ϱ =10-20 Ωcm or the (111)-surface of samples with a resistivity of $\varrho = 5 - 25$ Ωcm. The resistivity given corresponds to a doping level of ca. $n_{\mathrm{A}} = 10^{15}$ cm^{-3} [57]. The n-doped samples investigated are all the (111)-surfaces of silicon samples with resistivities ranging from high values of $\varrho > 40$ Ωcm over intermediate values of either $\varrho = 3 - 5$ Ωcm or $\varrho = 1 - 10$ Ωcm to low values of $\varrho = 0.1 - 0.5$ Ωcm, corresponding to doping levels of $n_{\mathrm{D}} < 10^{14}$ cm^{-3}, ca. $n_{\mathrm{D}} = 10^{15}$ cm^{-3} and ca. $n_{\mathrm{D}} = 5 \cdot 10^{16}$ cm^{-3}, respectively [57]. A thermally evaporated 200 nm aluminum layer is used as a back contact for all samples. The closed metal layer at the back ensures a spatially uniform potential distribution in the bulk of the silicon samples. In order to ensure an ohmic behavior, this contact was always annealed under 100 mbar nitrogen atmosphere. For p-doped samples the proposed mechanism for making the contact ohmic is a deep diffusion of the trivalent aluminum atoms into the silicon and a consequent gradual increase of the doping level toward the contact. In this way the sample is degenerately doped close to the contact, leading to a barrier free, ohmic metal|semi-metal connection. Consequently, the annealing is conducted at a relatively high temperature of 400 °C for a relatively long duration of 30 min. In contrast, for n-doped samples the fact that the work function of aluminum (4.06-4.26 eV [58]) is close to the electrochemical potential of the electrons in the conduction band is exploited. The latter was calculated in Eq.(2.4) for the doping level corresponding to the resistivity used ($n_{\mathrm{D}} \approx 10^{15}$ cm^{-3}) and has a value similar to the the work function of aluminum. In this case only a small barrier is expected to form at the interface between both materials leading to an easy charge carrier transfer across this barrier. The annealing thus serves a different purpose than for the p-doped samples, namely to increase the area of the interface and possibly to heal defects. The parameters chosen for the annealing are thus quite different from the corresponding values for p-doped silicon and a relatively low temperature of 250 °C is applied for a relatively short period of time of 15 min. The conceptual energy diagram for both contacts is shown in Fig.(2.10). For the ellipsometric silicon oxide detection the samples are fixed and electrically contacted with conductive silver paste on a custom made polytetrafluoroethylene (PTFE) sample holder. Silicone rubber (Scrintex 901, Ralicks GmbH, Rees-Haldern, Germany) is then used to seal the sample and the holder leaving an opening of 15-25 mm^2 in contact with the electrolyte. Prior to the experiments, the working electrodes are cleaned by first cautiously rubbing them with an acetone (Merck, p.a.) drenched tissue and subsequently immersing them for 5 min each in acetone (Merck, p.a.), ethanol (Merck, p.a.), methanol (Merck, p.a.) and ultra pure water (18.2 MΩcm). The assembled working electrode is then electrically connected using a banana jag and placed in the electrochemical cell.

All PTFE and platinum parts used are regularly cleaned with boiling piranha solution and are always stored in ultra pure water. An aqueous 1 M KOH solution is used to clean the glassware. All parts are stored in covered ultra pure water baths to stay clean.

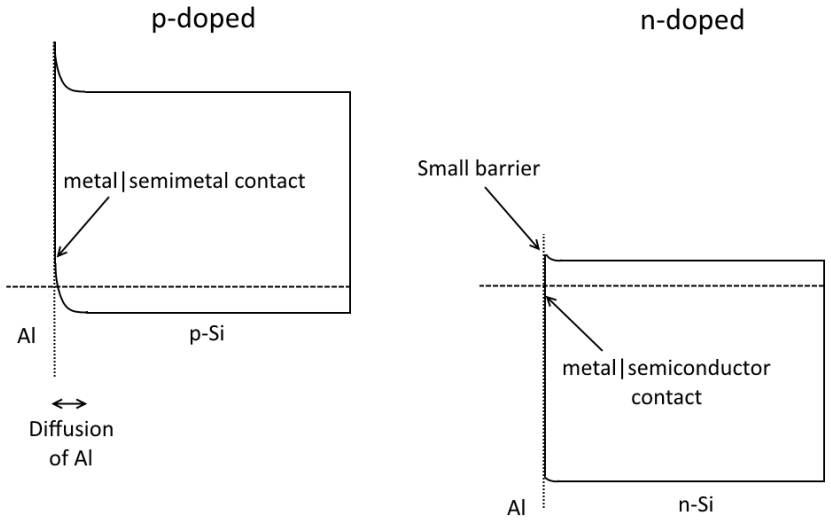

Figure 2.10: Schematic energy diagrams for the aluminum back contacts of p- (left) and n-doped (right) silicon samples.

2.3.4 H_2 detection

The hydrogen detection experiments are carried out in two different experimental setups. First, we use a custom made, compact poly(methyl methacrylate) (PMMA) electrochemical flow cell. Here the p-Si working electrode is mounted using an FKM O-ring (diameter 4 mm) as sealing. The electrolyte is constantly bubbled with argon in a reservoir above the working electrode where also a glassy carbon rod (HTW GmbH, Thierhaupten, Germany) acting as the counter electrode is placed. For the measurements the electrolyte is drawn at a defined flow rate of 4 μls^{-1} from the reservoir past the working electrode and a platinum wire ca. 40 μl downstream of the working electrode by an syringe pump (WPI, Berlin, Germany), resulting in a time delay between hydrogen production and detection of 10 s. The saturated Hg/HgCl reference electrode (SCE) is also placed downstream of the working electrode to prevent IR-distortions to the applied voltage due to the relatively small cross-sectional areas of the flow channel ($\approx 2-4$ mm^2) combined with a significant electrolyte resistivity. The potential control of both the p-Si working electrode and the platinum electrode and the acquisition of the potentials and currents on both electrodes are realized with a PGU bipotentiostat (IPS, Münster, Germany). Again a switchable resistor R_{ext} is placed between working electrode and potentiostat. The hydrogen produced at the working electrode is oxidized at the platinum wire at a potential of 200 mV vs. SCE = 306 mV vs. RHE = 442 mV vs. SHE. The collection efficiency of the platinum wire is identified prior to the experiments at each day by measuring the H_2 oxidation current with a cathodic potential applied at the illuminated p-Si working electrode leading exclusively to H_2 formation there [38]. Before and after each measurement we measure the current at the Pt-wire without hydrogen evolution at the working electrode and the obtained values are then linearly interpolated as the background correction for the measurement in between.

The second setup we use is a commercial rotating ring/disk electrode (PINE) and the potentiostat also used in the flow cell setup mounted in a custom built PMMA cell. The disk is a circular silicon piece cut from one of our wafers (p-Si (111), 5-25 Ωcm) with a diameter of 5 mm. This disk is mounted on a piece of copper to assure mechanical stability and sealed with the same silicone rubber used for the ellipsometric imaging experiments. The distance between the outer border of the disk and the Pt-ring is 0.5 mm.

In addition to the cleaning and sample preparation methods described above, all PMMA parts were first immersed in an aqueous solution of 1 % $KMnO_4$ for several days and then cleaned of residual MnO_2 using 10 % HCl in water.

2.4 Data analysis

The data of the ellipsometry measurements are recorded with a Labview program written in our group. They consist of an ASCII table containing the time t, applied voltage U, total current I, illumination sensor and spatially averaged ellipsometric intensity ξ with a temporal resolution of 10 Hz and a gray scale avi-video of the spatial distribution of the ellipsometric intensity on the electrode $\xi(\vec{x})$ with a frame rate of typically 1 Hz. To avoid too high amounts of data the recorded area for the video can be preselected to only contain the electrode and not the surrounding sealing, and the frame rate can also be reduced.

In the course of this work a MATLAB code for the data analysis with a graphical user interface was written. In the following a short overview over the manipulations of the raw data from the avi-video and the typical way of their presentation will be given. For further data analysis and presentation Origin is used.

Raw data manipulation: The main change in the original video data is made by a background correction. This correction becomes necessary as in general the raw data of the ellipsometric intensity $\xi(\vec{x})_{\mathrm{raw}}$ vary across the electrode surface independently of the actual measurement. As a consequence, a background has to be subtracted at every point individually. To achieve this the temporal average of the raw data of the ellipsometric intensity $\overline{\xi(\vec{x})}_{\mathrm{raw}}$ is subtracted at every point. Furthermore, the contrast of variations in the ellipsometric signal positively correlates with its absolute value. A linear correction is thus employed suppressing the signal from points with a high background intensity and enhancing the signal from points with a low background intensity

$$\xi(\vec{x}) = \left(\xi(\vec{x})_{\mathrm{raw}} - \overline{\xi(\vec{x})}_{\mathrm{raw}}\right) \frac{\left\langle \overline{\xi(\vec{x})}_{\mathrm{raw}} \right\rangle}{\overline{\xi(\vec{x})}_{\mathrm{raw}}}. \tag{2.21}$$

Here $\xi(\vec{x})$ is the corrected local time series and $\left\langle \overline{\xi(\vec{x})}_{\mathrm{raw}} \right\rangle$ is the spatial average of the time averages of the raw data of the local time series. In addition to this a part of the surrounding sealing is typically recorded alongside the electrode data. The points on the sealing are identified by their small temporal variation and artificially set to zero. Apart from these manipulations the data are used as recorded.

Realspace data: The main way of presenting the video data are 2d pseudo-color plots of the ellipsometric intensity $\xi(\vec{x})$ as defined in Eq.(2.21) on the entire electrode and the time evolution of these values from one dimensional cuts through the electrode. Taken together they offer a good qualitative overview over a given dynamical state.

Fourier Analysis: Fourier spectra are routinely created via the MATLAB 'FFT' function for both, the spatially averaged time series of current and ellipsometric intensity and the local time series at each individual point of the electrode. This allows for an isolation of modes associated with the patterns only and is especially helpful to analyze cluster patterns.

Analytical signal: In order to shed further light on the dynamics of a given state the analytical signal of rectangular parts of the video is generated. This analytical signal is a complex instead of a real time series where the measured, real data are the real part and the imaginary part is generated via a Hilbert transformation of the measured data using the MATLAB function 'Hilbert'. The generation of the analytical signal is aimed at improving the comparability of experimental results and the results of theoretical simulations as the latter are typically complex data.

3 Uniform dynamics

In this chapter the experimental findings for spatially uniform properties of the silicon electrodissolution system are presented. These findings are then the starting point for the modeling efforts in Chap.(4) and the study of the pattern formation in Chap.(6).

The measurements presented here were partly done by Carla Zensen, Andreas Heinrich and Maximilian Patzauer in the course of their respective Master theses which were supervised as a part of this work [41, 42].

3.1 Overview

3.1.1 Cyclic Voltammogram

A typical starting point for electrochemical investigations of any given electrochemical system is cyclic voltammetry where the electrode potential is swept back and forth linearly between two voltage limits and the current response is measured. A typical cyclic voltammogram of a silicon electrodissolution process together with the ellipsometric intensity ξ vs. voltage response are shown in Fig.(3.1) a) and b), respectively.

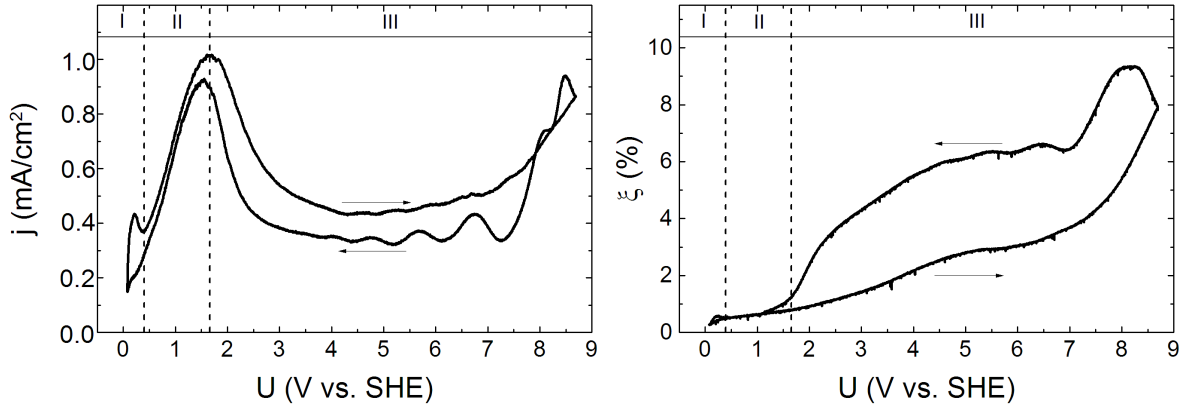

Figure 3.1: Cyclic voltammogram (left) (20 mV/s) of a highly illuminated n-Si sample (pH = 1, $c_F = 75$ mM) and the corresponding, spatially averaged signal of the oxide layer mass ξ (right). The arrows indicate the scan direction.

Below ca. 0.2 V vs. SHE (part I) the divalent oxidation mechanism described in Eq.(2.15) dominates [37, 47, 59]. Increasing the voltage the tetravalent mechanism becomes dominant but no stable oxide layer forms as the etching process is faster than the oxidation (part II). At voltages higher than ca. 1.7 V vs. SHE a stable oxide layer forms. This stable oxide layer leads to a decrease in the total current (part III). Starting at ca. 4 V vs. SHE in the upward scan current oscillations can be seen. These oscillations become even more pronounced upon reversal of the scan direction and can also be seen in the ellipsometric intensity ξ, as depicted in Fig.(3.1) b), which is a measure of the amount of silicon oxide present at the surface. The difference between the current in the upward and the downward scan can be well understood by the corresponding difference in the mass of the oxide layer on the electrode surface inhibiting the current. Summing this up, the features seen on the upward scan in parts I and II can

be attributed to the oxidation process while the current in part III is limited by the etching process. The dominant peak at ca. 1.7 V vs. SHE thus marks an important change in the qualitative interpretation of the measured current. In contrast to many other systems, the hysteresis between the upward and the downward scan is not due to capacitive effects, but given by the relatively slow equilibration between oxidation and etching leading to a drifting oxide thickness. For very slow scan rates this hysteresis can be all but eliminated as shown in Fig.(3.2). It is remarkable, however, that even in this very slow scan a hysteresis in the oxide layer thickness is clearly visible for $U > 6$ V.

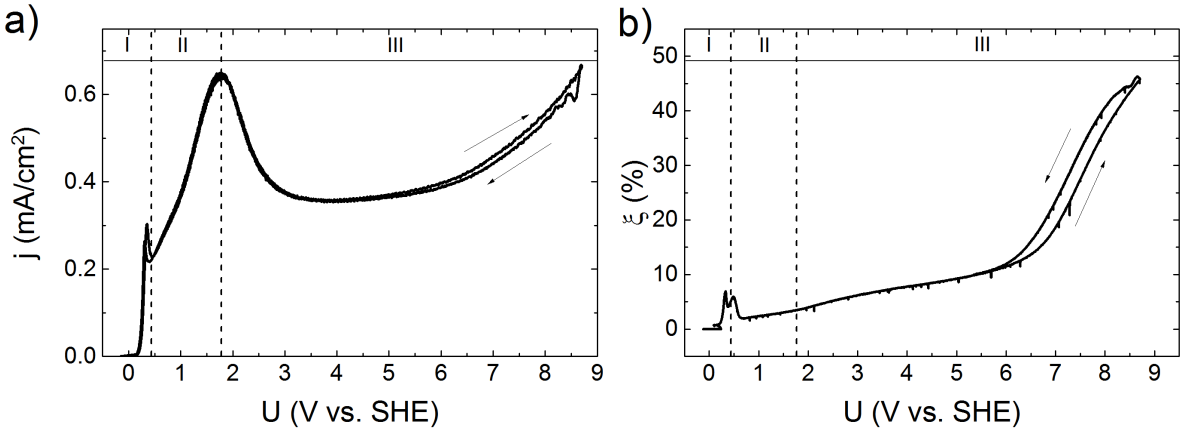

Figure 3.2: Cyclic voltammogram (left) (2 mV/s) of a p-Si sample (c_F = 50 mM, pH = 2.3) and the corresponding, spatially averaged ellipsometric intensity ξ (right). The arrows indicate the scan direction.

Outside of the oscillatory voltage regime the cyclic voltammogram without hysteresis constitutes a steady flow equilibrium and can be seen as the most basic behavior of the system in the given parameter regime tying in with the view expressed in the bifurcation diagram in Fig.(1.1). The qualitative behavior of the cyclic voltammograms is independent of electrolyte composition or doping type and level provided that n-doped samples are sufficiently illuminated (see also [52, 60]). Already from this it can be concluded that the electrochemical oxidation reaction and the chemical etching process are essential for the overall behavior and that the space charge layer in the silicon is of lower significance.

3.1.2 Reaction valency

In Fig.(3.3) a positive voltage scan of a p-doped silicon working electrode is shown together with the hydrogen evolution measured at a Pt probe electrode (see Sec.(2.3.4)). The latter is given as an equivalent current corrected for the collection efficiency of the Pt wire in the flow cell setup. The current peak at the lowest potential (U_1) corresponds to a strongly divalent ($\nu \approx 2$) dissolution of silicon as described in the bottom of Eq.(2.15). Accordingly, it is accompanied by pronounced H_2 formation. Increasing the potential first the hydrogen current sharply drops to a plateau until the second current peak at the silicon electrode (U_2) is reached and then drops further at potentials above 2 V vs. SHE. The overall form of the hydrogen current depicted in Fig.(3.3) is in good agreement with the values found in the literature [48, 59].

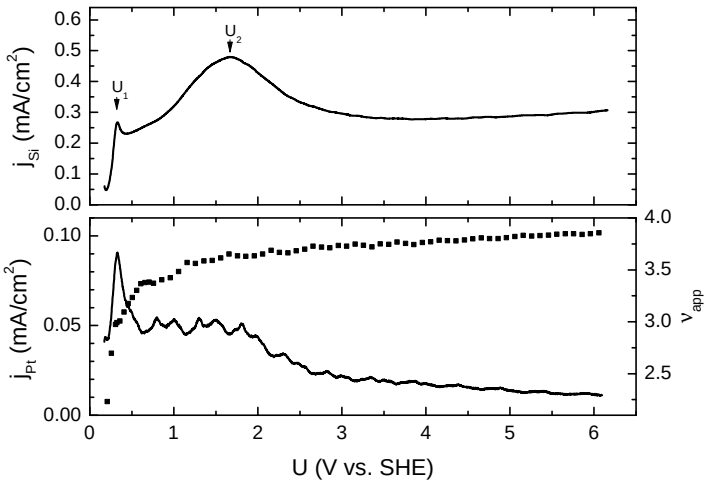

Figure 3.3: Positive voltage scan (5 mV/s) **at p-Si electrode** (c_F = 50 mM, pH = 2.3)**; Top: Current density j_{Si} at the p-Si working electrode; Bottom: Corresponding H_2 oxidation current at Pt-Wire corrected for collection efficiency normalized to the p-Si working electrode surface area (line, left scale) and reaction valency ν (squares, right scale).**

The reaction valency ν can be calculated directly from the H_2 oxidation current at the Pt-wire I_{Pt} corrected for collection efficiency and time delay as described in Sec.(2.3.4) and the current at the silicon working electrode I_{Si} in the flow cell setup in the following way [48]:

$$\nu = \frac{4}{1 + I_{Pt}/I_{Si}}. \tag{3.1}$$

Although the qualitative shape of the curve is identical with the literature results mentioned above, the values found in our experiments are systematically larger. This can be explained by the lower NH_4F concentration used, leading to a slower etch rate and thus also the suppressing of the chemical dissolution of the partially oxidized Si(II) and correspondingly the H_2 evolution [47].

3.1.3 Current oscillations

As early as 1958 it was established that the potentiostatic electrodissolution of p-doped silicon can proceed in an oscillatory fashion when the applied anodic bias is sufficiently high [37]. To stabilize the otherwise damped oscillations an external resistance connected in series with the working electrode has been found to be indispensable [61]. This external resistance R_{ext} links the voltage drop across the electrode U_{el} to the applied voltage U and the total current I passing through the surface

$$U_{el} = U - R_{ext} \cdot I = U - R_{ext} A \cdot j. \tag{3.2}$$

Thus, the external resistance introduces a coupling between all points at the electrode surface. This coupling is both global, as only the spatial average of the current is relevant, and linear. Note, however, that apart from introducing a coupling between all points, the external resistance is obviously also altering the local dynamics at each point via Eq.(3.2). It thus plays a dual role and the deconvolution of both roles is essential to understand the dynamics of the system. For a wide range of resistance values perfectly uniform oscillations in ξ can be realized, an example of which is shown in Fig.(3.4). The behavior of the electrodissolution of n-doped silicon for sufficiently high illumination is identical to that of p-doped silicon [62]. This can be explained by the fact that the amount of holes in the valence band of the silicon

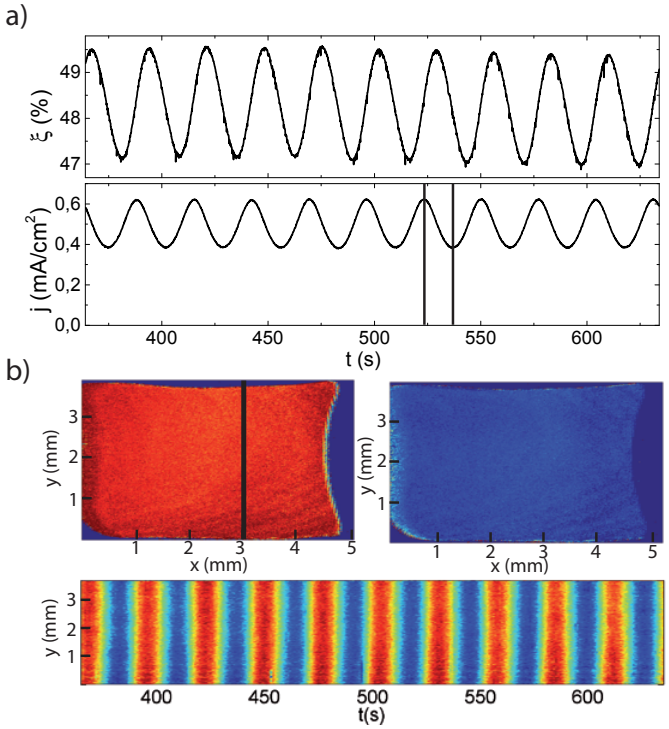

Figure 3.4: Uniform oscillation of ξ on an n-doped sample at a high illumination intensity and under constant potential ($U = 8.65$ V vs. SHE, $c_F = 50$ mM, pH $= 2.3$, $R_{ext}A = 2.7$ kΩcm^2, $I_{ill} = 3.0$ mW/cm^2). a) Time series of the global quantities ξ and j; b) Ellipsometric intensity distribution on the electrode for the two points in times indicated in a) and the temporal evolution of a 1d cut along the line indicated in the left electrode picture. Red indicates a relatively high and blue a relatively low value of ξ.

is in this case always sufficient to maintain the current determined by the electrochemical parameters. The oscillations arise from a Hopf bifurcation occurring at a minimal, electrolyte specific threshold value of the external resistance as shown in Fig(3.5) [63]. With an increase of the external resistance first stable, sinusoidal oscillations with amplitudes increasing with the external resistance are found. This is the expected behavior close to a Hopf bifurcation. Upon further increase of R_{ext} the shape of the oscillations then gradually changes towards a more relaxational type. Above another electrolyte specific threshold value of $R_{ext}A$ the oscillations vanish abruptly and instead the system relaxes to a stable steady state. The extent of the oscillatory regime is thus determined by a Hopf bifurcation at the low coupling limit and a cut-off caused by leaving the experimental parameters for a stable oxide in the high coupling limit.

3.1.4 Boundaries of the oscillatory regime

The upper boundary of the oscillatory regime with respect to the external resistance can be well understood by comparing the voltage drop across the interface in this case as shown in Fig.(3.5) to the CV scan shown in Fig.(3.1). The latter shows that the value of U_{el} for $R_{ext}A$ above the boundary of the oscillatory regime is in the voltage region where no stable oxide can form. When approaching this limiting resistance from lower resistance values a critical slowing down can be seen where the non-oscillatory transient preceding the first oscillation peak becomes gradually longer when the system is initialized in an oxide free state. At the limiting resistance this transient time then diverges. In Fig.(3.6) the initial transients are shown for values of the parameter $R_{ext}A$ around the critical value of ca. $R_{ext}A \approx 7$ kΩcm^2.

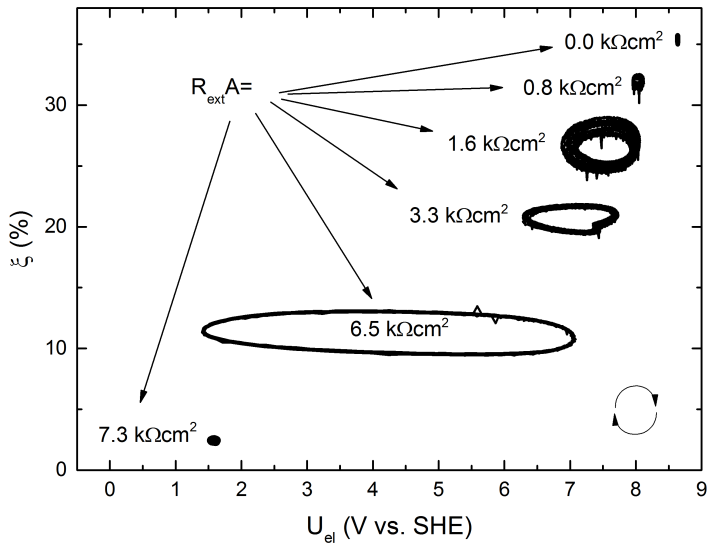

Figure 3.5: Phase space plots of spatially averaged time series measured during the photoelectrodissolution of highly illuminated n-doped silicon (U = 8.65 V vs. SHE, c_F = 75 mM, pH = 1) with varying $R_{ext}A$. The arrows in the lower right hand corner indicate the direction of rotation for all curves.

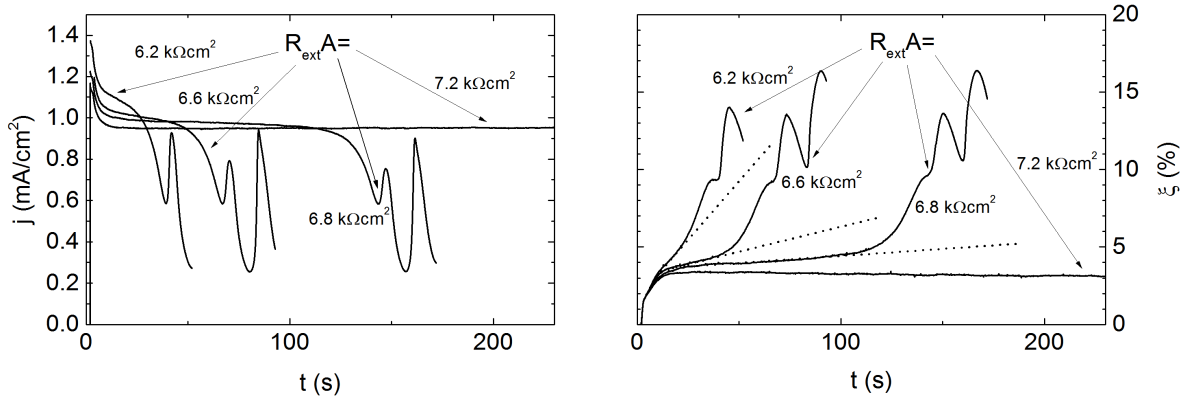

Figure 3.6: Critical slowing down for parameter values at the border of the oscillatory region in parameter space (U = 8.65 V vs. SHE, c_F = 75 mM, pH = 1). Current transients (left) and transients of the ellipsometric intensity (right) are shown together with the linear extrapolation of the slope directly after the initial jump (dash).

The critical slowing down is clearly visible for the current transients. Whether a stable oxide layer forms seems to be decided after a few seconds where a positive slope in the ellipsometric intensity and thus the oxide layer mass has to be present. This slope gradually moves to zero when the critical value for $R_{ext}A$ is approached which also means that it takes longer and longer to establish the oscillatory oxide layer. The critical value of the external resistance is thus relevant for establishing the oxide and not a property of the dynamical system.

What happens then when as an initial condition an already formed oxide is used? In this case, indeed oscillations can be observed at parameter values of $R_{ext}A$ significantly higher than the critical value for an oxide free initial condition. It is then possible to study the high resistance limit of the oscillatory parameter regime in the oscillatory medium. It turns out that the oscillation amplitude decreases significantly with increasing resistance and that, close to the critical value where the oscillations vanish, the oscillations become sinusoidal. A series of phase space plots in this parameter range is shown in Fig.(3.7).

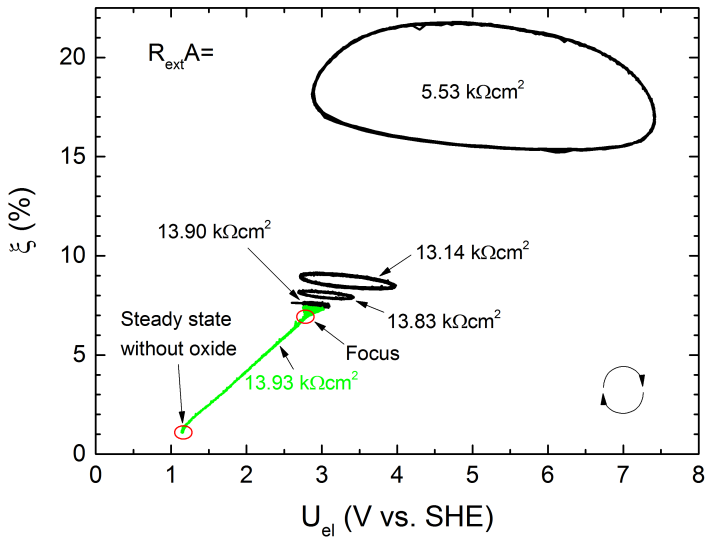

Figure 3.7: Phase space plots of spatially averaged time series measured during the electrodissolution of p-type silicon ($U = 8.65$ V vs. SHE, $c_F = 50$ mM, pH = 2.3). The arrows in the lower right hand corner indicate the direction of rotation for all curves. Stable oscillations (black) are shown together with a measurement of a stable focus followed by a vanishing of the oxide layer (green). All measurements were initialized with the oscillatory state at $R_{ext}A = 5.53$ kΩcm^2.

This behavior clearly indicates the presence of another Hopf bifurcation. It is an interesting side note that the Hopf bifurcation seems to coincide precisely with the point where the oxide layer itself becomes unstable. In a measurement at $R_{ext}A$ values slightly above the bifurcation point, first the oscillations vanish in a manner typical for a focus and once this has happened the oxide also vanishes. One has to keep in mind that there is nothing indicating that the two phenomena, the vanishing of the oscillations within the oxide layer and the stability of the oxide layer itself, are linked at all, much less that they should coincide at the same parameter value.

3.2 Properties of the oscillations

Upon a potential step from the open circuit potential (OCP), which lies between -0.1 and -0.05 V vs. SHE, to a potential of > 8 V vs. SHE stable current oscillations are obtained at suitable external resistances. We discern the four different prototypical types of oscillations depicted in Fig.(3.8). The amplitudes and frequencies of the oscillations show a strongly varying behavior. Increasing the external resistance from the lowest values where oscillations are obtained ($R_{ext}A \approx 2$ kΩcm^2) first sinusoidal oscillations with a relatively low amplitude are found (Fig.(3.8)a)). When the resistance is increased further the development of a shoulder at the decreasing slope of the previously sinusoidal oscillations can be observed as shown in Fig.(3.8) b). If a threshold value of the external resistance is exceeded (here at ca. $R_{ext}A = 3.7$ kΩcm^2), the amplitude and also the frequency of the oscillations increases dramatically, the latter by a factor of 2, and oscillations as shown in Fig.(3.8)c) are found. Upon further increase of the external resistance, resistance intervals where these regular oscillations with a comparatively high amplitude are observed and intervals where chaotic oscillations with a comparatively low amplitude (Fig.(3.8) d)) are observed, alternate. Fig.(3.9) shows the change in the average current density and oscillation frequency depending on the external resistance. It is obvious that the regular high amplitude oscillations shown in Fig.(3.8) c) are strongly different from the other oscillation types. Remarkably, the frequency of the high

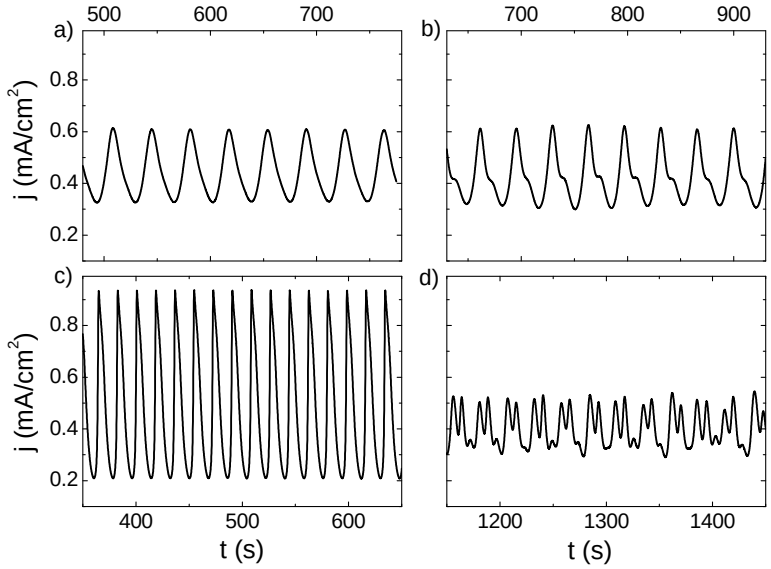

Figure 3.8: Different oscillation types at an applied voltage of $U = 8.15$ V vs. SHE **with different external resistances for** $c_F = 50$ mM **and** pH = 2.3**. a)** $R_{ext}A = 2.69$ kΩcm^2**, b)** $R_{ext}A = 3.59$ kΩcm^2**, c)** $R_{ext}A = 6.28$ kΩcm^2**, d)** $R_{ext}A = 7.30$ kΩcm^2**.**

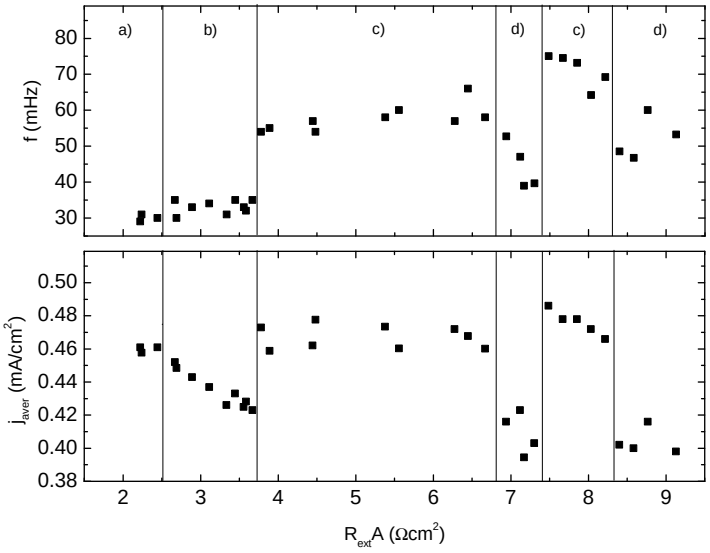

Figure 3.9: Oscillation base frequency (top) and average current density (bottom) during the current oscillations as a function of the parameter $R_{ext}A$ **(**$U = 8.15$ V vs. SHE**,** $c_F = 50$ mM**,** pH = 2.3**).**

amplitude current oscillations is about twice as high as the frequency of the low amplitude current oscillations with and without a shoulder. The difference of the oscillation types can be stressed further taking a look at the average current during the oscillations compared to the current during a cyclic voltammogram with a slow scan rate. This comparison is shown in Fig.(3.10). While the low amplitude current oscillations with and without a shoulder (Fig.(3.8) a,b)) and the foci at low resistance values are in excellent agreement with the cyclic voltammogram, the high amplitude current oscillations and also the chaotic oscillations have a significantly higher average current density than expected. The lower boundary in the average voltage drop across the electrode of the oscillatory regime then coincides with the descending slope of the CV scan, where the high resistance foci are again in good agreement with the CV.

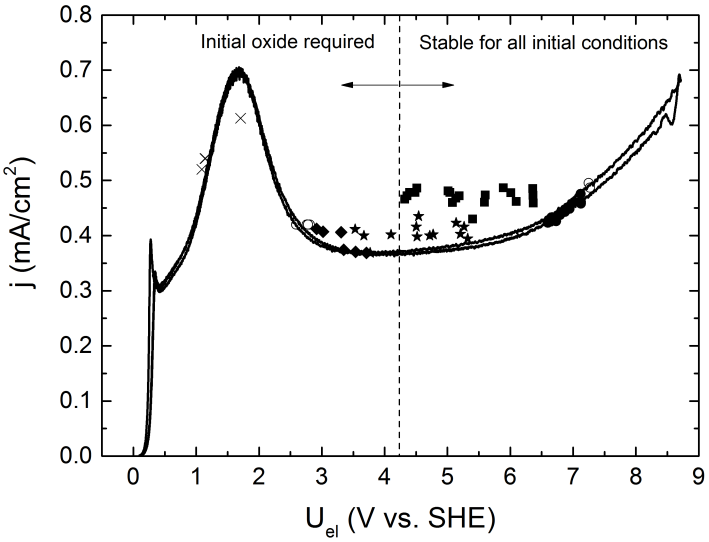

Figure 3.10: Cyclic voltammogram of a p-Si (111) sample ($c_F = 50$ mM, pH $= 2.3$) with a scan rate of 2 mV/s together with a collection of points marking the average current density as a function of the average voltage drop across the electrode of low amplitude current oscillations with and without a shoulder (filled circles), high amplitude current oscillations (squares), chaotic oscillations (stars), sinusoidal oscillations at high resistances (diamonds), foci (empty circles) and oxide free steady states (crosses). The vertical dashed line separates the oscillations found independently of the initial conditions and those that require an existing oxide as initial condition.

The fact that they coincide with a descending slope, i.e. a negative differential resistance, in the CV might then explain why the oxide layer is unstable at these foci. Fig.(3.10) is inconclusive on the question whether also the high resistance sinusoidal oscillations are in agreement with the CV scan, but they seem to be reasonably close. The overall picture of the oscillatory behavior of the system is then the following: Close to its limiting Hopf bifurcations it oscillates in a sinusoidal manner and the average current and voltage drop across the electrode are in agreement with the values expected from a quasi-stationary cyclic voltammogram. In between these limiting cases, the average current is significantly higher than expected and high amplitude current oscillations or chaotic oscillations occur.

3.2.1 Reaction valencies during the oscillations

The hydrogen current measured at the platinum wire in the flow cell setup during the oscillations and the corresponding reaction valency are shown in Fig.(3.11). For all oscillation types except the high amplitude current oscillations the reaction valency of $\nu \approx 3.9$ is in good agreement with the values for the given average voltage drops across the electrode ($\overline{U_{\mathrm{el}}} \approx 7$ V vs. SHE) expected from the cyclic voltammogram from an extrapolation of the positive voltage scan in Fig.(3.3). For these oscillation types no oscillation of the H_2 oxidation current above the noise limit can be seen. A contrary picture arises for the high amplitude current oscillations. In this case the reaction valency is even higher than for the other oscillation types, while the lower average voltage drop across the electrode would lead to the expectation of a lower reaction valency. Thus, the high amplitude current oscillations are again not in agreement with the cyclic voltammetry. Furthermore, the hydrogen oscillation current clearly oscillates for this type of oscillations in accordance with literature data [48]. Interestingly the same oscillatory behavior can be seen during the transient high amplitude current oscillation preceding the sustained low amplitude current oscillations with a shoulder (black curves in Fig.(3.11)). It is then interesting to investigate the phase correlation between the oxidation

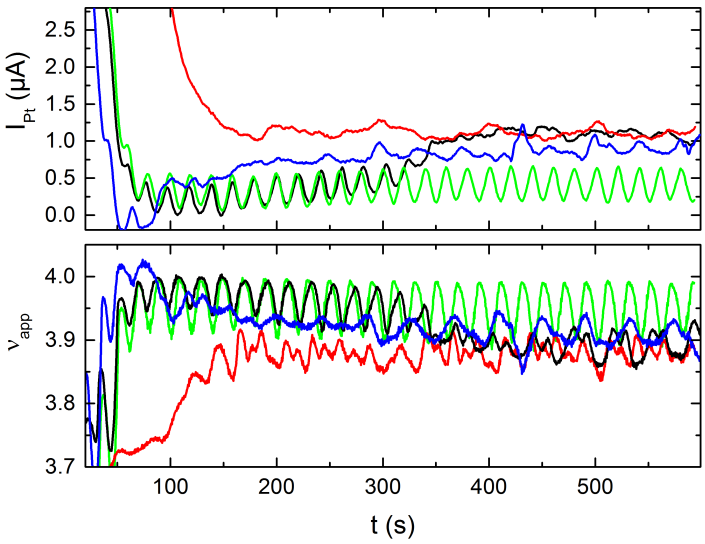

Figure 3.11: Top: H_2 oxidation current at the Pt wire corrected for the collection efficiency during the turn-on transient and sustained low amplitude current oscillation as shown in Fig.(3.8) a) (blue), low amplitude current oscillations with a shoulder as shown in Fig.(3.8) b) (black), high amplitude current oscillations as shown in Fig.(3.8) c) (green) and chaotic oscillations as shown in Fig.(3.8) d) (red); Bottom: Corresponding reaction valency ν ($U = 8.15$ V vs. SHE, $c_F = 50$ mM, pH $= 2.3$).

current oscillations and the hydrogen current oscillations. This is done in Fig.(3.12), where the high amplitude current oscillations are shown together with the H_2 oxidation current in the rotating ring disk setup.

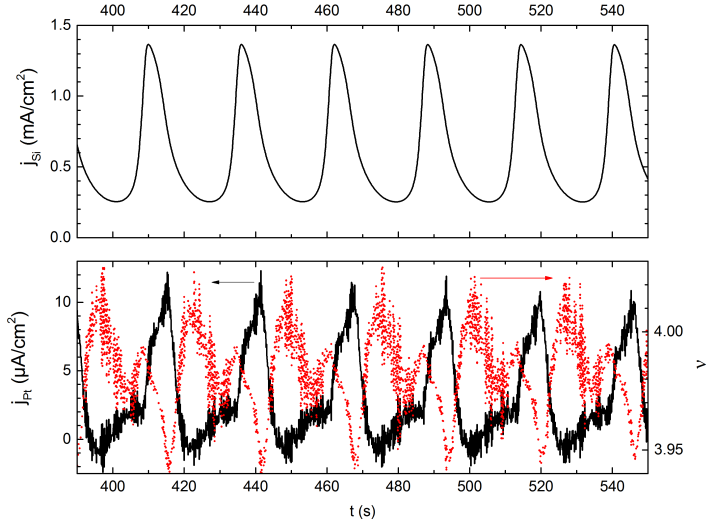

Figure 3.12: Phase dependence of the silicon oxidation current and the corresponding hydrogen current measured in the rotating ring-disk setup ($U = 8.65$ V vs. SHE, $c_F = 50$ mM, pH $= 2.3$, $R_{ext}A = 4.0$ kΩcm^2, Rotation rate: 2000 rpm). Top: Silicon oxidation current at the p-Si working electrode; Bottom: H_2 oxidation current at the Pt-ring corrected for the collection efficiency of ca. 10% and normalized to the silicon area (black, left scale) and corresponding reaction valency (red, right scale).

From Fig.(3.12) it can be concluded that the dominant peak of the H_2 evolution shows a significant phase lag with respect to the current peak and that its amplitude is below 1% of that of the oxidation current oscillations. This means that in the case of the high amplitude current oscillations, the resulting deviation in the reaction valency is very small and in the following

analysis we thus assume a constant value of $\nu \approx 4$ as a good zeroth order approximation.

3.2.2 Correlation between current and ellipsometric intensity

As the current through the silicon surface exclusively leads to the production of SiO_2 as seen in Eq.(2.15), it is possible to quantify the mass of the silicon oxide produced by measuring the current once ν is determined from the independent H_2 measurement. At the same time this silicon oxide is etched away leading to the following overall silicon oxide mass per unit area μ [40]

$$\mu = \frac{M_{\mathrm{SiO_2}}}{F\nu} \int_{t_0}^{t_1} j(\tau) d\tau - \int_{t_0}^{t_1} \dot{\mu}_E(\tau) d\tau + \mu_{\mathrm{av}}. \tag{3.3}$$

Here F is the Faraday constant, $M_{\mathrm{SiO_2}}$ the molar mass of the silicon oxide and ν the reaction valency, i.e. the averaged number of charge carriers from the electrode leading to silicon oxidation, $\dot{\mu}_{\mathrm{E}}$ the etch rate and μ_{av} the average silicon oxide mass density per unit area. Note that we do not make any assumption for the oxide density as usually made in the literature [64, 65, 66, 67, 63]. At the same time the ellipsometric intensity is also a measure of the silicon oxide mass density per unit area which can therefore also be written in the following way:

$$\mu = c_{\mathrm{opt}}(\widetilde{\xi})(\widetilde{\xi} - \xi_0) =: c_{\mathrm{opt}}(\xi) \cdot \xi. \tag{3.4}$$

Here, $\widetilde{\xi}$ is the measured ellipsometric intensity, $c_{\mathrm{opt}}(\xi)$ is a parameter dependent on the details of the optical setup and ξ_0 is the value of the ellipsometric intensity with no silicon oxide at the surface. In any regime of sustained oscillations the time average of the etch rate per unit area $\overline{\dot{\mu_{\mathrm{E}}}}$ is given by:

$$\overline{\dot{\mu_E}} = \frac{M_{\mathrm{SiO_2}}}{F\nu} \cdot \frac{1}{t_1 - t_0} \int_{t_0}^{t_1} j(\tau) d\tau =: \frac{M_{SiO_2}}{F\nu} \cdot j_{\mathrm{av}}, \tag{3.5}$$

with $t_1 - t_0$ being any integer multiple of the oscillation period. If additionally to a constant etch rate no significant variation of the optical parameter is assumed, $c_{\mathrm{opt}}(\xi_{\mathrm{av}})$ can be determined using a least square fit (MATLAB) to fit the measured deviation of the ellipsometric intensity from this average value $(\xi(t) - \xi_{\mathrm{av}})$ to the integral over the measured deviation of the current from the average current.

$$\begin{aligned} c_{\mathrm{opt}}(\xi_{\mathrm{av}})(\xi(t) - \xi_{\mathrm{av}}) &= \frac{M_{\mathrm{SiO_2}}}{F\nu} \int_{t_0}^{t_1} j(\tau) - j_{\mathrm{av}} d\tau \\ \Leftrightarrow c_{\mathrm{opt}}(\xi_{\mathrm{av}}) \cdot \xi(t) &= c_{\mathrm{opt}}(\xi_{\mathrm{av}}) \cdot \xi_{\mathrm{av}} + \frac{M_{\mathrm{SiO_2}}}{F\nu} \int_{t_0}^{t_1} j(\tau) - j_{\mathrm{av}} d\tau \end{aligned} \tag{3.6}$$

During the low amplitude current oscillations shown in Fig.(3.8)a,b) the amplitude of the potential variations is only about 10-20 % of the distance from its average value to the OCP at ca. -0.1 V vs. SHE as seen in Fig.(3.5). Additionally, the optical parameter $c_{\mathrm{opt}}(\xi)$ is assumed to be constant as the relative change in the ellipsometric intensity ξ is also below 20 % (Fig.(3.5)) and changes in this parameter are expected to be small for this case [55]. We assume furthermore a uniform oxide quality in growth direction and a constant etch rate. Under the assumptions made, the optical parameter of the average value of the ellipsometric intensity $c_{\mathrm{opt}}(\xi_{\mathrm{av}})$ and thus the value of the oxide mass per unit area μ can be calculated using Eq.(3.6). The results of the fitting procedure are shown in Figs.(3.13) and (3.14).

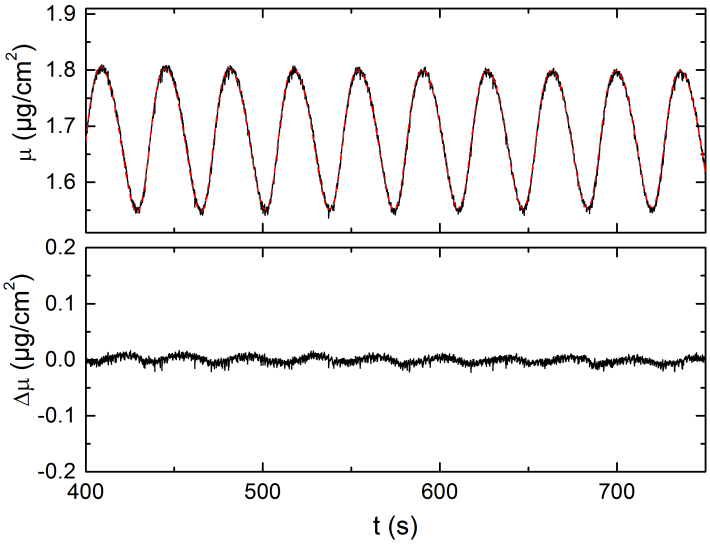

Figure 3.13: Top: Silicon oxide mass density μ for sinusoidal, low amplitude current oscillations as shown in Fig.(3.8) a) calculated according to Eq.(3.6) from the measured ellipsometric intensity (solid) and the measured current (red dash), respectively ($U = 8.15$ V vs. SHE, $c_F = 50$ mM, $R_{ext}A = 2.7$ kΩcm^2); Bottom: Difference $\Delta\mu$ of the two curves in the top panel (to scale).

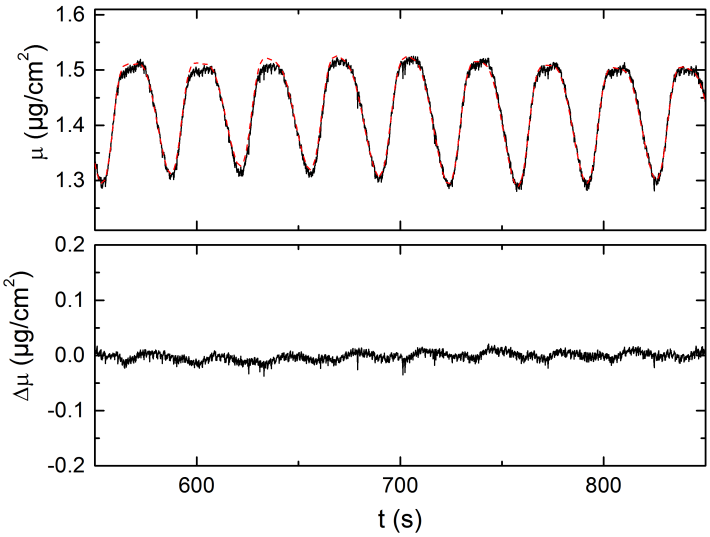

Figure 3.14: Top: Silicon oxide mass density μ for low amplitude current oscillations with shoulder as shown in Fig.(3.8) b) calculated according to Eq.(3.6) from the measured ellipsometric intensity (solid) and the measured current (red dash), respectively ($U = 8.15$ V vs. SHE, $c_F = 50$ mM, $R_{ext}A = 3.6$ kΩcm^2); Bottom: Difference $\Delta\mu$ of the two curves in the top panel (to scale).

For both oscillation types the fit is very good, corroborating the assumption of a constant etch rate during the oscillations. In contrast, for the high amplitude current oscillations the fitting procedure does not yield a satisfying agreement of the oxide mass density per unit area obtained by ellipsometric intensity and current, respectively, as shown in Fig.(3.15). Hence, the assumptions of a constant optical parameter $c_{opt}(\xi)$ and a constant etch rate during the oscillations, do not both hold in this case. Again the high amplitude current oscillations stand out in their behavior.

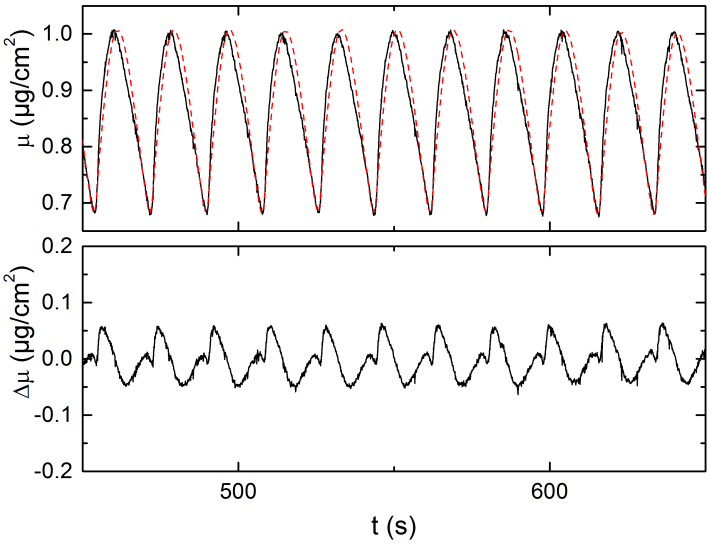

Figure 3.15: Top: Silicon oxide mass density μ for low amplitude current oscillations with shoulder as shown in Fig.(3.8) c) calculated according to Eq.(3.6) from the measured ellipsometric intensity (solid) and the measured current (red dash), respectively ($U = 8.15$ V vs. SHE, $c_F = 50$ mM, $R_{ext}A = 6.3$ kΩcm^2); Bottom: Difference $\Delta\mu$ of the two curves in the top panel (to scale).

3.2.3 Bistability

In this part we want to briefly return to the type of oscillations that has been left out from the discussion so far, namely the chaotic oscillations. The fact that they appear in windows within the parameter regime where also the high amplitude current oscillations exist and that both types of oscillations are well above the CV scans (see Fig.(3.10)) points to a shared oscillatory mechanism. The question is then what distinguishes which of the two types of oscillations is expressed at given parameters. Here we have evidence that this distinction is brought about by the initial conditions and not by the parameters themselves, i.e. that the system is bistable in parts of the $R_{ext}A$ parameter space. In Fig.(3.16) time series of oscillations initialized with different initial conditions are shown.

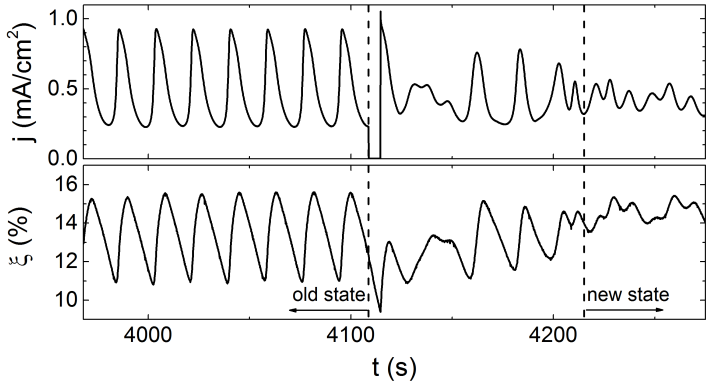

Figure 3.16: Time series of the current j (top) and the ellipsometric intensity ξ (bottom) of a high amplitude current oscillation initialized with an oxide free electrode (old state until ca. 4110 s) and a chaotic oscillation initialized with some oxide layer ($\xi \approx 10$ %) after a short interruption of the external bias and corresponding partial etching of the oxide layer at a highly illuminated n-doped electrode ($U = 8.65$ V vs. SHE, $c_F = 50$ mM, pH $= 2.3$, $R_{ext}A = 6.7$ kΩcm^2, $I_{ill} = 5.9$ mW/cm^2).

When the sample is initialized without an oxide layer, stable high amplitude current oscil-

lations form. In contrast to this, when some oxide layer is already present at the moment of initialization, the sample shows a chaotic oscillation. This behavior is accompanied by a shift in the average ellipsometric intensity ξ_{av} and is a clear indicator for the presence of a bistability in parameter space. This then has to be kept in mind as identical initial conditions are thus indispensable when interpreting broad scans of parameter space.

3.3 Summary and Discussion

Our experiments give evidence that oscillations in different parameter regimes involve different physico-chemical processes. The dynamic behavior during the anodic dissolution of silicon in fluoride containing electrolytes is thus even richer than previously assumed (for a summary see [38], chap. 5). Yet, the picture becomes also more structured. There are two main types of oscillations, namely the low amplitude current oscillations shown in Fig.(3.8) a) and the high amplitude current oscillations shown in Fig.(3.8) c). Some of their properties are summarized in Tab.(3.1).

	Low amplitude	High amplitude
U_{el} [V vs. SHE]	6-7.5	2-7.5
j_{av}	$\approx j_{\mathrm{CV}}$	$> j_{\mathrm{CV}}$
f	f_0 (ca. 30 mHz)	ca. $2f_0$
oxide quality	uniform	non-uniform
ν	constant (3.9), fits CV	oscillating (3.9-4), larger than in CV

Table 3.1: Summary of oscillation properties differing for low and high amplitude current oscillations. The numerical values are given for the following parameters ($U = 8.15$ V vs. SHE, $c_{\mathrm{F}} = 50$ mM, pH $= 2.3$).

The low amplitude current oscillations occurring at larger values of the voltage drop across the electrode U_{el}, do not involve different oxide qualities, implying that the oxide volume density or properties such as internal stress remain constant during the oscillations. This can be concluded from the extremely good agreement between oxide mass area density μ determined from the ellipsometric signal and from the integral of the current. This also substantiates the conclusion that the oxide is etched at a constant rate. Finally, we know that the oscillations are only stable if there is a sufficiently large ohmic resistance in series to the interface [61], implying that electrical quantities are essential for the oscillation inducing instability.

In contrast, the high amplitude current oscillations leave room for different oxide qualities as well as different etch rates. Furthermore, they are not in accordance with the cyclic voltammograms of the silicon system. This suggests that the high amplitude current oscillations are qualitatively different from the low amplitude current oscillations and that additional variables might play a role. The occurrence of parameter windows where chaotic oscillations occur underscores this, as these require at least one additional degree of freedom as compared to the necessary conditions for oscillations to occur. Observe, however, that the large amplitude current oscillations are not separated in phase space from the low amplitude current oscillations. It is, therefore, possible that the primary instability is the same. This notion is underlined further by the occurrence of the low amplitude current oscillation with a shoulder (Fig.(3.8) b)) at intermediate values of $R_{\mathrm{ext}}A$. These oscillations seem to mediate between low amplitude and high amplitude current oscillations sharing the relatively low amplitude and the base frequency with the former ones, while the first superharmonic component of the frequency, coinciding with the frequency of the latter ones, is already present.

4 Origin of the oscillations

When you have excluded the impossible, whatever remains, however improbable, must be the truth.
(Arthur C. Doyle/Sherlock Holmes)

In this chapter we discuss the oscillation mechanism. To do so, in a first step, the experimental findings from our and other groups are used to identify the essential variables for the oscillations. In a second step, experiments to investigate the oxide properties in growth direction are presented. The main tool for this will be etch-back experiments where the electrical properties of the oxide are investigated while it is etched away in the absence of an applied voltage. Finally, model efforts discussed in the literature will be presented and scrutinized concerning their viability in the light of the experimental findings.

4.1 Essential variables

As a first step, in this part we want to focus on investigating which parts of the system play a role in the oscillation mechanism and which ones can be safely excluded. Of special importance is the positive feedback loop which sustains the oscillations. As was shown in the last chapter there are at least two qualitatively different types of oscillations to be considered, the low amplitude current oscillations with and without a shoulder and the high amplitude current oscillations. We focus here on the high amplitude current oscillations as sinusoidal oscillations with a decreasing amplitude are the expected behavior close to the Hopf bifurcation giving rise to the oscillations. The mechanism for the low amplitude current oscillations might then be derived in a second step in the future.

4.1.1 Current vs. potential oscillations

For potentiostatic oscillations with an external resistance the current is directly linked to the voltage drop across the electrode U_{el} via Eq.(3.2). When the time evolution of this voltage drop is regarded, the resulting oscillation has a very strong resemblance to galvanostatic potential oscillations found in the same system. In Fig.(4.1) a comparison between such a galvanostatic measurement from the literature and one of our potentiostatic measurements is shown. The qualitative similarity between both time series is striking while some differences, especially in the magnitude of the average voltage drop across the electrode remain. It is then interesting to find a more direct method to compare potentiostatic with galvanostatic measurements. We achieve this by using a current limiter connected in series with the working electrode and the external resistance as described in the end of Sec.(2.1.3). This limiter cuts off the current above a preset threshold value j_{lim} and while the current is in the limited regime the measurement is then effectively under galvanostatic control. The measurement of the potential drop at the limiter makes it possible to record time series of the voltage drop across the interface. Examples for such measurements where the method of control changes, ranging from potentiostatic control with external resistance to purely galvanostatic control are shown in Fig.(4.2). The most remarkable feature of the measurements conducted under varying methods of control is the fact that the phase space plots are not in any way visibly disturbed by these changes.

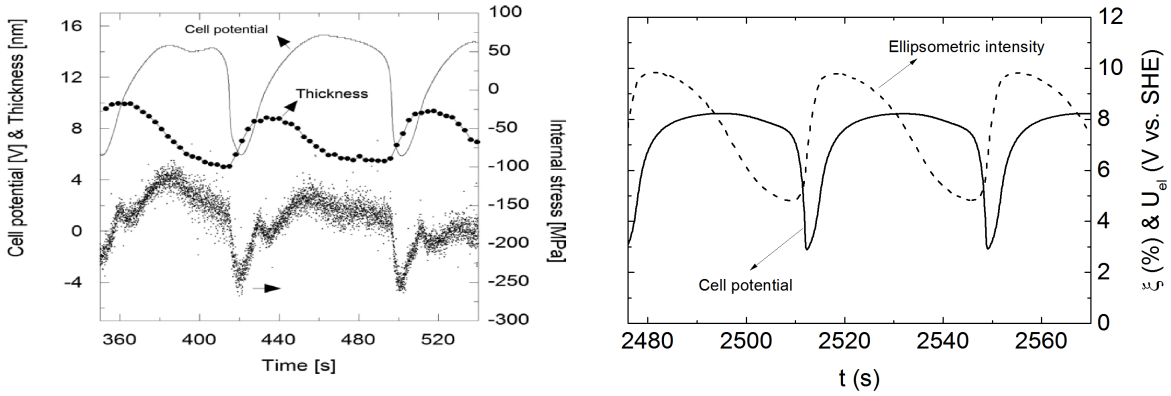

Figure 4.1: Comparison between galvanostatic potential oscillations (vs. Ag|AgCl(0.95 M)=0.24 V vs. SHE) from the literature (left, $j = 0.5$ mA/cm^2, $c_F = 50$ mM, pH ≈ 3) (Ref.[68] Reproduced by permission of The Electrochemical Society) and current mediated oscillations in the voltage drop across the electrode under potentiostatic control with an external resistance (right, $U = 8.65$ V vs. SHE, $c_F = 75$ mM, pH $= 3.5$, $R_{ext}A = 3.6$ kΩcm^2). The thickness curve in the left hand graph can be compared to the ellipsometric intensity in the right hand graph.

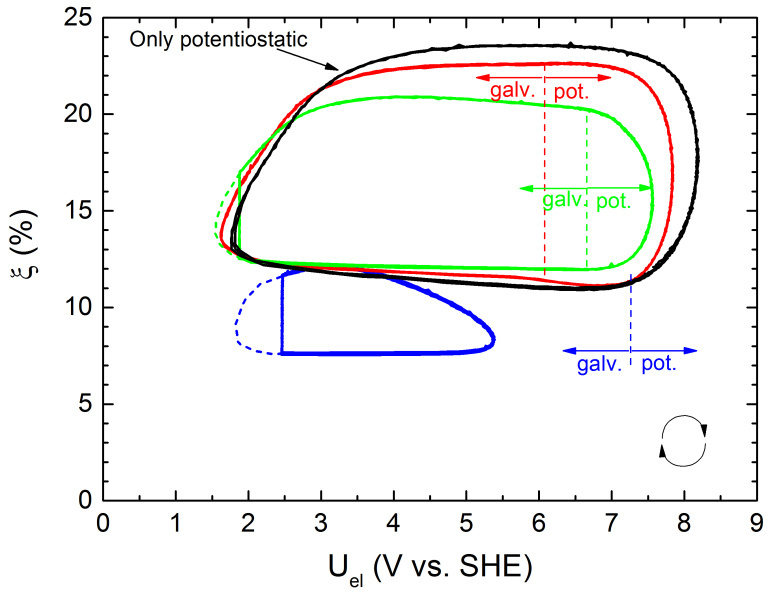

Figure 4.2: Comparison between potentiostatic high amplitude current oscillations at $R_{ext}A = 6.1$ kΩcm^2 (black) and mixed control oscillations at $R_{ext}A = 4.1$ kΩcm^2 and limiting currents of $j_{lim} = 0.63$ mA/cm^2 (red), $j_{lim} = 0.49$ mA/cm^2 (green) and $j_{lim} = 0.34$ mA/cm^2 (blue) for $U = 9.15$ V vs. SHE, $c_F = 75$ mM, pH $= 3.5$. The arrows in the lower right hand corner indicate the direction of rotation for all curves and the vertical dashed lines indicate the voltage drop across the electrode at which the method of control switches $U_{el,switch} = U - R_{ext}Aj_{lim}$. Note that the sharp cut-off at low values of the voltage drop across the electrode visible in the green and blue curves is an artifact. The dashed curves give a qualitative picture of the real shape of the curves.

Instead, the curves pass the points where the method of control changes in a continuously differentiable manner as evident from the behavior of the phase space plots in Fig.(4.2) at the dashed lines marking the potential where the method of control switches. It is as though the system always remembers what the voltage drop across the electrode is supposed to be at a given point in time. This information has to be stored somewhere in the system. In this view the oscillating current in the potentiostatically controlled measurements is the means of

the system to establish the desired potential via the IR-drop across the external resistance under the restriction of the fixed control potential. There is a strong similarity between potentiostatic and mixed control measurements and the differences are similar to those arising by changing the external resistance for a comparable series of purely potentiostatically controlled measurements. Even the purely galvanostatic measurement shown (blue curve in Fig.(4.2)) ties in nicely with the behavior of potentiostatic measurements with an external resistance for increasing external resistances, namely a decreasing ellipsometric intensity and amplitude as for example shown in Fig.(3.7). Note that the lower potential cut-off for the green and blue curves in Fig.(4.2) is an artifact introduced by the 5V overflow limit of the voltmeter measuring the potential drop at the current limiter and not connected to the cut-off itself. It is not influencing the measurement. Another important similarity strongly corroborating the view of a unified oscillatory mechanism for potentiostatic and galvanostatic oscillations is the frequency of the measurements shown in Fig.(4.2) which is in the narrow range of $31 - 35$ mHz comparable to the relative range for potentiostatic high amplitude current oscillations at different parameter values shown in Fig.(3.9). In line with the view formulated by other groups [68] we thus conclude that potentiostatic and galvanostatic oscillations arise from the same basic phenomenon and that the voltage drop across the electrode, U_{el}, rather than the current, is an essential, dynamical variable of the system.

If the galvanostatic and the potentiostatic oscillations with an external resistance share the same origin, it has to include variations of either the etch rate or the faradaic current for the tetravalent oxidation during the oscillations as the changes in oxide thickness during the galvanostatic oscillations are otherwise not explicable. Since transient potential oscillations of comparable frequency and shape were also found for galvanostatic measurements without etching [69, 70] an oscillating faradaic current for the tetravalent oxide formation should at least play a role. Changes in the faradaic current for the tetravalent oxide formation mean that either the reaction valency changes, i.e. that a varying amount of oxide is formed per unit charge transferred across the interface, or that a part of the current is exchanged with some charge storage for example in the form of trapped charges. In both cases the measured current is not identical with the faradaic current for the oxide formation. In general a mismatch between the oxide layer thickness predicted by the measured current and the measured value of the oxide layer thickness is then to be expected and since such a mismatch was found for the high amplitude current oscillations (see Fig.(3.15)) it lays in the focal point of our interest for the rest of the chapter. Note that the low amplitude current oscillations do not show such a mismatch (see Fig.(3.13)) and that hence an alternative mechanism has to be considered.

4.1.2 Space charge layer

The space charge layer of the silicon electrode with its non-linear current/voltage-characteristics is at first glance a good candidate where the positive feedback mechanism involving charging effects could take place. To investigate its possible role in the oscillation mechanism it is most straight forward to compare measurements with samples of different doping types and levels and thus different space charge layers. Some of the samples investigated are degenerately doped, i.e. they are semimetals for any practical purpose. In this case the space charge layer transforms into a surface charge and the drop in the electrochemical potential across the space charge layer in the electrode is expected to be negligible. In Fig.(4.3) phase space plots showing the typical oscillations are shown for an identical electrolyte and four different doping levels. The non-degenerate n-doped sample is highly illuminated. It is clear from Fig.(4.3) that there is no qualitative variation in the behavior of the four electrodes. The variations

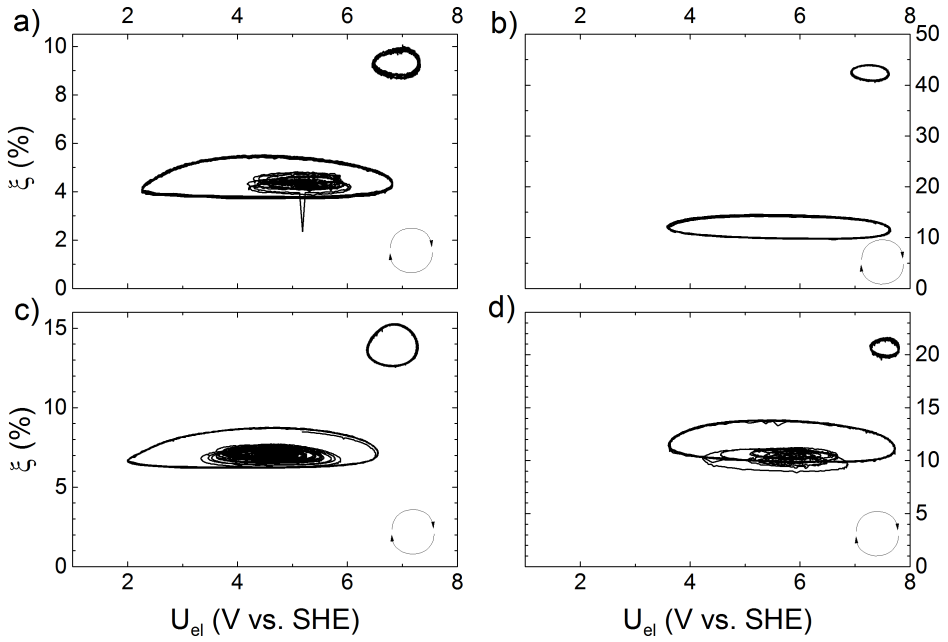

Figure 4.3: Phase space plots for two different doping types (p-Si left, n-Si right) and classes (non-degenerate top, degenerate bottom) at $U = 8.65$ V vs. SHE, $c_F = 50$ mM and pH $= 2.3$. a) p-doped electrode with resistivity $\rho = 1 - 10$ Ωcm corresponding to $n_A \approx 10^{15}$ cm^{-3}; b) highly illuminated ($I_{ill} = 5.9$ mW/cm^2) n-doped electrode with resistivity $\rho > 40$ Ωcm corresponding to $n_D \approx 10^{14}$ cm^{-3}; c) p-doped electrode with resistivity $\rho \leq 0.01$ Ωcm corresponding to $n_D \geq 10^{19}$ cm^{-3}; d) n-doped electrode with resistivity $\rho \leq 0.01$ Ωcm corresponding to $n_A \geq 5 \cdot 10^{18}$ cm^{-3}. The arrows in the lower right hand corners indicate the direction of rotation for all curves.

visible are well within the variations also found for a single electrode at different parameters. We thus conclude that the space charge layer does not play any role for the underlying oscillation mechanism. Furthermore, it does not even seem to have any impact on the details of the shape of the oscillations as long as the illumination is sufficient for the case of n-doped samples. Thus the potential drop across the space charge layer in the electrode can be safely neglected when considering models for oscillatory mechanism although some experimental literature data were interpreted in this direction [65]. Keep in mind that this result is of course not true for n-doped silicon samples illuminated with relatively low illumination intensities. In this case the space charge layer introduces a nonlinear current cut-off, the profound effect of which will be discussed in detail in the following two chapters.

4.1.3 Varying etch rate

Keeping in mind the spatial profile of the electrochemical potential shown in Fig.(2.3), the main feedback mechanism has to be found in an interplay of the kinetics of the electrochemical oxidation reaction which is responsible for η_{reac}, and the profile of the electrochemical potential in the oxide layer at each point in time which is responsible for η_{ox}. The latter is then subject to temporal variations mediated by the formation and etching of the oxide. In a first step, the role of possible variations in the etching process are discussed here. These variations can have various origins two of which will be discussed. First, the etch rate can be current or potential dependent both mediated by changes in the electrolyte composition close to the interface and, second, it can be influenced by the inner surface of the oxide layer when for example the porosity of the oxide layer varies during the oscillations. The latter possibility will be discussed in the next section. A possible influence of the current can be best

understood when the fact that protons are emitted by the electrochemical oxidation reaction as shown in Eq.(2.15) is linked to the pH dependence of the etch rate shown in Fig.(2.5). It is then expected that the pH value is lower than the bulk value throughout the oscillations and that this effect is strongest at the current maximum. This means that in the case of electrolytes with pH values ≤ 2.5, i.e. the pH value with the maximum etch rate, a damping effect is expected. There an increasing current lowers the etch rate which in turn increases the oxide thickness and thus damps the current increase. Conversely, when the pH value lies significantly above 2.5 the opposite is expected. Hence, in this parameter region an increasing current increases the etch rate thus lowers the oxide thickness, thereby enhancing the current increase. In this case thus a positive feedback would be expected. As was shown before, the electrolytes chosen for the experiments have pH values both, above and below 2.5. In all cases a qualitatively identical behavior with high amplitude current oscillations and chaotic oscillations for high values of the external resistance and sinusoidal low amplitude current oscillations for lower values can be found. This shows that a possible current-mediated pH change is not responsible for the oscillations. A possible potential dependence of the etch rate is also not very likely as the etching is mostly carried by HF for a pH value of 1 and by HF_2^- for a pH value of 3.5 as can be concluded from Fig.(2.5). The potential dependence should be different for both species as one is charged and the other is not. Again, the qualitative resemblance of the behavior at pH values of 1 and 3.5 is a strong hint that a relation between etch rate and potential does not seem to be essential for the oscillations.

While current and potential mediated changes of the etch rate do not seem to be responsible for the oscillations, they seem to introduce a higher order effect which is visible when comparing the details of the oscillations for pH values of 1 or 2.3 on the one hand and 3.5 on the other hand. In Fig.(4.4) two time series of both, current and ellipsometric intensity, are compared for two different electrolytes. The time series are both taken at the lower boundary of the $R_{\text{ext}}A$ parameter region where the high amplitude current oscillation are found.

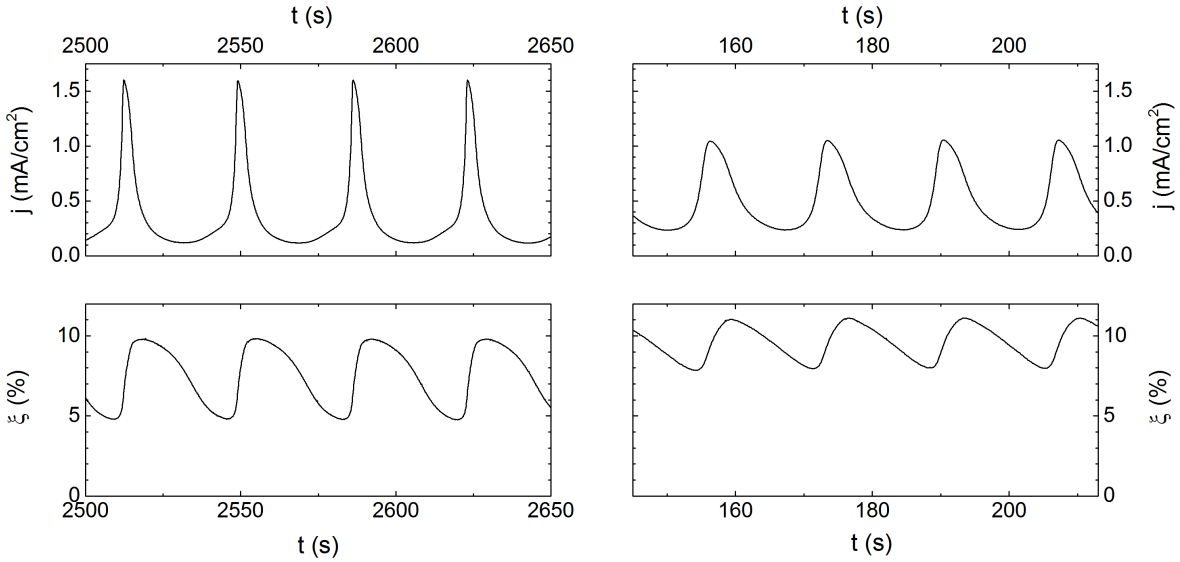

Figure 4.4: Time series of current j (top) and ellipsometric intensity ξ (bottom) of high amplitude current oscillations for relatively low values of $R_{\text{ext}}A = 3.6$ kΩcm^2 for pH $= 3.5$ (left) and $R_{\text{ext}}A = 5.1$ kΩcm^2 for pH $= 1$ (right) ($U = 8.65$ V vs. SHE, $c_{\text{F}} = 75$ mM).

The details of the shape of the oscillations are quite different and in line with the interpretation of a current dependent etch rate and the following positive feedback. The current spikes are sharper for the high pH value while at the same time the ellipsometric intensity

is more rounded than the corresponding curves for the low pH value. The former can then be explained by the fact that each slope of the current oscillations becomes steeper when the assumed positive feedback is present. As for the latter, the negligible decrease of the ellipsometric intensity directly after the sharp current peak is then explained by the relatively small current which then in turn leads to a comparatively low etch rate. This state of a small current and a correspondingly low etch rate can then also be used to explain the comparatively low frequency of the oscillations at the higher pH value as it essentially slows down the entire dynamics of the system. Furthermore, the amplitudes of both current and ellipsometric intensity are higher relative to the mean value of the oscillations for the high pH value than the low pH value. This is again consistent with the positive current feedback as this should lead to generally more pronounced oscillations.

4.1.4 Changes in the oxide properties

As neither the space charge layer nor an etch rate variation due to changes in the chemical environment of the electrode are part of the positive feedback loop necessary to trigger the oscillations, changing properties of the oxide layer itself remain as a viable candidate for introducing the oscillation inducing instability. These properties include structural properties, as e.g. porosity, chemical composition and internal stress, as well as related electrical properties as for example the specific resistivity or capacitance. It is these candidates that our modeling efforts focus on. The structural properties are also a part of many existing modeling attempts in literature. Some of the proposed models rely on periodical changes in the internal stress of the oxide layer as key to the oscillatory dynamics by either leading to the occurrence of cracks [69] or changing the electrical properties of the oxide layer and the etch rate [70, 68] while others assume variations in the lateral distribution of the oxide layer thickness [71, 72, 73]. Changes in the porosity of the oxide film are discussed as a compelling candidate for playing a part in the positive feed-back mechanism underlying the oscillations since an increase in the porosity increases the internal surface of the oxide layer and thus potentially the etch rate, while at the same time the specific resistivity should drop [71, 72]. We did not investigate this ourselves but changes in the porosity do at least not seem to be essential for galvanostatic potential oscillations as such oscillations were also found in the absence of a varying porosity [70, 68].

As a next step we take a first look at the oxide properties in the following way: At different oscillation phases the potential is switched to OCP for varying durations between 1 s and 25 s corresponding to 0.25-1.25 oscillation periods at the parameters chosen. Then the voltage is turned on again and after the oscillatory state stabilized again it is compared to an extrapolation in time of the state before the interruption. In this way the phase shift caused by the interruption can be measured. In Fig.(4.5) such a series is shown for a typical high amplitude current oscillation on highly illuminated n-doped silicon. The left hand graph in Fig.(4.5) shows that after a certain interruption time varying for the different phases a further increase in the interruption time $t_{\text{interrupt}}$ leads to an identical increase of the delay time Δt. For shorter interruption times an advance to this trend line is seen, i.e. the time delay is shorter than the time the voltage was turned off. In some cases the time series after the turn-off is even advanced as compared to the uninterrupted interpolation. The linear behavior of the time delay, while starting at different interruption times for the different turn-off phases, starts around an identical value of the minimal ellipsometric intensity ξ_{min} independent of the turn-off phase. This value is indicated by the vertical dashed line in the right hand graph in Fig.(4.5). We did not so far study this phenomenon systematically but it seems to indicate that the information the system has about its current phase is erased latest when a ξ_{min}

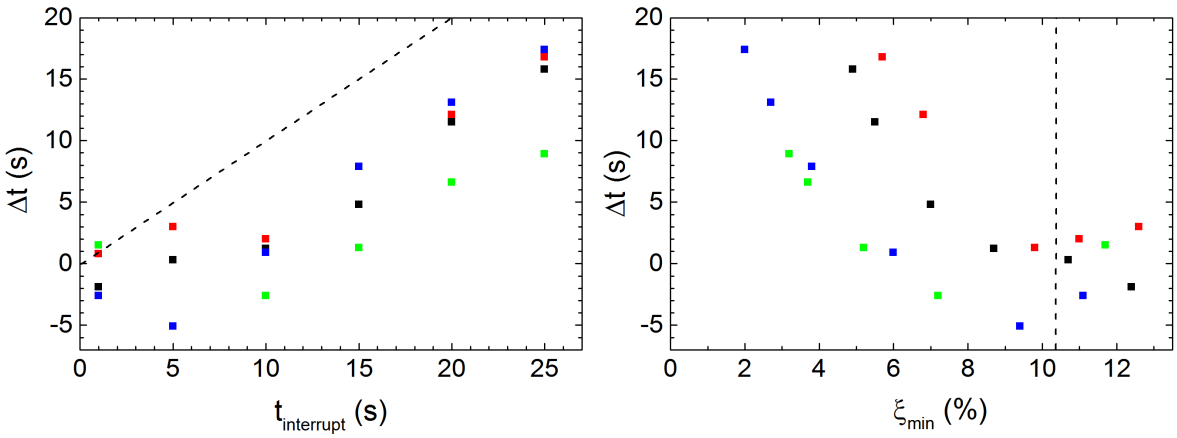

Figure 4.5: Time delay Δt upon an interruption of the potentiostatic driving of the interrupted measurement with respect to the extrapolation of the uninterrupted measurement at different oscillation phases (black: maximum j, red: maximum ξ, green: minimum j, blue: minimum ξ) as function of the duration of the interruption $t_{\mathrm{interrupt}}$ (left) and the minimal value of the ellipsometric intensity at the end of the interruption ξ_{min} (right) ($U = 8.65$ V vs. SHE, $c_{\mathrm{F}} = 50$ mM, pH $= 2.3$, $R_{\mathrm{ext}}A = 6.7$ kΩcm^2, $I_{\mathrm{ill}} = 5.9$ mW/cm^2). The dashed line on the left hand side indicates the identical slope corresponding to no phase shift while the dashed line on the right marks the level of ξ_{min} where the behavior of Δt changes qualitatively.

corresponding to the dashed line in the right hand graph is reached.

4.2 Etch-back characterization of the oxide

For an experimental investigation of the oscillation mechanism we use etch-back experiments. In these experiments the voltage is switched to OCP at four different oscillation phases, the maxima and minima of the ellipsometric intensity and the current, respectively. In a slight variation of these measurements, instead of the OCP also a potential close to but still above the OCP is used. In this way a current can still flow and its magnitude and time delay with respect to the turn-off time offers additional insights into the oxide properties [50, 74]. For this type of measurements presented here typically a value around 0 V vs SHE is used. The phases used for the turn-off and the color code used throughout this section are shown for low and high amplitude current oscillations in Fig.(4.6). In all etch-back experiments the oxide is probed in growth direction. Assuming that some features, as e.g. the chemical composition of the oxide, are frozen in by the drastic reduction of the applied voltage, information about these features as a function of the oscillation phase can be gained. To get an overview of the etch-back experiments we record the decreasing curve of the ellipsometric intensity towards its minimal value ξ_0. Such etch-back curves for the oscillation types shown in Fig.(3.8) a)-c) are shown in Fig.(4.7). For the low amplitude current oscillations in the top of Fig.(4.7) the shape of the etch-back curves $\xi(t)$ is independent of the phase of the oscillation where the potential was turned off leading to the conclusion of a uniform quality of the silicon oxide layer for this type of oscillation. Relatively small variations of the etch-back curves of low amplitude current oscillations with a shoulder with the turn-off phase can be seen in the middle of Fig.(4.7) indicating slight changes in oxide quality. These variations are fully developed for the high amplitude current oscillations in the bottom of Fig.(4.7). Here, the shape of the etch-back curves $\xi(t)$ is strongly dependent on the phase of the oscillation where the potential is turned off. A nonuniform oxide quality in growth direction and thus density variations or variations in the internal stress or composition can be concluded, a finding in line with later

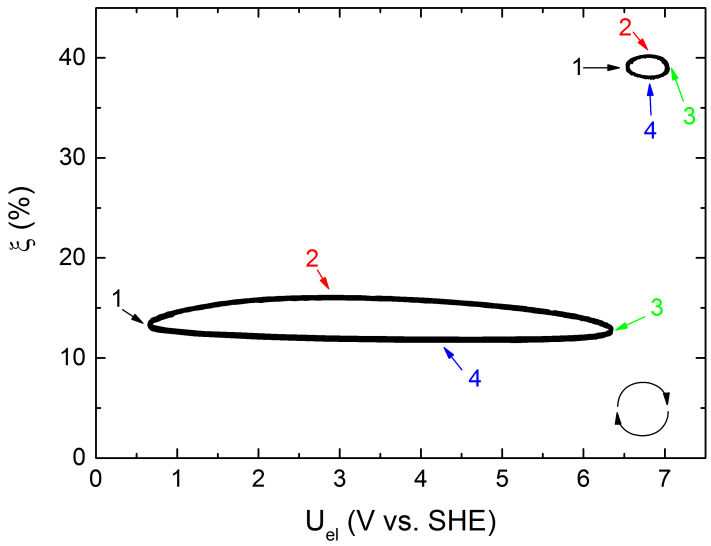

Figure 4.6: Phase space for high and low amplitude current oscillations (U = 8.15 V vs. SHE, c_F = 50 mM, pH = 2.3) used for the etch-back experiments presented in this section. The color coded arrows mark the oscillation phases where the potential is switched off. The black arrows in the lower right hand corner indicate the direction of rotation for all curves.

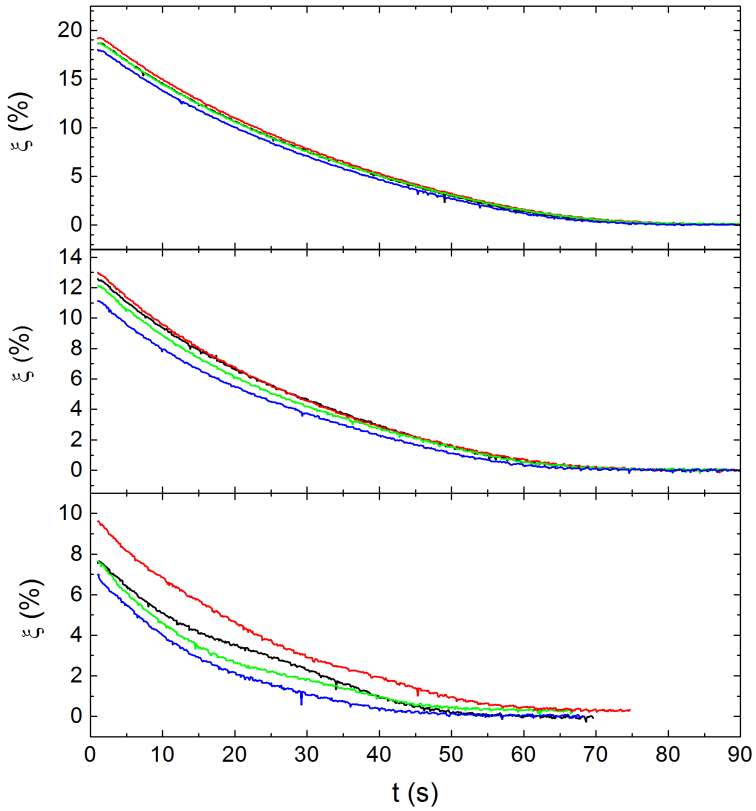

Figure 4.7: Top: Etch-back curves for low amplitude current oscillations as shown in (Fig.3.8) a); Middle: Etch-back curves for low amplitude current oscillations with a shoulder as shown in Fig.(3.8) b); Bottom: Etch-back curves for high amplitude current oscillations as shown in Fig.(3.8) c). The color code is according to Fig.(4.6).

observations from another group [68]. This result coincides with the finding that the fit of the integrated current to the measured ellipsometric intensity as discussed in Sec.(3.2.2) shows significant deviations of both quantities for this type of oscillations.

4.2.1 Chemical properties in growth direction

To probe the non-uniformity of the oxide in growth direction, electrical properties are measured during the etch-back experiments. First, the open circuit potential is tracked during the etch-back experiments and, second, the potential is set to a value slightly above the OCP to track the current during the etch-back without forming a new oxide layer. An overview of these measurements for low and high amplitude current oscillations is shown in Figs.(4.8) and (4.9), respectively.

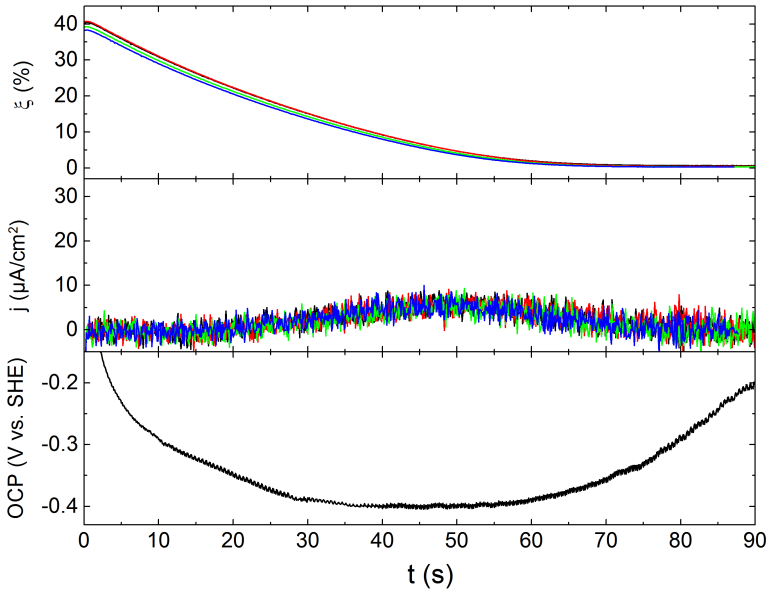

Figure 4.8: Etch-back curves for low amplitude current oscillations as shown in (Fig.3.8) a) with the color code indicating the turn-off phase according to Fig.(4.6); Top: Development of the ellipsometric intensity; Middle: Anodic current during the etch-back at a potential of 50 mV vs. SHE**; Bottom: Development of the open circuit potential for the etch-back started at the current maximum.**

The anodic current found with a low applied potential can then be associated with the presence of partially oxidized species close to the silicon|silicon oxide interface, which are electrochemically oxidized when the covering oxide layer becomes thin enough [50, 75]. A comparison between the development of the current and the OCP shows that indeed the OCP drops at the same time as the current peaks as would be expected for an increasing presence of partially oxidized species close to the surface. The fixed potential during the etch-back then constitutes a higher overpotential for the oxidation of these already partially oxidized species in line with the higher measured current. As evident from Figs.(4.8) and (4.9) the experimental findings for the etch-back measurements again tie in nicely qualitatively with the earlier findings about a uniform oxide quality in growth direction for low amplitude current oscillations and a varying oxide quality in growth direction for high amplitude current oscillations. There is no phase dependence of the anodic current for low amplitude current oscillations while a pronounced dependence is found for high amplitude current oscillations. Hence, we assume that the presence of the partially oxidized species is ruled out as a key factor for the oscillatory mechanism of the low amplitude current oscillations while it may play a significant role for the high amplitude current oscillations to come about. In the following section the latter is

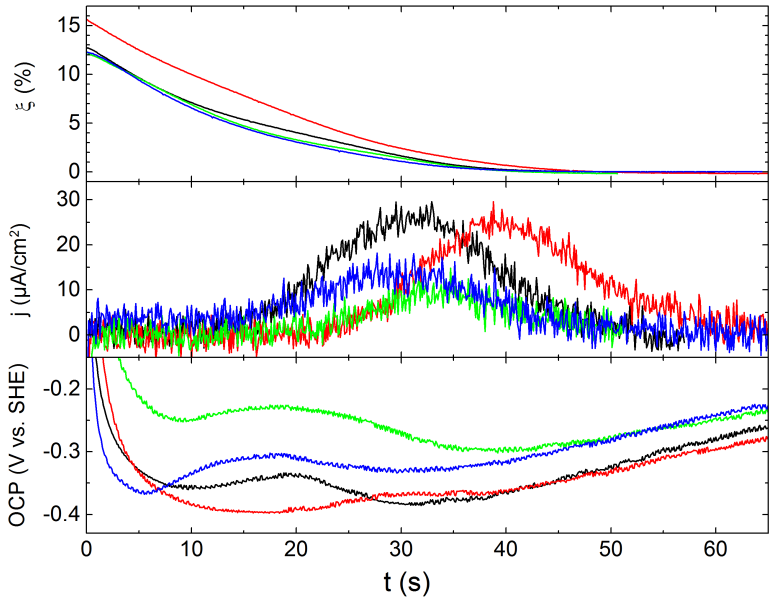

Figure 4.9: Etch-back curves for high amplitude current oscillations as shown in (Fig.3.8) c) with the color code indicating the turn-off phase according to Fig.(4.6); Top: Development of the ellipsometric intensity; Middle: Anodic current during the etch-back at a potential of 50 mV vs. SHE**; Bottom: Development of the open circuit potential.**

investigated. It is then as a first step interesting to know the spatial distribution in growth direction of these partially oxidized species. To visualize this, the anodic etch-back current and the etch-back OCP are plotted against the ellipsometric intensity in Fig.(4.10). The partially oxidized species are thus located close to the Si|oxide interface in line with findings from other groups [75].

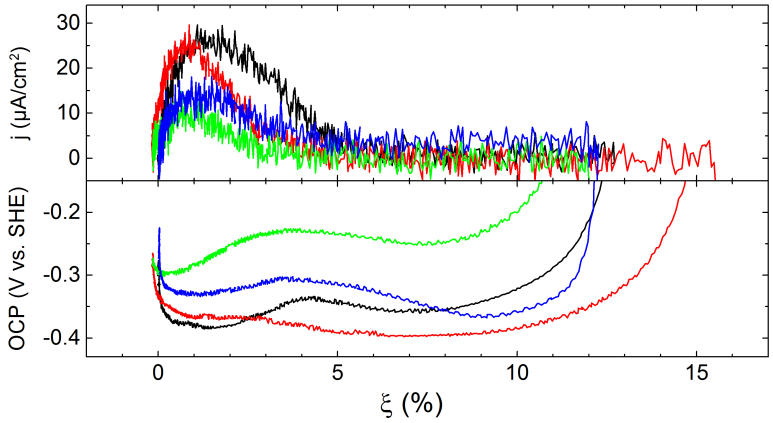

Figure 4.10: Etch-back curves for high amplitude current oscillations as shown in (Fig.3.8) c) with the color code indicating the turn-off phase according to Fig.(4.6); Top: Anodic current as a function of the ellipsometrice intensity during the etch-back at a potential of 50 mV vs. SHE**; Bottom: Open circuit potential as a function of the ellipsometric intensity during etch-backs at OCP.**

4.2.2 Partially oxidized species during the high amplitude current oscillations

To investigate the presence of the partially oxidized species in the silicon oxide layer during the oscillations we performed the etch-back experiments for more phases and integrated over the anodic current during the etch-backs. The resulting time dependent total measured charge

is shown together with the current in Fig.(4.11).

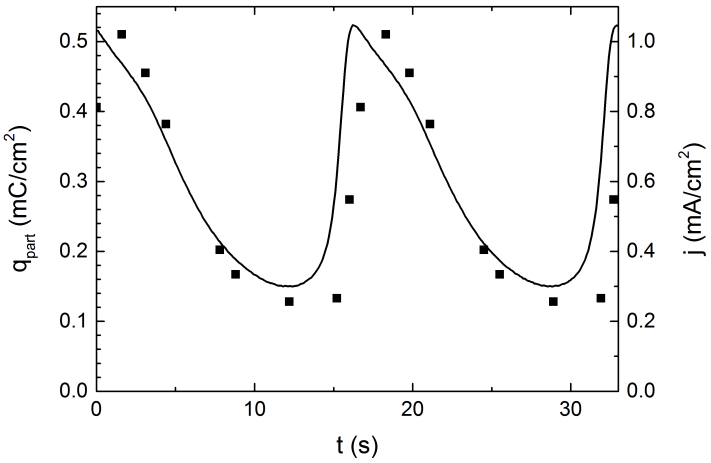

Figure 4.11: Charge density associated with the partially oxidized species as measured from the etch-back experiments as a function of time (dots, left scale) and the corresponding time series of the current (solid line, right scale). For a better visibility the charge data are stringed together for two oscillation periods.

The change in the presence of partially oxidized species is associated with a phase dependence of the reaction valency ν. In this view, the reaction valency can take values larger than $\nu = 4$ which can only be explained by the oxidation of previously partially oxidized species. In such processes a current flows but no additional oxide is produced. The partially oxidized species thus provide an additional pathway for the current which we write in the following form for the example of the partially oxidized species $Si(OH)_2$:

$$Si(OH)_2 + 2h^+ \rightarrow SiO_2 + 2H^+. \tag{4.1}$$

It is then also this oxidation current that is measured during the etch-back experiments. The question is then if the misfit between ellipsometric intensity and the current integral found for high amplitude oscillations (see Fig.(3.15)) can be explained by this phase dependence of the reaction valency. To answer it, Eq.(3.6) used for the fitting has to be reformulated. It then takes the following form:

$$c_{\mathrm{opt}}(\xi_{\mathrm{av}}) \cdot \xi(t) = c_{\mathrm{opt}}(\xi_{\mathrm{av}}) \cdot \xi_{\mathrm{av}} + \frac{M_{\mathrm{SiO_2}}}{F\nu_{\mathrm{av}}} \int_{t_0}^{t} j(\tau) - j_{\mathrm{av}} d\tau + (q_{\mathrm{part}}(t) - q_{\mathrm{part,av}}), \tag{4.2}$$

where ν_{av} is the average reaction valency and $q_{\mathrm{part,av}}$ the average amount of partially oxidized species present in the oxide layer. Using Eq.(4.2) and the measured charge data from Fig.(4.11) indeed an improvement of the fitting procedure can be seen as shown in Fig.(4.12). While the mismatch is reduced when the anodic etch-back currents are assumed to be caused by partially oxidized species, it is still not fully removed. The mismatch becomes even smaller under the assumption that during the etch-back the partially oxidized species are not only electrochemically oxidized via the pathway of Eq.(4.1) but also chemically oxidized during the etching process accompanied by hydrogen evolution as described in the last line of Eq.(2.15). This assumption is sensible as the overpotential for the electrochemical oxidation pathway, i.e. the difference between applied potential during the etch-back and the OCP, is relatively small. The electrochemical reaction thus proceeds relatively slowly and the purely chemical etching process can be significantly faster. Hydrogen evolution during etch-back experiments has been measured in our group but not yet investigated systematically. It seems, however, that there is no significant change in the total amount of partially oxidized species and that

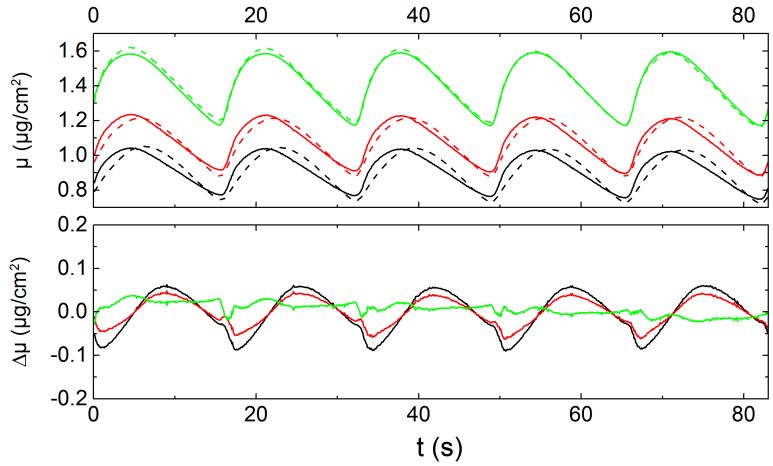

Figure 4.12: Top: Fitted silicon oxide mass density without $\nu(t)$-correction (black), with the $\nu(t)$-correction corresponding to the measured etch-back charge (red) and with a $\nu(t)$-correction corresponding to three times the measured etch-back charge (green) at $U = 8.65$ V vs. SHE, $c_F = 50$ mM and pH $= 2.3$. The solid lines indicate the left hand side of Eq.(4.2) and the dashed lines the right hand side. Bottom: Corresponding mismatches between the respective solid and dashed curves.

for the parameters chosen the chemical etching pathway accompanied by hydrogen evolution is of minor importance. Still, it is also interesting to try to improve the fitting by assuming that only a certain fraction of the partially oxidized species is detected. The best fit is then achieved by the assumption that only one third of the actual amount of partially oxidized species is electrochemically oxidized. The fit made under this assumption is also shown in Fig.(4.12) (green curves) and the corresponding mismatch is almost entirely gone. Note that all the correction to the fitting procedure also change the oxide mass per unit area significantly.

With the modified fitting procedure the reaction valency also becomes an oscillating quantity and takes the following form, assuming that changes in the hydrogen evolution can be neglected during the oscillations:

$$\nu(t) = \frac{\nu_{\mathrm{av}}}{1 + \dot{q}_{\mathrm{part}}(t)/j(t)}. \tag{4.3}$$

Under the assumptions that the etch-back current peaks are caused by partially oxidized species the reaction valency $\nu(t)$ then shows an intriguing behavior that might be very helpful in trying to identify a full model of the oscillations. This is best visualized by plotting the fitted oxide mass density against the reaction valency as is shown in Fig.(4.13) where a sharp jump in the reaction valency coincides with the minimal oxide mass density. The coincidence of the minimum of the mass density of the oxide layer and the jump in the reaction valency is remarkable as the former is associated with the state of the oxide layer while the latter is associated with its formation. This leads to the conclusion that the reaction valency or another quantity linked to the reaction valency is a good candidate for being an essential variable for the oscillation mechanism.

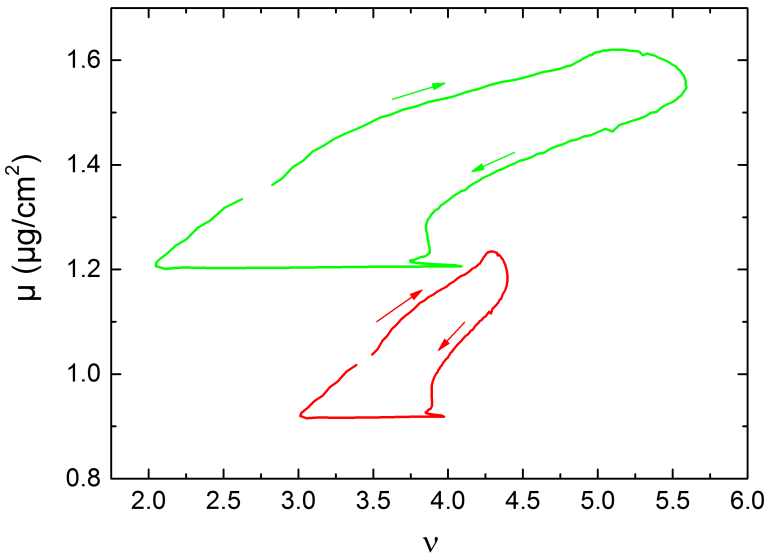

Figure 4.13: Phase space plot of oxide mass density $\mu(t)$ against the reaction valency $\nu(t)$ under the assumption that all partially oxidized species are electrochemically oxidized during the etch-back (red) and that only 1/3 of the partially oxidized species is electrochemically oxidized during the etch-back while the rest is chemically oxidized (green).

4.3 Discussion

Summing up the experimental findings from our group and others we conclude that there is a strong case for looking for a unified mechanism for, on the one hand, potentiostatic current oscillations with an external resistance and, on the other hand, both persistent and transient galvanostatic oscillations with and without etching. The experimental findings strongly suggest that the basis for the mechanism lies in either structural, chemical or electrical properties of the oxide layer itself. Neither the space charge layer of the silicon electrode nor variations of the etching electrolyte seem to play a central role for the positive feedback underlying the oscillations. While the latter seems to introduce at least higher order effects manipulating the properties of the oscillations, the former does not seem to have any effect at all. Instead, we found that the occurrence of partially oxidized species and following from this the time evolution of the reaction valency is a potentially good candidate for being an essential variable.

Concluding the chapter we want to focus on a more general aspect of modeling attempts in our group and in the literature. A dominant thread underlying many models presented in the literature is the idea that the oscillations are brought about by a synchronization phenomenon of local 'self-oscillating' microdomains. In light of our experimental findings we want to renounce this view and advocate for seeing the system as a homogeneous, oscillatory medium instead. In many publications the origin of the potentiostatic current oscillations is seen as the outcome of the synchronization of self-oscillating microdomains brought about by the presence of the external resistance [76, 77, 78, 71, 72, 73, 68]. This would correspond to a Kuramoto-transition with the external resistance as a control parameter [17]. The microscopic origin of the oscillations in the microdomains is then, if at all, treated in a second step. It is noteworthy that in many cases this second step is omitted which means that the proposed models are then not models at all [76, 77, 71, 72, 68] as it is a trivial result that the spatially averaged signal of a field of nearly identical oscillators oscillates with an amplitude depending on the degree of synchronization.

Originally the synchronization view arose from the interpretation of impedance spectra which were recorded for the system being in the state of a stable focus, i.e. the steady-state after transient damped oscillations [76, 77]. These spectra showed resonant behavior for some rational multiples of the transient oscillation period indicating that even in this non-oscillatory state the system was still exhibiting some feature of the oscillations. The reasoning was then that the frequencies were still active in the system but that the individual microdomains were desynchronized. There are a at least two difficulties with this interpretation, one concerning its plausibility and one concerning its internal consistency. First, note that for the impedance data to show resonances it is not necessary that the individual parts of the system are in their oscillatory state. The same behavior can be found for uniform media close to a supercritical Hopf bifurcation and can be attributed to the 'ghost' of the bifurcation [79] as was shown in our published work (Zensen et al.). Impedance measurements are thus not a helpful tool to distinguish between local oscillators and oscillatory media and the interpretation of impedance spectra recorded in stable foci necessarily requires the inclusion of nonlinear effects. Note furthermore that even if a system is indeed made from individual nonlinear oscillators a sharp 'quorum sensing' transition can occur where all oscillators become unstable simultaneously in identical bifurcations as was shown for ensembles of yeast cells and coupled Belousov-Zhabotinsky reactions [80, 81, 82]. Thus, even such systems composed of individual oscillators are then best treated as oscillatory media. Second, the size of the assumed microdomains (10^{-10} cm^2 [77]) is such that they should be diffusively coupled over the electrolyte or show some coupling via electrical quantities such as electric fields. In this case, however, the tendency of neighboring domains to desynchronize would be strongly suppressed and larger domains with synchronized behavior, reminiscent of Weiss domains in ferromagnets, should be expected at least for supposedly only partially synchronized states such as persistent low amplitude oscillations. For such a synchronization transition the spatially resolved data should thus show some spatial variations as a broad spectrum of phases is still active for the oscillators in the desynchronized state. This should then lead to a rather noisy signal in space. However, gradients in physical quantities cannot be seen in experiments with uniform oscillations down to a length scale of ca. 10 µm. In contrast, a perfectly synchronous oscillation of all points at the electrode surface is found for all oscillations measured on p-type silicon or highly illuminated n-type silicon, similar to the example shown in Fig.(3.4). This is true independent of the amplitude of the oscillations and in particular also when the system relaxes to a stable focus and thus, in the view of the synchronization model, for all degrees of synchronization. The synchronization view could then only be true if there was no local coupling whatsoever, a rather peculiar assumption given that changes in electrical quantities such as local potential variations are assumed to be present and that a diffusive coupling in the electrolyte is highly probable. This necessary assumption can also be disproved by our experiments as the comparison of one-dimensional cuts through the oxide thickness distribution across the silicon surface between measurements in a stirred and an unstirred electrolyte shown in Fig.(4.14) makes clear. In all four measurements in Fig.(4.14) the oscillations are almost perfectly uniform for the spatial resolution measured (ca. 10 µm). Keep in mind that the low amplitude current oscillations are supposed to be mostly desynchronized in the local oscillation view. The stirring does have a small effect on the spatial synchrony of the oscillation, as the fast phase wave present in the unstirred measurements is removed. This dependence of the occurrence of the phase wave on the stirring clearly indicates the presence of a non-local coupling, i.e. a coupling with a finite spatial range, mediated by the electrolyte. Under this coupling any synchronization phenomenon of local oscillators should form spatial aggregates which would then in turn be visible for the low amplitude current oscillations, i.e. the supposedly only partially synchronized oscillations. Such a behavior was never found in the hundreds of experiments we performed on p-doped and highly illuminated n-doped silicon

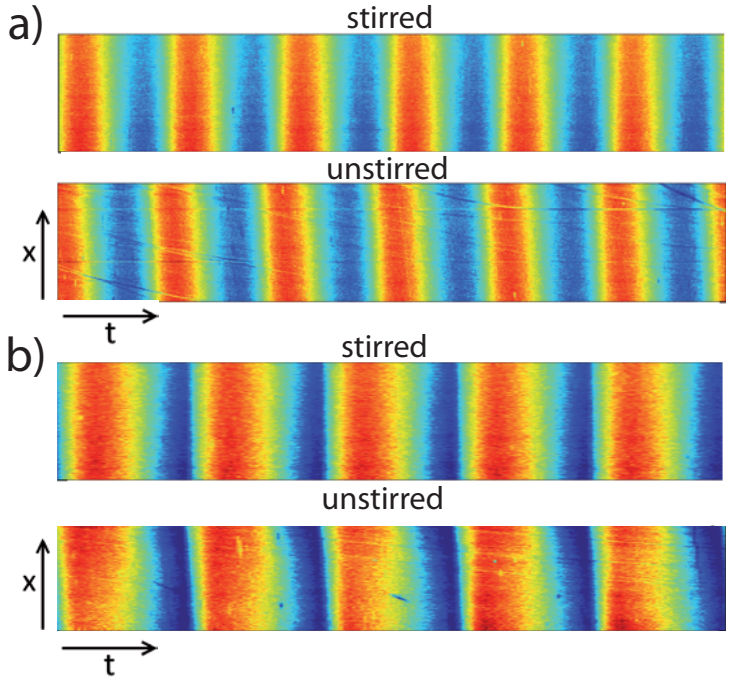

Figure 4.14: Comparison between the temporal evolutions of one-dimensional cuts through the ellipsometric intensity distribution across the electrode in stirred and unstirred electrolytes for a) low amplitude current oscillations at $R_{\mathrm{ext}}A = 2.7$ kΩcm^2 and b) high amplitude current oscillations at $R_{\mathrm{ext}}A = 13.5$ kΩcm^2 at the same conditions ($U = 8.65$ V vs. SHE, $c_{\mathrm{F}} = 50$ mM, pH $= 3$). Red indicates a relatively high and blue a relatively low ellipsometric intensity. The time axis of the four measurements are not to scale.

samples, and we thus feel quite confident in concluding that the idea of local oscillators is not valid. Instead, in our view the oxide layer at the interface constitutes an oscillatory medium, which ceases to oscillate when the parameters are varied and the system undergoes a Hopf bifurcation (see Fig.(3.5) and [63]). For uniform oscillations the problem of the oscillation mechanism is thus one dimensional. In this view the external resistance is then an integral part of the oscillation mechanism for the potentiostatic current oscillations as well as a global coupling term and not simply the latter. A windfall profit of this view is that the oscillations are measured directly and not as a composite signal of the base oscillation on the one hand and the degree of synchronization on the other hand.

We conclude the chapter by remarking that, while the system is a uniformly oscillating medium for p-doped and highly illuminated n-doped samples this does not mean that it is uniform on every conceivable length scale. Evidently at some level inhomogeneities as, e.g. nanoscopic pores, may occur. In this case a uniform density of these inhomogeneities on a more coarse grained level is indispensable. Furthermore, dynamical patterns on a relatively large scale can form for lowly illuminated n-doped silicon samples and possibly also for galvanostatic measurements. These patterns, however, have nothing to do with the local oscillator model but are self-organized and arise from dynamical instabilities in the oscillatory medium as will be discussed in detail in the following chapters.

5 Linear and nonlinear coupling

In this chapter we investigate the effect of a nonlinear current cut-off on the anodic silicon electrodissolution system. The cut-off can be introduced naturally by a restricted illumination for n-doped samples, as the oxidation current always involves valence band processes requiring photo-induced holes. This is the expected behavior for an n-doped semiconductor electrode as its contact with the electrolyte constitutes a Schottky-diode as discussed in Sec.(2.1.2). It might seem like a peculiar choice to investigate these specific conditions. The reason for our interest in this topic lies, as probably often in scientific research, in a serendipitous discovery made prior to this work in our group while studying the oscillatory silicon electrodissolution. In one case an n-doped sample was erroneously used instead of a p-doped one resulting in no measurable current. A current did, however, occur when the light proof box where the experiment is situated was opened and, much more interestingly, the ellipsometric intensity showed spatio-temporal pattern formation. We have investigated this phenomenon extensively since then. In this chapter we want to focus on the properties of the introduced current cut-off and interpret them in the context of the results presented thus far. The results on the properties of the patterns themselves will then be the subject of the next chapter.

Much like the external resistance the sharp current cut-off has two effects. First, it introduces a coupling between the points at the electrode surface by restricting a spatially averaged quantity and, second, it also possibly changes the behavior of the oscillating medium itself. A lower illumination intensity leads to a higher coupling strength. The coupling obviously has a nonlinear characteristics and is at least partly global as the total current, i.e. the current averaged over all points on the surface, is determining its strength.

To investigate the detailed properties and range of the illumination-induced current cut-off coupling we compare it to a global current cut-off coupling introduced by the current limiter already described in the last chapter in Sec.(4.1.1). In this way insights in, e.g., the time evolution of the surface energetics in illumination-limited measurements or the range of this coupling can be gained.

The current limiter was built by Andreas Heinrich as a part of his Master thesis and some measurements were performed by Andreas Heinrich and Carla Zensen as parts of their Master theses and Elmar Mitterreiter in the course of his Bachelor thesis [41, 42, 83]. The supervision of these works was part of this thesis.

5.1 Overview

In this part a short overview over the dynamical properties of the electrodissolution of silicon under current limitation is given.

5.1.1 Quantum efficiency

As a first step we take a closer look at the sharpness of the current cut-off. It is well established that for weakly illuminated n-doped silicon samples the current can be significantly higher

than the illumination restriction seemingly allows [50, 84, 48, 62]. This current multiplication effect is explained by electron injection processes from partially oxidized silicon oxide species to the conduction band. It is robust against variations of the electrolyte composition and the photon energy of the incident light [62]. The multiplication effect becomes stronger with decreasing illumination approaching a maximum multiplication factor of 4 corresponding to an injection of all but the first charge carrier in the tetravalent oxidation. The question is then whether the current cut-off is also subject to this effect in our measurements. This is relevant as the charge injection into the conduction band is a behavior genuine to n-doped silicon samples and has to be kept in mind when the oscillation mechanisms for illumination restricted n-doped samples and current limited p-doped samples are compared. In Fig.(5.1) the internal quantum efficiency Φ as defined in Eq.(2.20) at the cut-off plateau is shown for various measurements with the three standard electrolytes as a function of the illumination intensity I_{ill}.

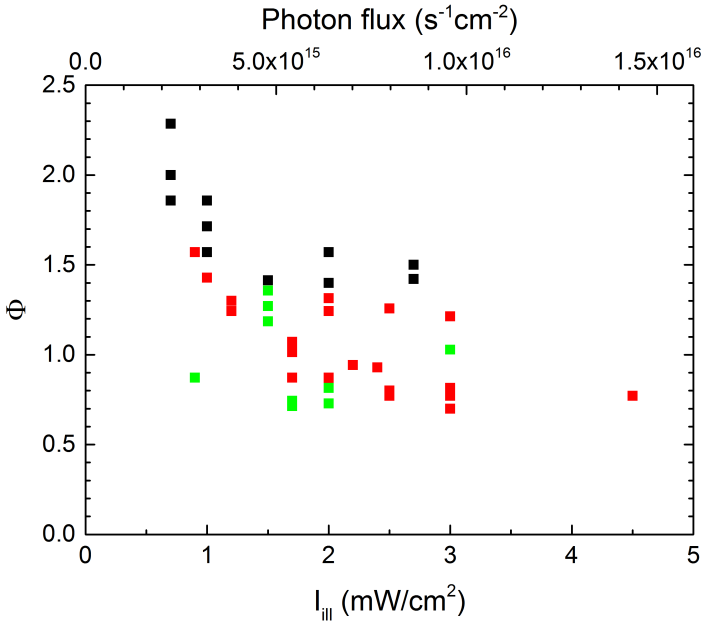

Figure 5.1: Internal quantum efficiency Φ at the current cut-off plateau as a function of the illumination intensity I_{ill} for measurements with $c_{\mathrm{F}} = 50$ mM at pH $= 2.3$ (black), $c_{\mathrm{F}} = 75$ mM at pH $= 1$ (red) and $c_{\mathrm{F}} = 75$ mM at pH $= 3.5$ (green).

The current multiplication effect is well visible below illumination intensities of ca. $I_{\mathrm{ill}} \approx 2$ mW/cm^2 albeit not for all measurements. The overall trend is in line with the one found in the literature although the literature data typically start at lower illumination intensities. We conclude that charge injections into the conduction band may play a role for n-doped silicon samples under restricted illumination but that it is nevertheless still sensible to compare illumination-restricted n-doped samples with current-limited p-doped samples and treat the possibility of electron injections to the conduction band as a source of deviating behavior.

5.1.2 Cyclic voltammogram

The cyclic voltammogram changes significantly when the illumination limitation is introduced [59, 40]. Examples for such CV scans are shown in Fig.(5.2), together with the corresponding development in the spatially averaged ellipsometric intensity. Comparing the illumination limited cyclic scans to the unlimited case, one notes that when the current reaches the illumination limit the oxide growth is initially suppressed. Only at significantly higher potentials

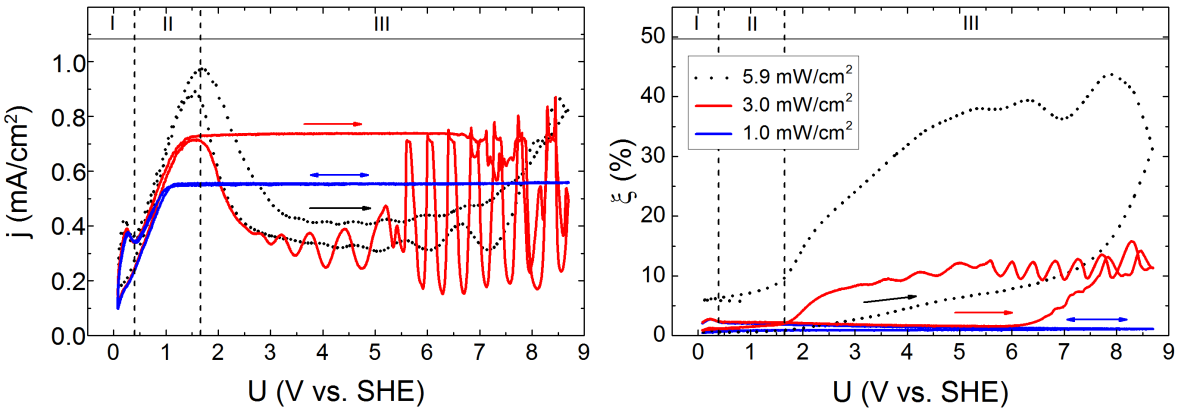

Figure 5.2: Cyclic voltammogram (left) (20 mV/s) of an n-Si sample (c_F = 75 mM, pH = 1, $\varrho >$ 40 Ωcm^2) at the levels of illumination indicated and the corresponding, spatially averaged ellipsometric signal ξ (right). The highly illuminated case (dot) is identical to a CV at p-doped silicon (see Fig.(3.1)).

does an oxide layer form. This can be understood by the additional high resistance introduced by the space charge layer of the n-doped silicon electrode under anodic bias. The potential shift for the oxide formation is illumination-dependent and at too low illumination levels no oxide formation is found at all. In the cases where a stable oxide layer forms both current and oxide layer mass show oscillations at relatively high potentials which increase in amplitude upon the change in the potential sweep direction. This behavior is similar to that of p-doped or highly illuminated n-doped silicon samples as evident by the dotted curves in Fig.(5.2). The illumination limited measurement at an intermediate illumination intensity (red curve) shows nicely that the illumination limitation has no further effect once only currents below the limit are present. This is visible on the back scan, where the current drops because of the formed oxide and stays consistently below the illumination induced limit. The curve then gradually moves towards and finally realigns with the unlimited curve.

In Fig.(5.3) a selection of cyclic voltammograms recorded with a p-doped silicon sample under various levels of current restrictions imposed by the current limiter are shown.

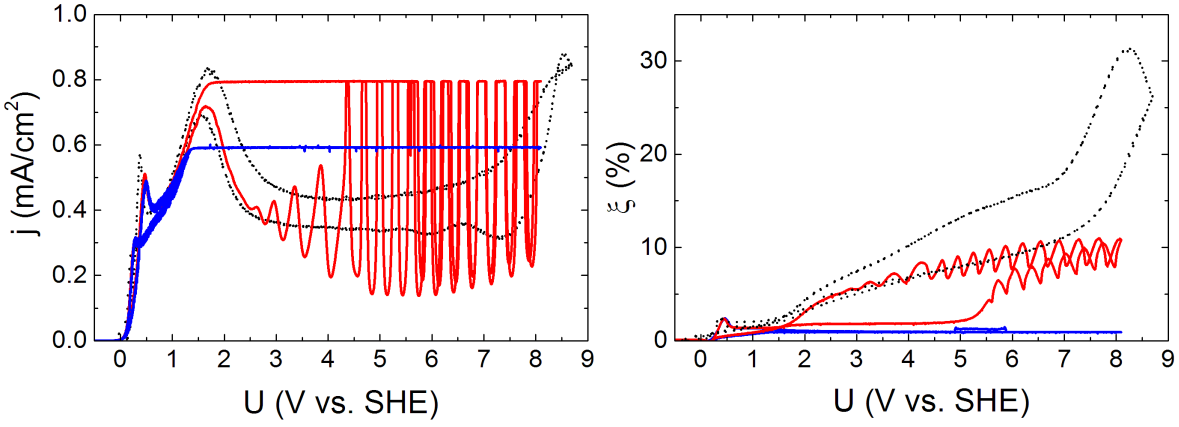

Figure 5.3: Cyclic voltammogram (left) (20 mV/s) of an p-Si sample (c_F = 50 mM, pH = 2.3) at two levels of current limitation j_{lim} = 0.79 mW/cm^2 (solid red) and j_{lim} = 0.59 mW/cm^2 (solid blue) and the corresponding, spatially averaged ellipsometric signal ξ (right). The unlimited case is also shown (dot).

Comparing Figs.(5.2) and (5.3) it becomes apparent that the four limited scans (red and blue

curves in the respective pictures) share some key features. If the limitation is not too strong, the oxidation onset is significantly shifted to higher applied potentials compared to the unlimited case and the oxide formation is immediately accompanied by oscillations. In case of the strongly restricted measurements the oxide does not form at all, which can in both cases be explained by a strong potential drop across the respective limiters, i.e. the space charge layer in the silicon electrode in the former and the current limiter in the latter case. The rest of the applied potential is then too small to lead to oxide formation corresponding to regions I and II in the unlimited CV. Differences in the shape of the curves arise for two reasons. First, the fact that different electrolytes were used changes the absolute values of the relevant current cut-off levels and the overall scaling as well as the shape of the ellipsometric intensity scans in the unrestricted case. Second and more importantly, pattern formation along a growing front is seen for the illumination-restricted measurement where the oxide layer is formed, while this cannot be seen in the presence of the current limiter. This points to a local component of the illumination-induced coupling, at least in the transient phase where the oxide is first formed. This point will be further investigated in Sec.(5.3.1) below. Note that the cut-off of the total current still strongly suggest the presence of a global component in the coupling range.

5.1.3 Current oscillations

The illumination limitation induced coupling is in itself sufficient to generate sustained oscillations as shown in the phase space plots in Fig(5.4) where measurements in which no external resistance was used are displayed.

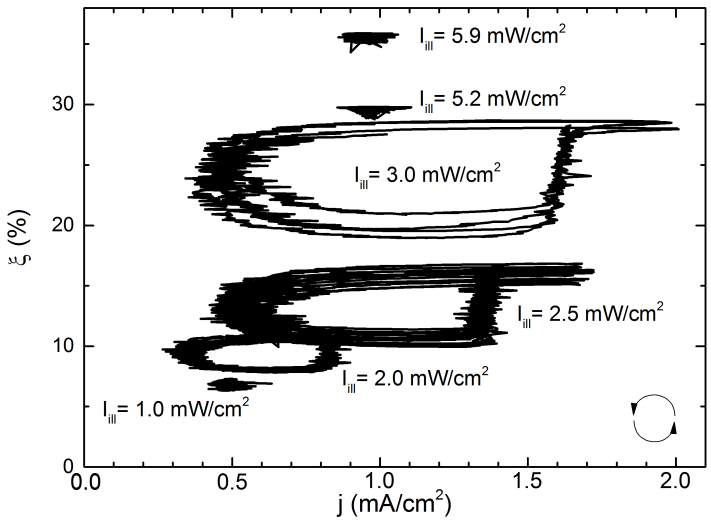

Figure 5.4: Phase space plots of spatially averaged time series occurring during the photoelectrodissolution of n-doped silicon at various levels of the illumination intensity I_{ill} ($U = 8.65$ V vs. SHE, $c_{\mathrm{F}} = 75$ mM, pH $= 1$) without an external resistance, i.e. at $R_{\mathrm{ext}}A = 0$ kΩcm^2. The arrows in the lower right hand corner indicate the direction of rotation for all curves.

Again the coupling strength is also a bifurcation parameter leading to stable foci above an electrolyte specific, critical illumination intensity and stable oscillations below it. At very high coupling strength, i.e. at low illumination intensities, the system relaxes to a stable node. In contrast to the case of the linear global coupling discussed above, however, the transition to the steady state is not abrupt and thus not of the same origin. It is linked to pattern formation and can thus only be understood considering the spatially extended system. This point will be discussed in more detail in the following chapter. The measurements show that not in all cases an external resistance is required for sustained oscillations and rather, can also

be brought about by other methods of coupling. The current cut-off coupling does, however, share a key characteristics with the external resistance in that it is a synchronizing coupling for the voltage drop across the interface and this can in turn be seen as an important property for the existence of sustained oscillations [85]. Note that this does not mean that pattern formation is suppressed under this coupling but that the pronounced pattern formation found in experiments dominated by this coupling rather points to an inhibitory role of the essential, potential related variable in the oscillation mechanism [86].

A prototypical example for the time series of an illumination-restricted measurement is shown in Fig.(5.5). Note that the notation $\overline{\xi}$ will be used for the spatially averaged ellipsometric intensity from this point on to underscore the fact that pattern formation is expected.

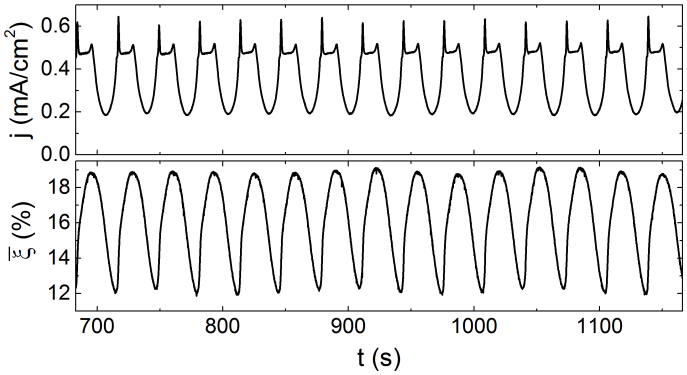

Figure 5.5: Prototypical time series of current j and spatially averaged ellipsometric intensity $\overline{\xi}$ during the photo-electrodissolution of n-doped silicon (8.65 V vs. SHE, $c_{\mathrm{F}} = 75$ mM, pH $= 3.5$, $R_{\mathrm{ext}}A = 5.9$ kΩcm^2, $I_{\mathrm{ill}} = 1.7$ mW/cm^2)**. Current overshoots at the beginning and the end of the current limited plateau are well visible.**

The current plateau well visible is not an entirely sharp cut-off but is typically accompanied by overshoots at the beginning or the end of the plateau or both, the latter being realized in Fig.(5.5). We denote these overshoots l-peak and r-peak for the one at the beginning, i.e. the left hand side, and the one at the end, i.e. right hand side, of the plateau, respectively. The occurrence of the r-peak is strongly correlated with pattern formation while an l-peak seems to have a synchronizing effect which leads to less pronounced pattern formation.

5.2 Spatially averaged properties

In this part we neglect the role of pattern formation and concentrate on the spatially averaged quantities j and $\overline{\xi}$ to investigate the properties of current limited oscillations.

5.2.1 Voltage drops during the oscillations

In general, the shape of the oscillations in current and spatially averaged ellipsometric intensity is very similar under current cut-off coupling irrespective of the origin of this coupling when the current cut-off happens at the same level and all other parameters are identical. This offers a very interesting possibility to measure electrical quantities during the illumination restricted measurements that would be otherwise inaccessible. From Fig.(2.3) we can read out the following expression:

$$U_{\mathrm{el}} - E_{\mathrm{Si}}^{\mathrm{eq}} = \eta_{\mathrm{sc}} + \eta_{\mathrm{reac}} + \eta_{\mathrm{ox}}. \tag{5.1}$$

Since the equilibrium electrode potential $E_{\mathrm{Si}}^{\mathrm{eq}}$ is a constant and η_{sc} was shown to be of negligible effect so far (see Sec.(4.1.2)), changes in the measurable voltage drop across the electrode U_{el}

were identical to changes in $(\eta_{\mathrm{reac}} + \eta_{\mathrm{ox}})$ which was thereby shown to be essential for the oscillatory dynamics. In contrast in the illumination limited case, the strong changes of η_{sc} due to the illumination limitation then destroy this connection and the essential variable $(\eta_{\mathrm{reac}} + \eta_{\mathrm{ox}})$ can no longer be measured directly. The measured voltage drop across the electrode is thus no longer the essential variable for oscillations with an illumination restricted current. In contrast, the measured potential drop across the electrode U_{el} is an essential variable for the oscillations with current limiter since the potential drop across this limiter occurs outside of the electrode and can be measured separately while η_{sc} is again negligible. Whenever the oscillation shapes are similar under both types of current restriction, the time series of the potential drop across the electrode for the limiter measurements thus offers a reasonable measure for the time series of $(\eta_{\mathrm{reac}} + \eta_{\mathrm{ox}})$, i.e. the essential potential related variable, under illumination restriction. In Fig.(5.6) an example for such a comparison between illumination restricted and current limiter restricted current oscillations is shown together with a measurement under both restrictions.

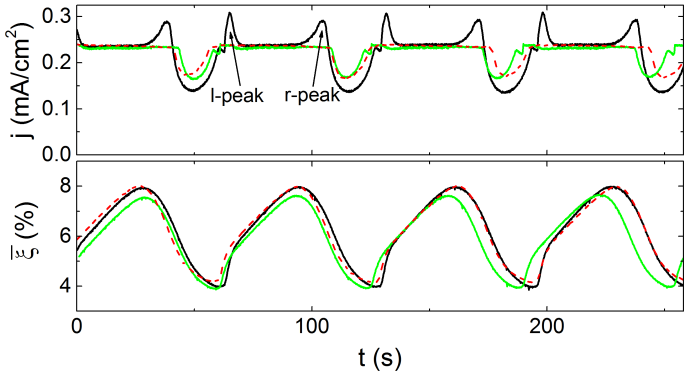

Figure 5.6: Time series of current j and spatially averaged ellipsometric intensity $\overline{\xi}$ for an illumination restricted measurement at $I_{\mathrm{ill}} = 0.7$ mW/cm^2 (black), a current limiter restricted measurement at $j_{\mathrm{lim}} = 0.24$ mA/cm^2 and $I_{\mathrm{ill}} = 5.9$ mW/cm^2 (red dash) and a measurement under both restrictions at $j_{\mathrm{lim}} = 0.24$ mA/cm^2 and $I_{\mathrm{ill}} = 0.7$ mW/cm^2 (green) ($U = 9.15$ V vs. SHE, $c_{\mathrm{F}} = 50$ mM, pH $= 1$, $R_{\mathrm{ext}}A = 0.51$ kΩcm^2).

It is clear from the graph that apart from the occurrence of the l- and r-peaks in the curve recorded under illumination restriction only, the measurements are very similar. Only the curve under both restrictions shows a significant increase in the frequency as well as a decrease in the amplitude of the ellipsometric intensity. The similarity of the curves is then making us confident to be able to get a good estimate of the time evolution of the potential drop across the space charge layer in the silicon $\eta_{\mathrm{sc}}(t)$. In Fig.(5.7) the time evolutions of current and voltage drop across the electrode for the three measurements from Fig.(5.6) are shown. A comparison between the voltage drop across the electrode of the three curves is not possible over the entire time series as the doubly restricted curve has a higher frequency. All three curves do, however, fit rather nicely during the second oscillation shown, starting at ca. 50s. It is this oscillation we will hence focus on. We will first neglect the l- and r-peaks in a 'zeroth order' view and incorporate their effect later. We thus first take a look at the red dashed curve in Fig.(5.7). Apart from the artifact that the voltage drop across the electrode has a lower cut-off, the shape of this curve is similar to typical high amplitude current oscillations and its phase space picture is similar to the two partly restricted cases in Fig.(4.2) (red and green curves). In zeroth order the illumination limited oscillations thus seem to be again typical high amplitude current oscillations. The effect of the l- and r-peak alone can then be seen in a 'first order approximation' by comparing the zeroth order curve (red dash) with the doubly restricted curve (green). In the latter the l- and r-peaks are clearly visible as voltage

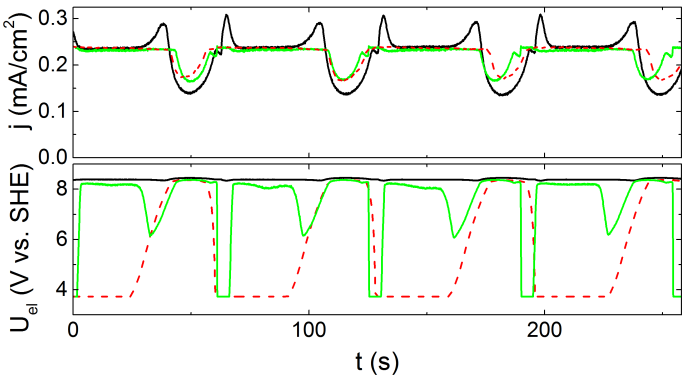

Figure 5.7: Time series of current j and voltage drop across the electrode U_{el} for an illumination restricted measurement at $I_{\mathrm{ill}} = 0.7$ mW/cm^2 (black), a current limiter restricted measurement at $j_{\mathrm{lim}} = 0.24$ mA/cm^2 and $I_{\mathrm{ill}} = 5.9$ mW/cm^2 (red dash) and a measurement under both restrictions at $j_{\mathrm{lim}} = 0.24$ mA/cm^2 and $I_{\mathrm{ill}} = 0.7$ mW/cm^2 (green) ($U = 9.15$ V vs. SHE, $c_{\mathrm{F}} = 50$ mM, pH $= 1$, $R_{\mathrm{ext}}A = 0.51$ kΩcm^2).

dips and it becomes clear from this comparison that the two peaks are not contributing any surprising new features to the time series of the voltage drop across the interface. We thus interpret the l- and r-peaks as overshoots, i.e. they can be seen as an imperfection of the illumination-induced limitation possibly brought about by the possibility of charge injections into the conduction band as discussed in Sec.(5.1.1). This also means that the term $(\eta_{\mathrm{reac}}+\eta_{\mathrm{ox}})$ is treated as more or less identical for measurements under restricted illumination and the high amplitude current oscillations and that these oscillations again share the same basic oscillatory mechanism. It is interesting to note, however, that the r-peak seems to always occur close to the maximum in the spatially averaged ellipsometric intensity $\overline{\xi}$ while being at the same time, as already mentioned, linked to pattern formation.

5.2.2 Etch-back characterization

We performed an etch-back characterization for a current limited measurement in a very similar way to the one presented in Sec.(4.2). The overall result is strikingly similar with one important difference. In Fig.(5.8) the time evolution of the measured charge is shown together with the time series of the current. Overall this picture looks very similar to Fig.(4.11), i.e. the corresponding one for the unlimited case. There is just the hint at a small difference in that the measured charge is comparatively large on the current plateau. When comparing the fit made under the assumption of the presence of partial oxides according to Eq.(4.2), again a very similar behavior to the unrestricted case is found. As was the case then, the best fit is achieved under the assumption that only 1/3 of the charges is electrochemically oxidized while the rest is etched away in a purely chemical fashion accompanied by hydrogen evolution. The three corresponding fitting curves are shown in Fig.(5.9). Again a peculiarity differentiating between the unrestricted measurements shown in Fig.(4.12) and the current restricted ones shown in Fig.(5.9) arises at the beginning of the current plateau, i.e. at the ascending slope of the oxide mass curves. Here the measured amount of charge is higher than expected leading to an overcompensation of the mismatch there. This points towards another origin of parts of the etch-back charges there, possibly a real charging effect in form of trapped charges. We have not investigated this phenomenon in detail so far, but found that it becomes more pronounced for a stronger current restriction, i.e. lower values of j_{lim}.

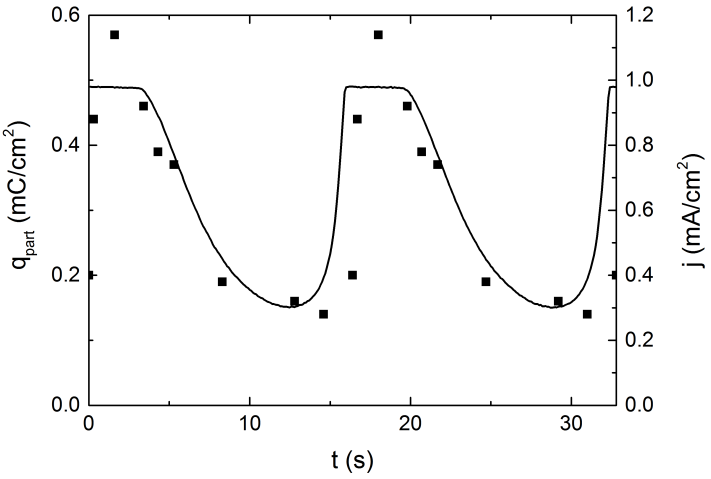

Figure 5.8: Charge density associated with the partially oxidized species as measured from the etch-back experiments at a p-doped sample under current limitation as a function of time (dots, left scale) and the corresponding time series of the current (solid line, right scale). For a better visibility the charge data are stringed together for two oscillation periods (U = 9.15 V vs. SHE, c_F = 50 mM, pH = 2.3, $R_{ext}A$ = 6.2 kΩcm^2, j_{lim} = 0.81 mA/cm^2).

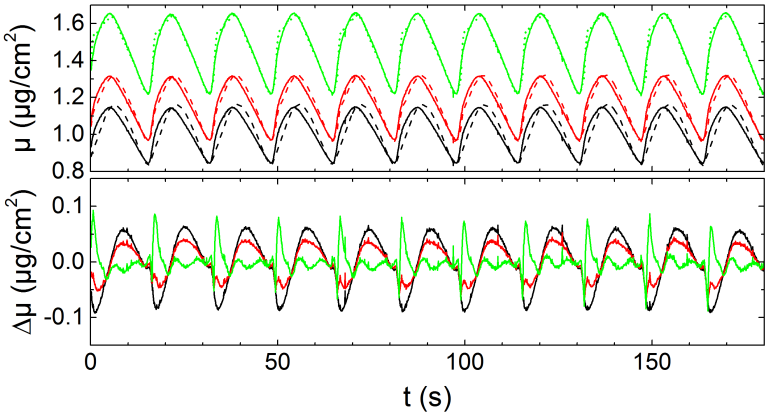

Figure 5.9: Top: Fitted silicon oxide mass density without $\nu(t)$-correction (black), with the $\nu(t)$-correction corresponding to the measured etch-back charge (red) and with a $\nu(t)$-correction corresponding to three times the measured etch-back charge (green). The solid lines indicate the left hand side of Eq.(4.2) and the dashed lines the right hand side. Bottom: Corresponding mismatches between the respective solid and dashed curves.

5.2.3 Bistability

As was the case for oscillations without a current limitation (see Sec.(3.2.3)), a bistability can also be found for current restricted oscillations. Also similar is the fact that the two states are distinguished by a different temporal average of the spatially averaged ellipsometric intensity $\overline{\xi}$ and thus probably different oxide layer thicknesses. In Fig.(5.10) an example showing this bistability is presented. In the present case the second state (new state) which is present after the intermediate state is of a different nature than those discussed before as it is clearly periodic and not chaotic. Still it shows a much more complex temporal dynamic than the state before the intermediate state (old state). We conclude that it would be in any case revealing to broadly scan the system for further multistability by initializing it with different oxide layers which can be best characterized by the measured ellipsometric intensity. The

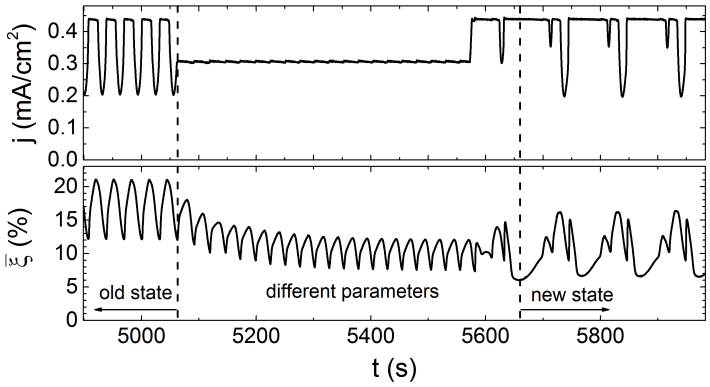

Figure 5.10: Time series of the current j (top) and spatially averaged ellipsometric intensity $\bar{\xi}$ (bottom) of a high amplitude potential oscillation before an intermediate parameter change (old state until ca. 5150 s) and a three peak oscillation after the intermediate parameter change (new state starting at ca. 5670 s) at a highly illuminated n-doped electrode (U = 9.15 V vs. SHE, c_F = 50 mM, pH = 1, $R_{ext}A$ = 5.1 kΩcm², I_{ill} = 5.9 mW/cm², j_{lim} = 0.44 mA/cm² old and new state, j_{lim} = 0.31 mA/cm² intermediate state).

oscillation types thus encountered then offer a good test for any model which is proposed for the spatially uniform oscillatory electrodissolution of silicon.

5.3 Pattern formation

If both coupling mechanisms, the linear global coupling brought about by the external resistance and the nonlinear current cut-off coupling, are combined, pattern formation is found as long as the linear global coupling is not too strong compared to the nonlinear coupling. This leads to a typical parameter space as shown in Fig.(5.11).

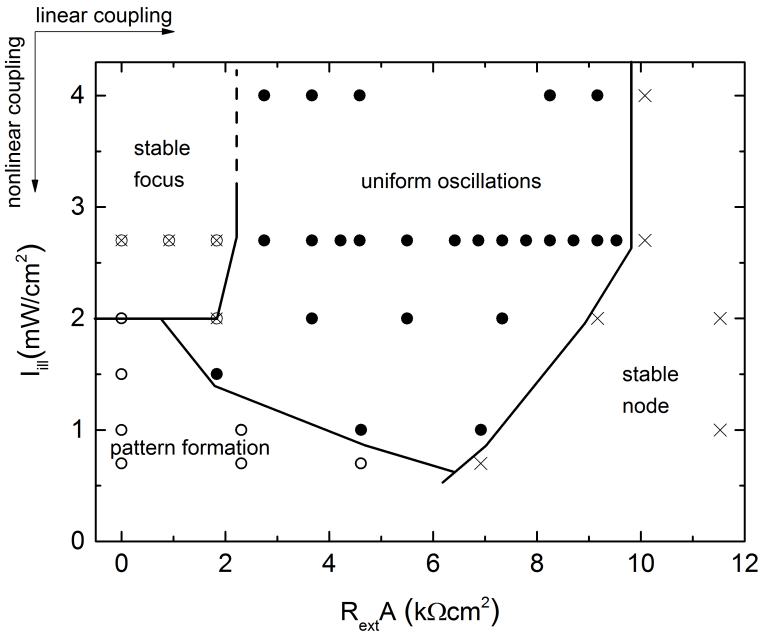

Figure 5.11: Dependence of the oscillation type on the strengths of the linear, global coupling $R_{ext}A$ and the nonlinear coupling, the restriction of I_{ill} (U = 8.65 V vs. SHE, c_F = 50 mM, pH = 2.3).

The overall qualitative behavior is in line with the one found for the 1d parameter space of p-doped samples. Again, too low overall restrictions on the oscillator (upper left hand corner) lead to a stable focus and too strong ones result in no oxide formation at all (lower right hand side). The line separating the pattern forming from the uniform regime is in line with the fact that the external resistance acts as a synchronizing linear global coupling. Note once again that synchronization in this context does not have anything to do with possible micro-oscillators but rather with a shift in the parameter value at which the uniform oscillation become destabilized leading to pattern formation.

5.3.1 Coupling range

Good candidates for the origin of a non-local component in the coupling are the finite lifetime of the photo-generated minority charge carriers which is paired with a finite spatial range of their movement, on the one hand, and the finite spatial extension of space charge layers forming during the current-limited oscillations, on the other hand. These candidates can be experimentally evaluated by comparing measurements with highly doped samples, in our case ca. $n_D = 5 \cdot 10^{16}$ cm^{-3} or $\varrho = 0.1 - 0.5$ Ωcm, to those of samples with a low doping level, here $n_D \leq 10^{14}$ cm^{-3} or $\varrho > 40$ Ωcm. Both candidates are affected in the same way by the doping level showing shorter characteristic length scales for higher and longer characteristic length scales for lower doping levels. For example, for the former doping level the minority charge carrier lifetime is in the range of $\tau \approx 50$ µs while it is a factor of 10 higher for the latter, i.e. $\tau \approx 500$ µs [57]. To illustrate the experimental differences between these two doping types, the temporal evolution of 1d cuts recorded during cyclic voltammograms in identical electrolytes are shown for both doping types in Fig.(5.12).

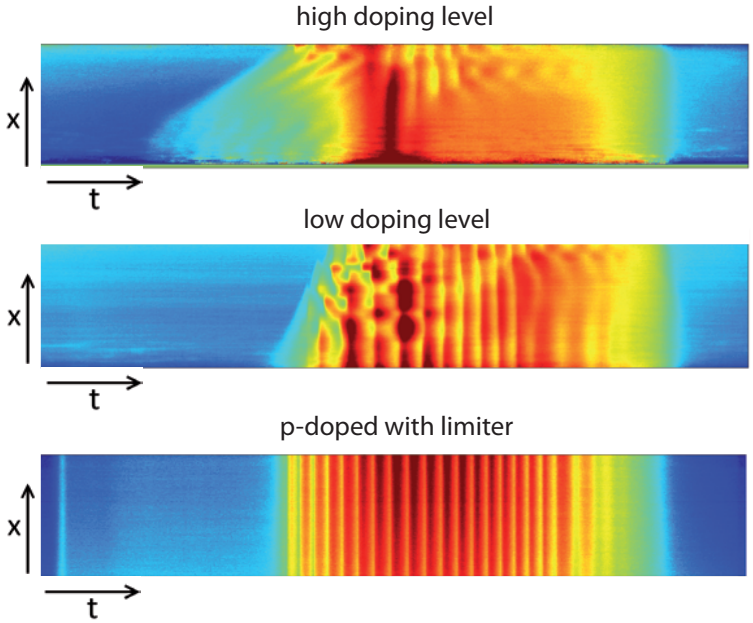

Figure 5.12: Comparison between the temporal evolutions of one-dimensional cuts through the ellipsometric intensity distribution across the electrode recorded during CV scans (20 mV/s, $c_F = 75$ mM, pH = 1, $I_{ill} = 2.0$ mW/cm^2) **for highly n-doped silicon** ($n_D \approx 5 \cdot 10^{16}$ cm^{-3}) **(top), lowly n-doped silicon** ($n_D \leq 10^{14}$ cm^{-3}) **(middle) and p-doped silicon with current limiter** (20 mV/s, $c_F = 50$ mM, pH = 2.3, $j_{lim} = 0.80$ mA/cm^2)**. Red indicates a relatively high and blue a relatively low ellipsometric intensity.**

Following the graphs in Fig.(5.12) from top to bottom it becomes apparent, that the onset of the oxidation is becoming less gradual, i.e. that the moving front becomes faster. This is no surprise for the p-doped silicon sample with current limiter, as the coupling is purely global in this case and no moving front is expected. The moving front is significantly faster for the lowly n-doped sample than for the highly n-doped sample. This means that the local component of the coupling has a longer range in the former and a shorter range in the latter case [87]. This finding is in line with the behavior of both the minority charge carrier lifetime and the spatial extension of the space charge layer as a function of the dopant concentration and the measurement thus corroborates the notion of these effects being responsible for the local component of the coupling. The hole configuration, for example, would in this view then have not enough time in the highly doped material to realign in a spatially uniform manner after a certain amount of holes was taken out of the system at a certain location driving local oxide formation. Instead, only the configuration close to the point where the holes were taken out would then feel the distortion, an effect whose range would then critically depend on the lifetime. A similar moving front growth of the oxide layer can be seen when transients preceding stable oscillations are regarded supporting the findings of the CV scans.

5.3.2 Origin of the patterns

Comparing the two one-dimensional cuts in the top part of Fig.(5.12) to the one in the bottom, one sees that the illumination limited n-doped samples show spatial patterns while the current limited one is spatially uniform. This is again similar to transients preceding oscillations where pattern formation is also typical for illumination restricted measurements even when the final oscillatory state might gradually become spatially uniform, while for current limited p-doped sample patterns are found neither in the transient nor during stable oscillations. This immediately raises the question whether the patterns are induced by these transients. We can address this question by initializing the system with a uniform oxide layer at certain parameters and then switching the parameters to different values in the pattern forming regime. Such a measurement is shown in Fig.(5.13). It is apparent from Fig.(5.13) that the patterns are indeed self-organized and not caused by inhomogeneities during the initial oxide growth. To what extent the range of the coupling plays a role has not been investigated systematically so far. We found, however, that a similar emergence of patterns is not seen in the purely globally coupled case of current-limited oscillations of p-doped samples. Here, patterns were only found in the absence of stirring, i.e. in the presence of another electrolyte-mediated spatial coupling. Thus, experimentally the patterns seem to require at least some measure of local component of the coupling. Keep in mind, however, that many features of the illumination-induced and current-limited coupling are identical and that thus the illumination-induced coupling can be approximated as a global coupling in many aspects.

5.3.3 Borders of the oscillatory regime

An interesting phenomenon is found at the border of the oscillating regime where the oxide layer becomes unstable not because of a too high external resistance as was discussed in Chap.(3) but because of a too low illumination intensity. In this case a part of the electrode is often found to be covered by an oxide layer while the rest remains uncovered. Much like for uniform oscillations where the voltage drop across the external resistance becomes too high to leave enough driving force for the oxide layer formation, also here the driving force becomes too small to sustain the moving front shown in the CVs in Fig.(5.12) until it covers the entire electrode. Such half-covered electrodes are found regularly at the border of the two parameter regimes with decreasing oxide layer coverages for decreasing illumination intensities and can exhibit quite unique behavior an example of which is shown in Fig.(5.14).

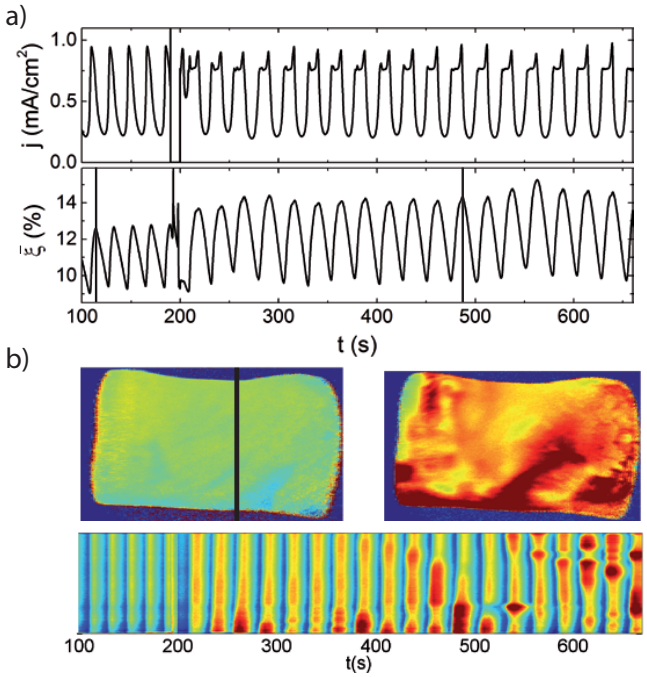

Figure 5.13: Pattern formation after spatially uniform initialization for $c_F = 50$ mM, pH $= 2.3$ and $R_{ext}A = 7.2$ kΩcm^2, $I_{ill} = 5.9$ mW/cm^2 before the parameter change at $t = 200$ s and $R_{ext}A = 0.36$ kΩcm^2, $I_{ill} = 2.2$ mW/cm^2 after the parameter change. a) Time series of j and the spatially averaged ellipsometric intensity $\bar{\xi}$; b) Ellipsometric intensity distribution on the electrode for the two times indicated by the vertical lines in a) and the temporal evolution of a 1d cut along the line indicated in the left electrode picture. Red indicates a relatively high and blue a relatively low ellipsometric intensity.

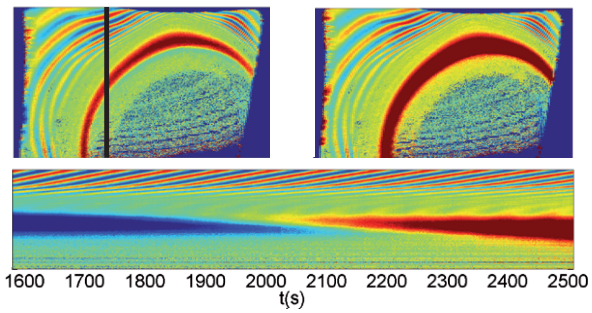

Figure 5.14: Ellipsometric intensity distribution on the electrode for two times (top) and the temporal evolution of a 1d cut along the line indicated in the left electrode picture (bottom) ($U = 8.65$ V vs. SHE, $c_F = 50$ mM, pH $= 1$, $R_{ext} = 10.4$ kΩcm^2, $I_{ill} = 0.25$ mW/cm^2). Red indicates a relatively high and blue a relatively low ellipsometric intensity.

The lower right hand part of the Fig.(5.14) is not covered by an oxide layer and shows no time variations. Conversely, in the left hand side and the upper part of the electrode phase waves are visible moving from the border between active and passive part outward to the borders of the electrode. At the separation between both parts, visible as the prominent red ring fragment, a long term variation with a high amplitude is found which is possibly an artifact of the data manipulation procedure described in Sec.(2.4). The gradual increase of the area of the inactive part with a decreasing illumination intensity is then a possible reason why the oscillation amplitude gradually decreases when approaching this border of the oscillatory regime in parameter space. When traveling waves as shown in Fig.(5.14) are present this gradual decrease becomes even more pronounced as these waves tend to become slower and slower thus averaging out the overall oscillation.

5.4 Summary and discussion

We have shown that the illumination induced coupling is itself sufficient for sustained oscillations and that under this coupling an external resistance is thus no longer indispensable. In spite of the current multiplication effect, which is clearly present for many measurements, many features of the illumination-induced current restriction can be reproduced using a current limiter. This comparison then serves two purposes: First, the voltage drop across the current limiter can be used to give a good estimate for the voltage drop occurring due to the kinetics of the electrochemical reaction and the oxide layer ($\eta_{\mathrm{reac}} + \eta_{\mathrm{ox}}$) which we assume to be an essential variable for the oscillatory mechanism. Accordingly, some features of the oscillations are quite similar to high amplitude current oscillations without restriction as shown by etch-back characterizations. Second, the similarities between illumination-restricted and current limiter-restricted measurements clearly show that a global component of the former plays a significant role for the dynamics since the latter is a purely global coupling.

The spatio-temporal patterns forming under illumination restriction but not under current limiter restriction seem to indicate that some local component in the coupling is indispensable for their occurrence. They are, however, not induced by inhomogeneities in the transient initialization phase, i.e. the initial growth phase of the oxide layer. Instead, they are dynamically stable states which occur even if the system is initialized in a perfectly uniform way. The details of the patterns forming will be the subject of the following chapter where we will also make the case that it is again the global component of the coupling that governs the overall behavior and not, as might be the conclusion here, local components.

6 Patterns

For the last three chapters we focused our attention mostly on uniform oscillatory dynamics. In this chapter the overall thread of the thesis as laid out in Fig.(1.1) is taken up and the states further away from equilibrium showing a more complex behavior are investigated. It is already remarkable that a system which is influenced by a time independent, spatially uniform driving only can exhibit an oscillatory steady-state and the silicon electrodissolution proved to be an interesting model system to study this phenomenon. However, the system shows even more levels of spontaneous structuring which are surprising when taking into account that all externally set parameters are uniform, both in time and space. Following the schematic bifurcation diagram in Fig.(1.1) the first new level of structuring is the occurrence of spatio-temporal patterns in the oxide layer thickness where before all oscillations were uniform. The patterns exclusively occur during the photo-electrodissolution of n-doped silicon under limited illumination and are visible as spatio-temporal variations in the ellipsometric intensity signal with a typical length scale for the spatial variation in the order of $10-100$ μm. There are several qualitatively different types of patterns forming on the surface, and for a large part of parameter space more than one of them introduce stable basins of attraction. This opens the way for an additional level of self-organized complex structuring that is quite surprising: the coexistence of qualitatively different dynamics on the electrode surface. The most famous example for this kind of pattern is called 'chimera state' and is defined by the coexistence of synchrony and chaos [88, 89]. As will be shown below, in our case such a coexistence of drastically different dynamics does occur in our system, and this with purely spatially and temporally uniform parameters. It is thus fully self-organized. Finally, long term variations, i.e. variations of the dynamical behavior on timescales much larger than the oscillation period are frequently found. While in the previous chapters mostly the question of why the oscillations occur was addressed, in this part a different point of view shall dominate the argumentation. Here, we take the oscillatory electrode as given and treat the patterns as additional features of the system, both in experiments and theory. In doing so, we thus concentrate on the branches further from equilibrium than the second bifurcation in Fig.(1.1) where the branch denoted 'uniform oscillations' can be seen as the starting point.

The occurrence of patterns during the anodic oxide growth were first observed in electroluminessence experiments on amorphous silicon samples [49, 90] and to our knowledge no further investigations into spatial pattern formation on a large length scale have been published. In our own group patterns during the photo-electrodissolution of n-doped silicon were then first reported and analyzed in detail [39, 40]. This chapter is devoted to a discussion of the central findings concerning these patterns.

The results presented here have been partly recorded by Martin Wiegand and Elmar Mitterreiter during their Bachelor theses which were supervised as a part of this work [91, 83]. The theoretical interpretations and results were obtained for the most part by Lennart Schmidt as part of his PhD work [92].

6.1 Overview

Compared to patterns classically found in oscillatory media the silicon oscillator exhibits two characteristic and peculiar phenomena: First, in a large part of the pattern forming parameter region the global quantities, i.e., the total current j and the spatially averaged ellipsometric intensity $\overline{\xi}$ oscillate in a simple periodic fashion although local time series exhibit complex oscillation forms up to completely irregular ones. Besides, j and $\overline{\xi}$ may oscillate with a period-2 or irregularly. Second, typically different dynamic behaviors as for example cluster patterns and spatio-temporal chaos coexist on the electrode. To make the discussion of these patterns easier understandable we introduce the term region for a part of the surface exhibiting one distinct dynamical state.

In the following the patterns are classified, in a first step, according to the spatially averaged ellipsometric intensity $\overline{\xi}$ into three categories:

- Simple periodic oscillations
- Period-2 oscillations
- Oscillations with an irregular amplitude

Prototypical examples for time series of the three types of $\overline{\xi}$-oscillations are shown in Fig.(6.1).

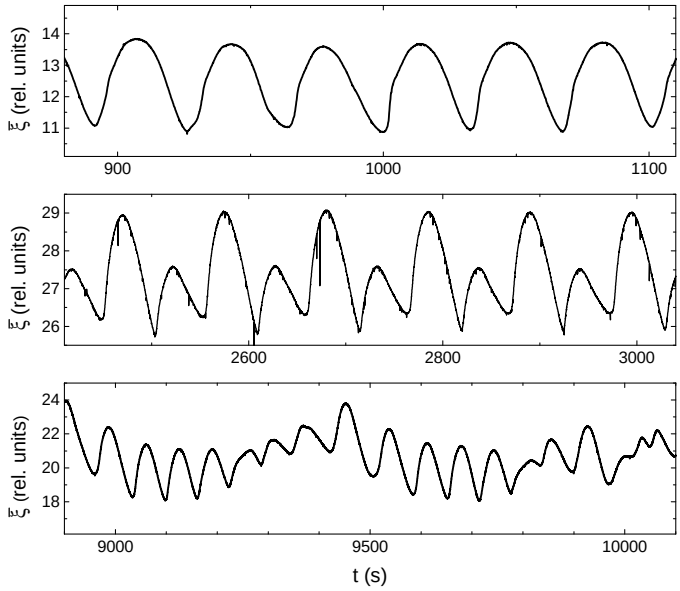

Figure 6.1: Time series of the spatially averaged ellipsometric intensity $\overline{\xi}$ for three different measurements showing simple periodic oscillations (top), period-2 oscillations (middle) and oscillations with an irregular amplitude (bottom).

In the case of simple periodic oscillations in $\overline{\xi}$, 2d simulations using the suitably modified complex Ginzburg-Landau equation with a nonlinear global coupling show striking similarities with the patterns observed in the experiments [39, 93] (also in our published work Schmidt et al, Chaos, 2014). This opens a pathway to a deeper understanding of both the origin of pattern formation and of the coupling mechanism. Consequently, in the following the emphasis is first put on the analysis of the first class of patterns and the second and third classes are treated as modifications of this first class and are discussed later.

6.2 Simple periodic oscillations in $\overline{\xi}$: Experimental findings

In this section the experimental findings for the patterns forming during simple periodic $\overline{\xi}$ oscillations depicted in the top of Fig.(6.1), will be discussed. The regularity of the spatially averaged signal implies that the spatial variations of the patterns cancel out on average. There are two dominant types of spatio-temporal pattern dynamics forming. First, subharmonic phase clusters are found, where the ellipsometric intensity at each point shows oscillations with a strong frequency component at an integer fraction of the spatially averaged oscillation frequency. These points are arranged in phase domains where all points within a domain are synchronized and the distinct domains differ in their phase [39]. Typically but not exclusively, 2-phase clusters are found, i.e. clusters where the cluster frequency is half the frequency of the spatially averaged oscillation. The second type of dynamical behavior found are desynchronized oscillations with a broad distribution of oscillation frequencies. Hence, at any given point the oscillation amplitude of the ellipsometric intensity is irregular.

As already mentioned, typically the electrode forms different regions. In a region either one of the two patterns mentioned or a synchronized oscillation with the frequency of the spatially averaged signal exists. The occurrence of only one type of dynamical behavior on the entire electrode surface and any pairwise coexistence have been found in this study and are subsequently presented.

6.2.1 One region

First, we take a look at patterns with only one region covering the entire electrode. We start by discussing 2-phase clusters. An example is shown in Fig.(6.2). It is clear that the spatially averaged ellipsometric intensity $\overline{\xi}$ as well as the spatially averaged current density j oscillate in a simple periodic fashion. This oscillation is not uniform as can be seen in Fig.(6.2) b) where two snapshots of the ellipsometric images and the temporal evolution of a 1d cross section are depicted. Clearly, at every point, an amplitude variation can be seen which inverts every other oscillation. For a better visibility of the spatial distribution of the amplitude variations the underlying uniform oscillation is subtracted in Fig.(6.2) c), uncovering subharmonic local oscillations. The characteristics of this structure are further elucidated by the results of a Fourier analysis of the local time series at each point of the surface shown in Fig.(6.3). In Fig.(6.3) a), the spatial average of the absolute values of the pointwise Fourier spectra is compared to the Fourier spectrum of the spatially averaged ellipsometric intensity. The occurrence of an additional peak at half the dominant frequency can clearly be seen. The spatial distribution of absolute value and phase of the Fourier coefficient corresponding to this additional, subharmonic frequency are shown in Fig.(6.3) b). The latter is composed of two values which are π apart, confirming that a 2-phase cluster spreading across the entire electrode area is indeed present. The two clustered phase domains are separated by Ising-type walls, i.e., by a zero crossing of the absolute value of the Fourier coefficient where the phase jump occurs. This manifests itself in the black lines in the left hand picture of Fig.(6.3) b).

More insight into the details of the cluster dynamics can be gained by considering the analytical signal (see Sec.(2.4)) of points from the individual phase domains as shown in Fig.(6.4). The analytical signal of the points in the two areas indicated in Fig.(6.2) are arranged on a bar (blue and green points, respectively) whose center follows the analytical signal of $\overline{\xi}$ (black solid line). The end points of the bar, i.e. the points from the individual phase domains, trace a Moebius strip projected on the complex plane. This suggests that the subharmonic clusters result from a period doubling bifurcation of the uniform oscillation.

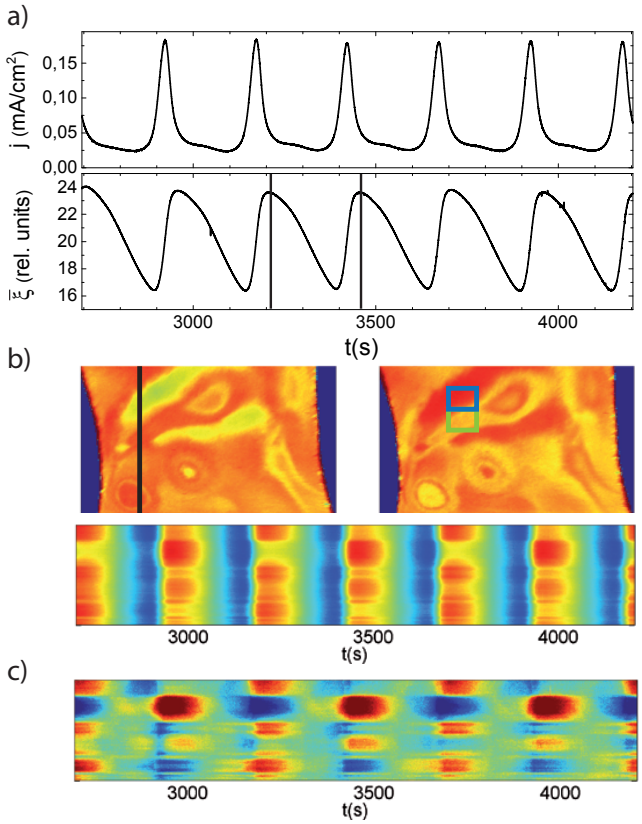

Figure 6.2: Subharmonic cluster pattern covering the entire electrode ($U = 8.65$ V vs. SHE, $c_F = 35$ mM, pH $= 1$, $R_{ext}A = 9.1$ kΩcm^2, $I_{ill} = 0.7$ mW/cm^2). a) Time series of j and $\bar{\xi}$; b) Ellipsometric intensity distribution on the electrode for the two times indicated by the vertical lines in a) and the temporal evolution of a 1d cut along the line indicated in the left electrode picture. Red indicates a relatively high and blue a relatively low ellipsometric intensity; c) 1d cut as in b) where $\bar{\xi}$ is subtracted from every local time series. The color scale is not identical to b).

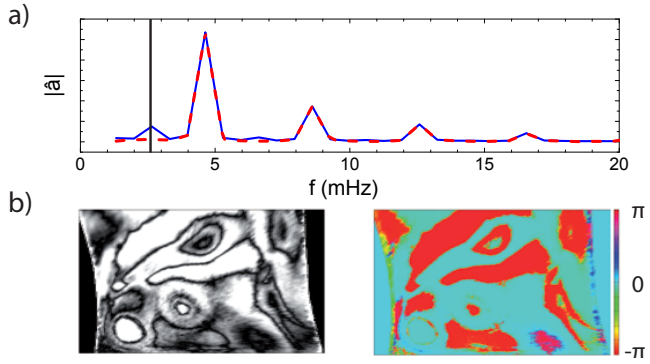

Figure 6.3: Fourier analysis of the subharmonic cluster pattern shown in Fig.(6.2). a) Spatial average of the absolute values of the pointwise Fourier spectra (blue) and Fourier spectrum of the spatially averaged signal $\bar{\xi}$ (red); b) Spatial distribution of the absolute value (left) and phase (right) of the Fourier coefficient corresponding to the Fourier mode indicated by the vertical line in the Fourier spectra in a).

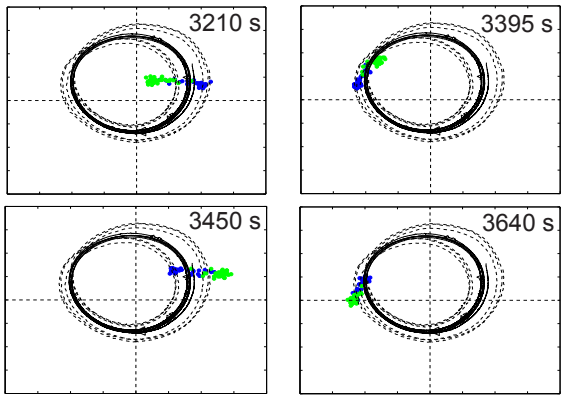

Figure 6.4: Analytical signal from the points indicated by correspondingly color coded rectangles in Fig.(6.2) b) at four consecutive extrema of the $\overline{\xi}$ oscillation shown in Fig.(6.2) a) together with the traces of the analytical signal of $\overline{\xi}$ (solid) and a point located in the center of the blue rectangle in Fig.(6.2) (dash).

The four snapshots in Fig.(6.4) are taken at consecutive extrema of $\overline{\xi}$ and the sequence of pictures thus shows that a full rotation of the bar is accompanied by two full rotations of its center mirroring the subharmonic dynamics.

The second type of dynamical pattern covering the entire active area observed is a desynchronized oscillation spreading across the entire electrode as shown in Fig.(6.5).

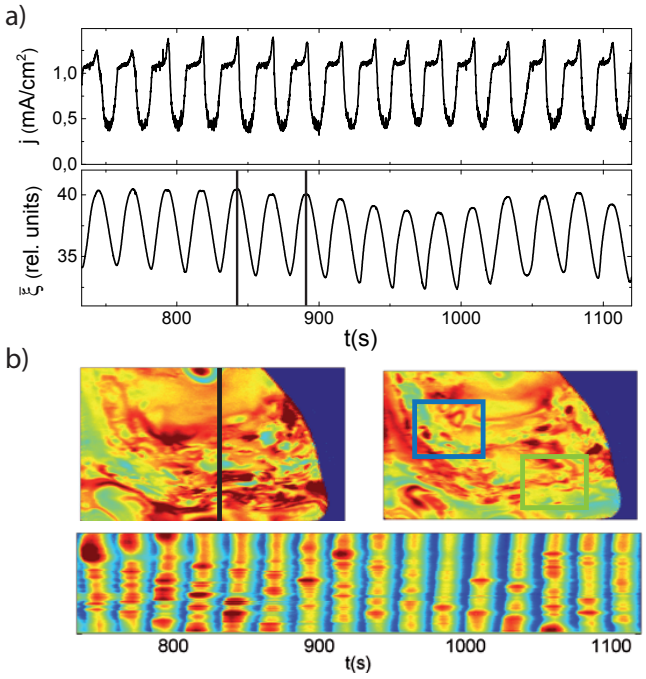

Figure 6.5: Desynchronized oscillation pattern covering the entire electrode ($U = 8.65$ V vs. SHE, $c_F = 75$ mM, pH $= 1$, $R_{ext}A = 0$ kΩcm^2, $I_{ill} = 2.0$ mW/cm^2). a) Time series of j and $\overline{\xi}$; b) Ellipsometric intensity distribution on the electrode for the two times indicated by the vertical lines in a) and the temporal evolution of a 1d cut along the line indicated in the left electrode picture. Red indicates a relatively high and blue a relatively low ellipsometric intensity.

Here, the remarkable case is shown where the ensemble of pointwise time series of the ellip-

sometric intensity across the surface is oscillating in a desynchronized manner while in the spatially averaged signal these differences cancel out almost perfectly leaving a simple periodic oscillation in $\overline{\xi}$ and j. The corresponding full analytical signal of two sets of points on the electrode further illustrates this behavior. It is shown in Fig.(6.6).

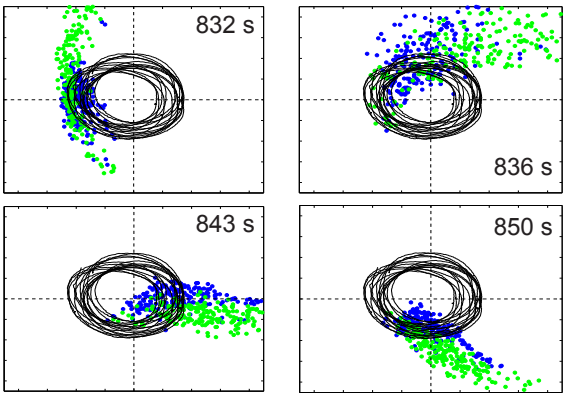

Figure 6.6: Analytical signal from the points indicated by correspondingly color coded rectangles in Fig.(6.5) b) at four points during one oscillation period of the $\overline{\xi}$ oscillation shown in Fig.(6.5) a) together with the trace of the analytical signal of $\overline{\xi}$ (solid).

The trajectories of the individual points are uncorrelated, both within the two areas shown and between them, leading to broad point clouds circling the origin.

6.2.2 Two regions

A region of one distinct dynamical behavior is typically not covering the entire electrode. More often two such regions are observed to coexist on the electrode. In Fig.(6.7) an example for the coexistence of a 2-phase cluster with an approximately synchronous oscillation with the frequency of the spatially averaged signal is depicted. The two regions are clearly distinguishable in Fig.(6.7) b) with the 2-phase cluster showing a remarkably fine structured, sharp border between its two phase domains. Note that the spatially averaged signals still oscillate in a simple periodic manner.

The Fourier analysis of this pattern is shown in Fig.(6.8). Outside the clustered domain the subharmonic frequency is inactive as can be seen in Fig.(6.8) b). As in the experiment where the 2-phase cluster covers the entire electrode shown in Figs.(6.2)-(6.4), the domain walls are Ising-type walls. The analytical signal of points from three areas on the electrode is shown in Fig.(6.9). Two main results can be read from the analytical signal in Fig.(6.9). First, the center of the rotating bar formed by the two domains of the 2-phase cluster and their separating wall is now approximately stationary in the origin. This means that the underlying harmonic frequency of the spatially averaged signal is strongly suppressed in the region of the 2-phase cluster. Second, the trajectory of the points taken from the approximately synchronized region does not follow the trace of the spatially averaged analytical signal perfectly. This can also be seen in the one dimensional cut in Fig.(6.7) b) where the active phase seems to propagate across the surface. We treat this, however, as a minor variation of a perfectly uniform oscillating region. Actually, the region oscillating with the frequency of the spatially averaged signal in a synchronous manner tends to this wave-like disturbance easily.

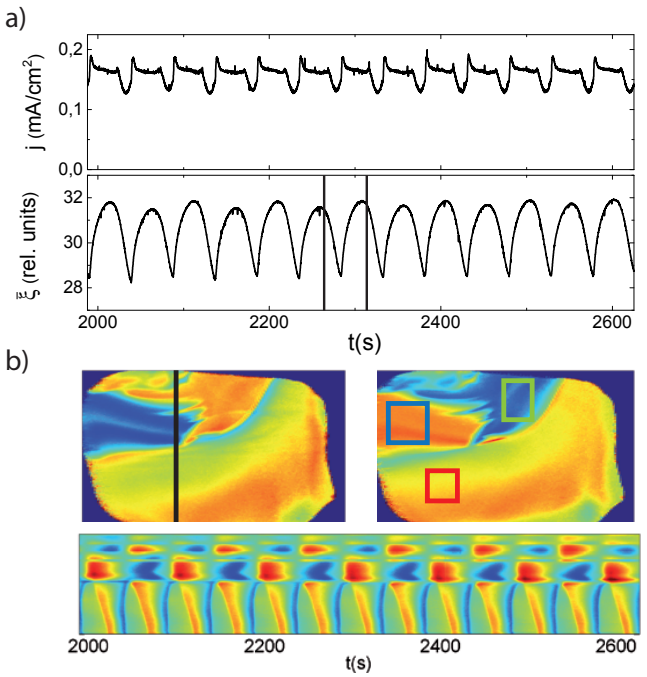

Figure 6.7: A pattern consisting of a synchronized region coexisting with a subharmonic 2-phase cluster ($U = 8.65$ V vs. SHE, $c_F = 50$ mM, pH $= 1$, $R_{ext}A = 0.69$ kΩcm^2, $I_{ill} = 0.4$ mW/cm^2). a) Time series of j and $\bar{\xi}$; b) Ellipsometric intensity distribution on the electrode for the two times indicated by the vertical lines in a) and the temporal evolution of a 1d cut along the line indicated in the left electrode picture. Red indicates a relatively high and blue a relatively low ellipsometric intensity.

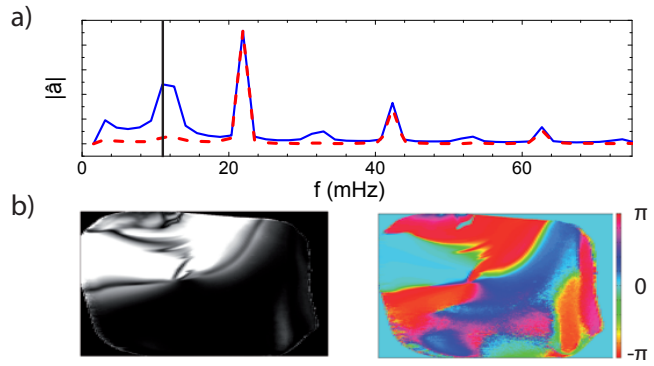

Figure 6.8: Fourier analysis of the pattern shown in Fig.(6.7). a) Spatial average of the absolute values of the pointwise Fourier spectra (blue) and Fourier spectrum of the spatially averaged signal $\bar{\xi}$ (red); b) Spatial distribution of the absolute value (left) and phase (right) of the Fourier coefficient corresponding to the Fourier mode indicated by the vertical line in the Fourier spectra in a).

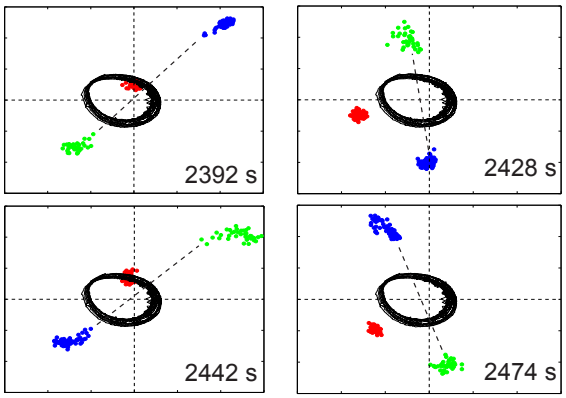

Figure 6.9: Analytical signal from the points indicated by correspondingly color coded rectangles in Fig.(6.7) b) at four points during two oscillation periods of the $\overline{\xi}$ oscillation shown in Fig.(6.7) a) together with the trace of the analytical signal of $\overline{\xi}$ (solid). The dashed line represents points in the Ising wall between the two phase domains.

Another interesting point arises comparing the measurement where the 2-phase cluster covers the entire electrode shown in Figs.(6.2)-(6.4) to the measurement showing coexistence of the 2-phase cluster and synchronized, harmonic oscillation shown in Figs.(6.7)-(6.9). The transition from the former to the latter dynamical state is seemingly achieved by spatially decomposing the two active frequencies. This is best seen by the corresponding deconvolution of the movement of the bar in the analytical signal shown in Fig.(6.4) into a pure rotation of the bar around the origin and a pure center of mass rotation around the origin in the different regions on the electrode as shown in Fig.(6.9). The frequency ratio between the center of mass movement and the rotation of the bar remains unaffectedly 1:0.5. A further investigation of this possible deconvolution process is desirable but we have not done this so far in a systematic manner.

The next case frequently found in the experiments is the coexistence of a synchronized and a desynchronized region on the electrode. This dynamical state is typically called chimera state, has attracted a lot of research interest in recent years and has been realized in diverse experimental settings [88, 89, 94, 95, 96, 97, 98, 99]. While in most experiments in the literature these states have to be initialized in a special way and, moreover, rely on a computer-generated and especially designed spatial coupling feedback, their spontaneous occurrence in our system is especially interesting [100]. An example of such a chimera state in our system is shown in Fig.(6.10). Note that while a region of desynchronized local oscillations can easily be seen in Fig.(6.10) b), the spatial average is again unaffected. Furthermore, the region of synchronized oscillations seems to be less perturbed by the presence of the region of desynchronized oscillations than by the presence of the subharmonic 2-phase cluster as discussed for Fig.(6.7). The coexistence of the two dynamical regions is further emphasized in Fig.(6.11) where the analytical signal of points from three areas on the surface shows the qualitative difference between the synchronized and the desynchronized oscillations.

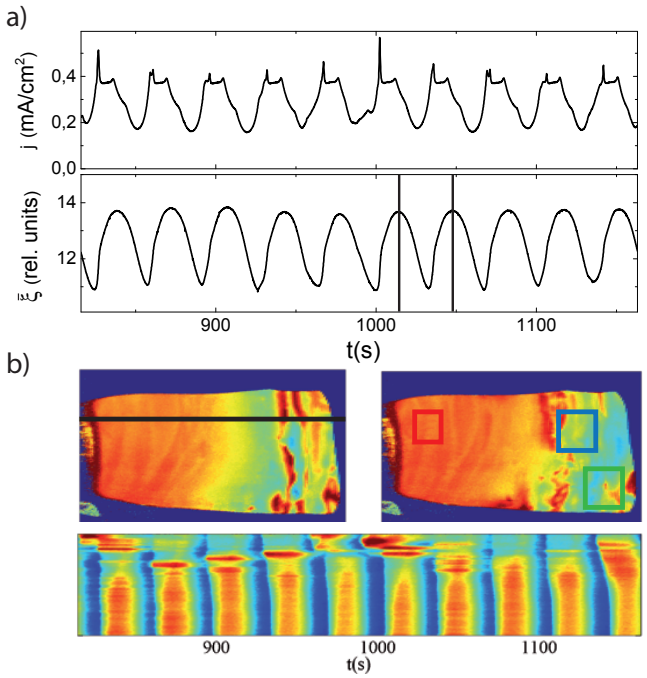

Figure 6.10: A chimera state consisting of a synchronized and a desynchronized region (U = 8.65 V vs. SHE, $c_{\mathrm{F}} = 75$ mM, pH = 3.5, $R_{\mathrm{ext}}A = 5.61$ kΩcm^2, $I_{\mathrm{ill}} = 1.8$ mW/cm^2). a) Time series of j and $\bar{\xi}$; b) Ellipsometric intensity distribution on the electrode for the two times indicated by the vertical lines in a) and the temporal evolution of a 1d cut along the line indicated in the left electrode picture. Red indicates a relatively high and blue a relatively low ellipsometric intensity.

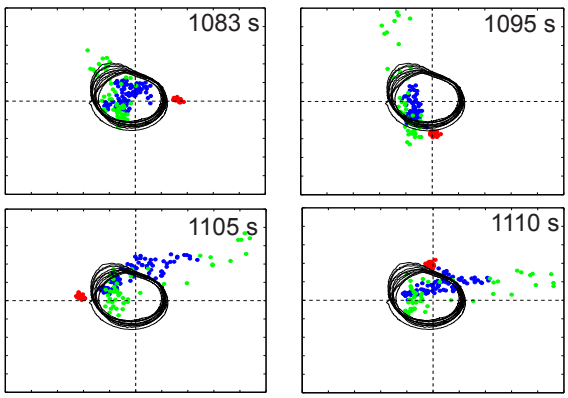

Figure 6.11: Analytical signal from the points indicated by correspondingly color coded rectangles in Fig.(6.10) b) at four points during one oscillation period of the $\bar{\xi}$ oscillation shown in Fig.(6.10) a) together with the trace of the analytical signal of $\bar{\xi}$ (solid).

Another type of chimera state on the electrode arises in the case of the coexistence of a 2-phase cluster with a desynchronized region as shown in Fig.(6.12).

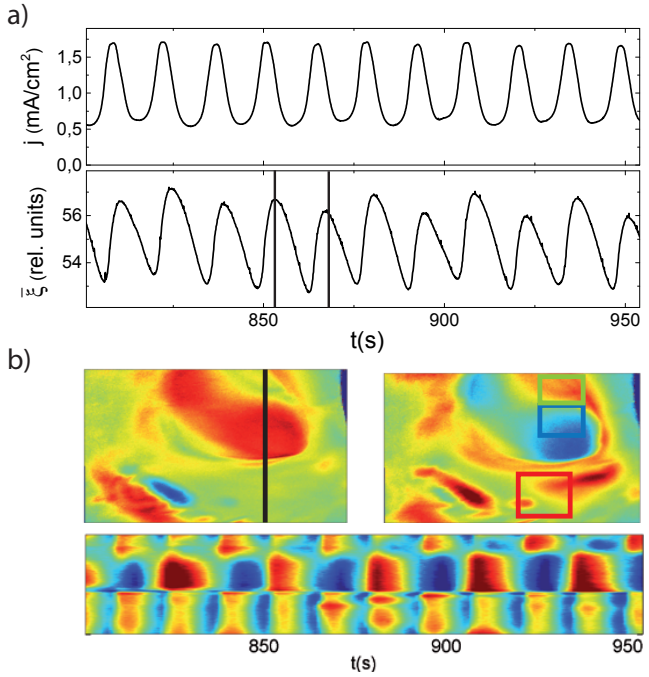

Figure 6.12: A chimera state consisting of a 2-phase cluster and a desynchronized region (U = 8.65 V vs. SHE, c_F = 100 mM, pH = 3.5, $R_{ext}A$ = 2.81 kΩcm^2, I_{ill} = 2.7 mW/cm^2). a) Time series of j and $\overline{\xi}$; b) Ellipsometric intensity distribution on the electrode for the two times indicated by the vertical lines in a) and the temporal evolution of a 1d cut along the line indicated in the left electrode picture. Red indicates a relatively high and blue a relatively low ellipsometric intensity.

Here, the individual domains in the 2-phase cluster are again synchronized, show a phase difference of π and are separated by Ising-type walls. This is further elucidated in the analytical signal obtained from points spreading across the Ising-type wall in Fig.(6.13) (blue and green points).

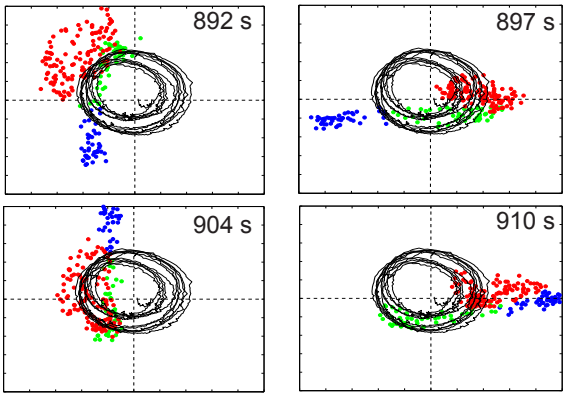

Figure 6.13: Analytical signal from the points indicated by correspondingly color coded rectangles in Fig.(6.12) b) at four points during two oscillation periods of the $\overline{\xi}$ oscillation shown in Fig.(6.12) a) together with the trace of the analytical signal of $\overline{\xi}$ (solid).

Comparable to Fig.(6.4) these points form a bar that rotates at half the angular frequency of the $\overline{\xi}$ oscillation. In contrast, the points from the desynchronized region, displayed in red,

spread out in a cloud. It has to be noted that a slight period-2 perturbation is visible in the oscillation of $\overline{\xi}$ in Figs.(6.12) and (6.13). This point will be further discussed in Sec.(6.4.1).

6.3 Simple periodic oscillations in $\overline{\xi}$: Theoretical interpretation

Here the experimental findings presented in the last section will be interpreted using a generic theoretical ansatz. It is thereby shown that the patterns can be well described as a purely dynamical phenomenon. This means that the specifics of the system, for example the question why the oscillations arise, are inessential for an explanation of the pattern formation. In contrast, the patterns observed can be expected in any field of oscillators originating from a Hopf bifurcation at parameters sufficiently close to the bifurcation point under a suitable global coupling.

The appropriate normal form for a reaction-diffusion system close to a Hopf bifurcation is the complex Ginzburg-Landau equation [17, 101, 102]

$$\partial_t W = W + (1 + ic_1)\nabla^2 W - (1 + ic_2)|W|^2 W. \tag{6.1}$$

Here W is the complex amplitude of the individual oscillators where $\mathrm{Re}(W)$ and $\mathrm{Im}(W)$ can be viewed as the oscillations of two essential, physical variables such as in our case the ellipsometric intensity ξ at each point, and $c_{1,2}$ are two free parameters. In a system described by the complex Ginzburg-Landau equation the oscillators are only diffusively coupled, i.e. the coupling is short range. The experiments presented in Sec.(6.2) deviate in two important aspects from the assumptions underlying Eq.(6.1). First, the oscillators are coupled with a long-range or even global coupling as discussed in Chap.(5) and, second, the spatially averaged signal $\overline{\xi}$ itself oscillates in a simple periodic manner. Both deviations can be incorporated in the complex Ginzburg-Landau equation by introducing a nonlinear global coupling between all points at the surface. The thus modified equation then takes the form

$$\partial_t W = W + (1 + ic_1)\nabla^2 W - (1 + ic_2)|W|^2 W - (1 + i\nu)\langle W\rangle + (1 + ic_2)\langle |W|^2 W\rangle, \tag{6.2}$$

and is subsequently called modified, complex Ginzburg-Landau equation (MCGLE). The modification introduced in the MCGLE is the most straight forward way to ensure an oscillatory behavior of the spatially averaged amplitude $\langle W\rangle$ while making use of a global coupling only. The spatially averaged dynamics can indeed by read out easily as the spatial average over the Laplace operator vanishes

$$\partial_t \langle W\rangle = -i\nu\langle W\rangle \quad \Rightarrow \quad \langle W\rangle = \eta e^{i\nu t}. \tag{6.3}$$

with the complex amplitude η of the spatially averaged oscillation. The MCGLE as a theoretical approach to model the experimental system then shows striking similarities with the experimental results shown so far, and all types of patterns encountered in the experiments could be found in theoretical simulations as well.

6.3.1 Cluster patterns

The possibility of the occurrence of cluster patterns in simulations of the MCGLE Eq.(6.2) is in itself a nontrivial result and a symmetry breaking caused by the nonlinearity of the global coupling is essential to their formation [93]. Qualitatively, the patterns can arise in the exclusively globally coupled system since the global response to any perturbation, exerted on all the oscillators equally at any point in time, still has a different effect on oscillators differing in phase or amplitude due to the nonlinear characteristics of the global coupling.

The simplest case of symmetry breaking in systems described by the MCGLE Eq.(6.2) is then the occurrence of two phase shifted limit cycles which both attract groups of oscillators resulting in stable cluster patterns. This mechanism has then been shown to be fundamental for the further generation of the pattern dynamics and the cluster patterns are thus the starting point for all forms of patterns formation encountered [103, 104]. In Fig.(6.14) the experimental cluster pattern shown in Fig.(6.2) is compared to a corresponding theoretical simulation.

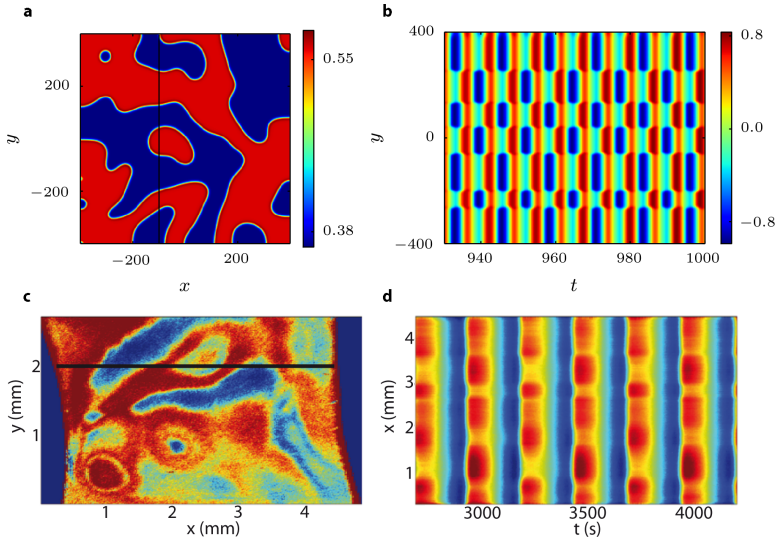

Figure 6.14: Two-phase clusters in theory (a,b) and experiment (c,d). (a) Snapshot of the two-dimensional oscillatory medium in the theory. Shown is the real part of W. (b) Spatio-temporal dynamics in an one-dimensional cut versus time in the theory. (c,d) The same as (a,b) now for the experimental results. The simulation captures the experimental dynamics very well. Note that the color bars are different for each subfigure. Parameters read: $c_1 = 0.2$, $c_2 = -0.58$, $\nu = 1.0$, $\eta = 0.66$ **(simulation) and** $U = 8.65$ V vs. SHE, $c_F = 35$ mM, pH $= 1$, $R_{ext}A = 9.1$ kΩcm^2, $I_{ill} = 0.7$ mW/cm^2 **(experiment).**

The strong resemblance of the theoretical and experimental results evident in Fig.(6.14) can be elucidated further by comparing the pointwise Fourier spectra of the two datasets. This comparison is shown in Fig.(6.15). Note that the experimental results shown in Fig.(6.15) f) are from the full measured avi-video and not only from a part. This explains the few points not situated on a straight line which occur at the border of the electrode. Apart from the similarities between experiment and theory there is one major difference. In the theory the cluster frequency is in principle free as the clusters arise in a secondary Hopf bifurcation. In contrast to this subharmonic 2-phase clusters are by far the most prominent example for cluster patterns found in the experiments. These subharmonic 2-phase clusters seem to emerge from a period doubling bifurcation rather than the more general secondary Hopf bifurcation. We thus conclude that there is an additional mechanism or restriction leading to the preferred occurrence of 2-phase clusters with a cluster frequency of $\nu/2$ in the experiments which is not captured by the generic theoretical approach.

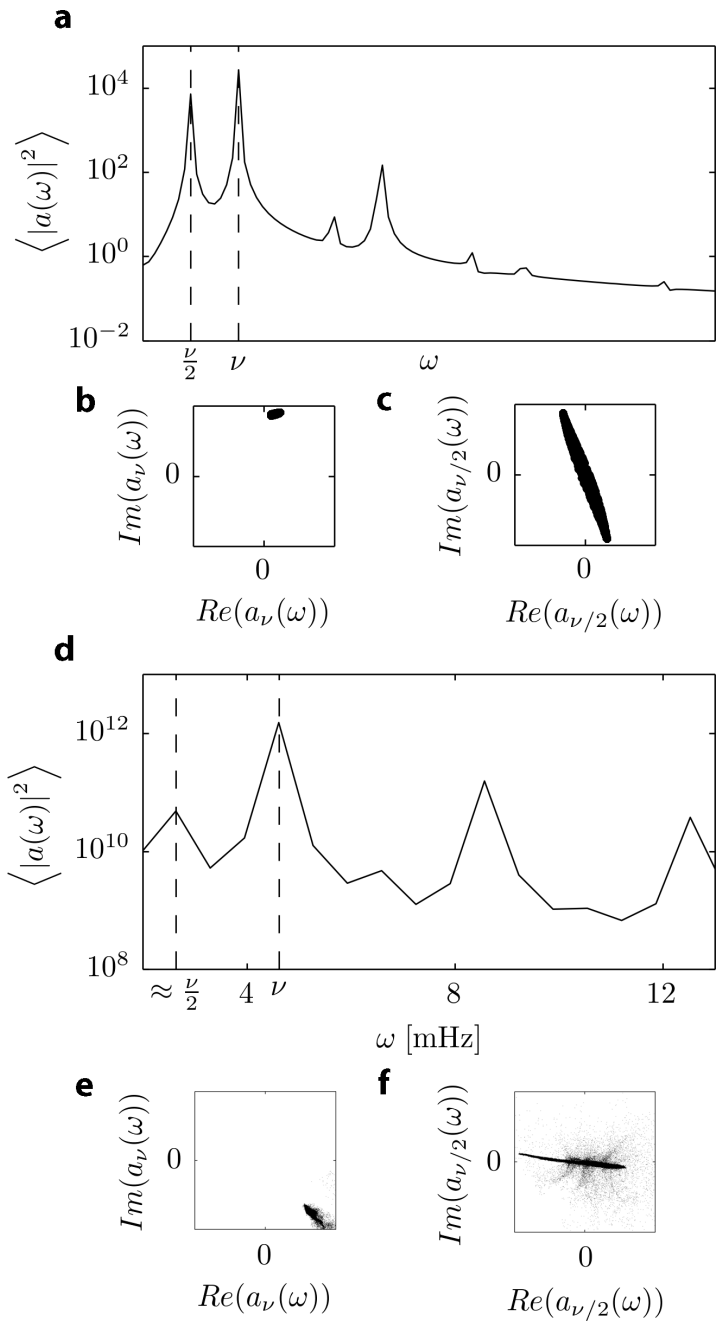

Figure 6.15: (a,d) Cumulative power spectra for experiments and simulations, respectively. The two major peaks at frequencies ν and approximately $\nu/2$ are indicated. The arrangement of the local Fourier amplitudes in the complex plane corresponding to these peaks are depicted in (b) and (c) for the theory and (e) and (f) for the experiments, respectively. The whole two-dimensional system is considered, which leads to the scattered oscillators in the experimental result in (f).

The coexistence of clusters and uniformly oscillating regions as shown in Fig.(6.7) was also found in the theoretical simulations. In this case one of the two original cluster domains splits up into two cluster domains in what appears to be a period doubling bifurcation. A comparison between a theoretical simulation showing this behavior and an experimental example is shown in Fig.(6.16).

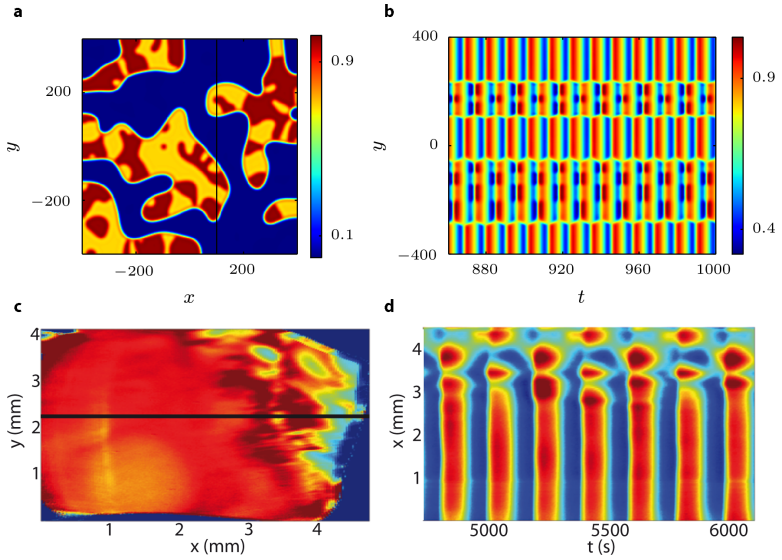

Figure 6.16: Subclustering in theory (a,b) and experiment (c,d). Snapshots (a,c) and one-dimensional cuts (b,d) are shown. The system splits into two regions, one region being homogeneous and one exhibiting 2-phase clusters as a substructure. Note that in (b) for better visibility $|W(y,t)|$ is shown. Parameters read: $c_1 = 0.2$, $c_2 = -0.67$, $\nu = 0.1$, $\eta = 0.66$ (simulation) and $U = 8.65$ V vs. SHE, $c_F = 35$ mM, pH $= 1$, $R_{ext}A = 7.6$ kΩcm^2, $I_{ill} = 0.5$ mW/cm^2 (experiment).

Again a strong similarity between experiments and theory is evident. There are, however, a few points where both deviate. As already discussed in Fig.(6.9), the two modes active in the experimental system are spatially segregated, a behavior that is not reproduced in the theoretical simulations. In contrast, in Fig.(6.16) b), the simulations show clearly the two levels of clustering. The original cluster formation already discussed above is visible in the phase shift between the maxima in the uniform and the subclustered region. For the observed difference between experiment and theory the spatial segregation seems to be of central importance.

6.3.2 Turbulence and chimera states

From the viewpoint of the theory the second class of patterns contains at least one region with turbulent dynamics. This includes a turbulent oscillation present at the entire electrode and chimera states, where the latter are subdivided into the coexistence of a uniform and a turbulent region and of a 2-phase cluster and a turbulent region. A comparison between experimental results and theoretical simulations is shown in Fig.(6.17). Again a strong resemblance between experimental results and theoretical simulations is evident. The theoretical understanding of the occurrence of chimera states follows a similar path as in the case of coexisting cluster states discussed in the last section. Again the initial clustering is followed by a subsequent destabilization of one of the clusters. The similarity between the theoretical simulations and the experimental results seems to be more close in the case of turbulent patterns than in the case of 2-phase clusters discussed in the last section. Especially for the chimera states where a synchronous region coexists with a turbulent one, no qualitative differences

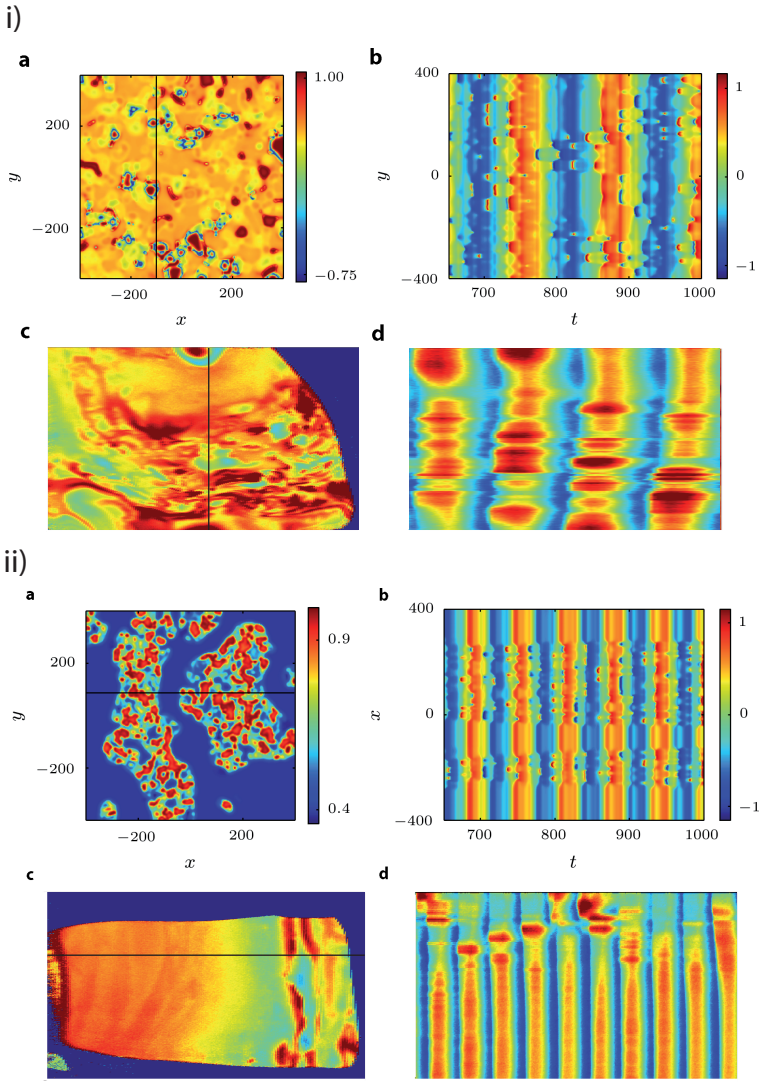

Figure 6.17: i: Turbulent oscillations in theory (a,b) and experiment (c,d). Snapshots (a,c) and one-dimensional cuts (b,d) are shown. Parameters read: $c_1 = 0.2$, $c_2 = -0.58$, $\nu = 0.05$, $\eta = 0.66$ **(simulation) and** $c_F = 75$ mM, pH $= 1$, $R_{ext}A = 0$ kΩcm^2, $I_{ill} = 2.0$ mW/cm^2 **(experiment). ii) Chimera states where the system splits into two regions, one region being homogeneous and one exhibiting 2-phase clusters as a substructure in theory (a,b) and experiment (c,d). Parameters read:** $c_1 = 0.2$, $c_2 = -0.58$, $\nu = 0.1$, $\eta = 0.66$ **(simulation) and** $U = 8.65$ V vs. SHE, $c_F = 75$ mM, pH $= 3.5$, $R_{ext}A = 5.6$ kΩcm^2, $I_{ill} = 1.8$ mW/cm^2 **(experiment).**

can be found.

6.4 More complex oscillations in $\overline{\xi}$

In this part we discuss patterns that are accompanied by more complex oscillation forms of $\overline{\xi}$ than the simple periodic ones discussed so far. This contains patterns which are stable in time as well as the last level of complexity discussed in this work, namely the occurrence of long term changes in the local dynamics in the coexistence patterns. While these types of patterns are not describable by our theoretical ansatz as the spatially averaged signal of the

ellipsometric intensity is not simple periodic, there are still some striking similarities between some simulations and the patterns. This suggests that the deviation in the spatially averaged signal might be of minor importance there or could be seen as a higher order effect.

6.4.1 Period-2 oscillations in $\overline{\xi}$

The least complex deviation from the simple periodic oscillations in $\overline{\xi}$ is the occurrence of period-2 oscillations in $\overline{\xi}$ as shown in the middle of Fig.(6.1). In all experiments where this behavior is found it is accompanied by the formation of a 2-phase cluster region where one phase domain covers a larger area or has a higher amplitude in the subharmonic mode than the other. An example is shown in Fig.(6.18). In the distribution of amplitude and phase of the Fourier coefficient of the subharmonic mode in the lower images of Fig.(6.18) c) the lack of balance between the phase domains of the 2-phase cluster becomes apparent. The difference between the unbalanced and the balanced case is visualized in Fig.(6.19) by an overlay of the amplitude and phase plots of the Fourier coefficients of the subharmonic mode for the patterns shown in Figs.(6.18) (unbalanced) and (6.7) (balanced), respectively. While the two phase domains on the left hand side of the unbalanced electrode in Fig.(6.19) are of similar size and the amplitude of the Fourier coefficient in these domains is similar, there is no counterbalancing phase domain for the domain in the upper right corner. For this reason the phase color coded as purple in Fig.(6.18) c) is also visible as an amplitude variation in the spatially averaged ellipsometric intensity signal. Whenever the average signal $\overline{\xi}$ of a patterned electrode oscillates with a period-2, unbalanced 2-phase clusters are present. Since period-2 oscillations are also found for spatially uniform oscillations, it is not clear here whether one of these two phenomena can be seen as cause of the other.

6.4.2 Irregular oscillations in $\overline{\xi}$

The next type of patterns is accompanied by an irregular oscillation of $\overline{\xi}$ as shown in the bottom of Fig.(6.1). In this case three different pattern categories are distinguished. The first category, shown in Fig.(6.20), can again be seen as a deviation from the case of simple periodic spatial average oscillations. Here the irregular oscillation of the spatial average is imposed on the entire electrode and the relative intensity of the maxima and minima of $\overline{\xi}$ in Fig.(6.20) a) can be traced in the synchronized region in the lower part of the one dimensional cut in Fig.(6.20) b). A striking similarity between this type of pattern and the patterns forming accompanied by a simple periodic oscillation in $\overline{\xi}$ is that the regions on the electrode retain their respective dynamical behaviors and sizes until the measurement is finished. Spatially uniform oscillations with an irregular amplitude are also encountered with p-type and highly illuminated n-type silicon samples, i.e. in the absence of the nonlinear coupling. For this reason the measurement shown in Fig.(6.20) can be seen as a peculiar deviation from the chimera state shown in Fig.(6.10). The synchronized part exhibits deterministic low-dimensional chaotic dynamics and coexists with a spatially desynchronized turbulent region. The dynamical state shown in Fig.(6.20) is in this view caused by the nonlinear coupling imposed on a spatially uniform oscillation with irregular, most likely chaotic, dynamics, while the chimera state shown in Fig.(6.10) is caused by the nonlinear coupling acting on a simple periodic, spatially uniform oscillation. This then raises the question if the irregularity of the spatially averaged quantities is a higher order phenomenon while the underlying cause of the spatial segregation into different dynamics is still identical. Further study on this is thus of interest.

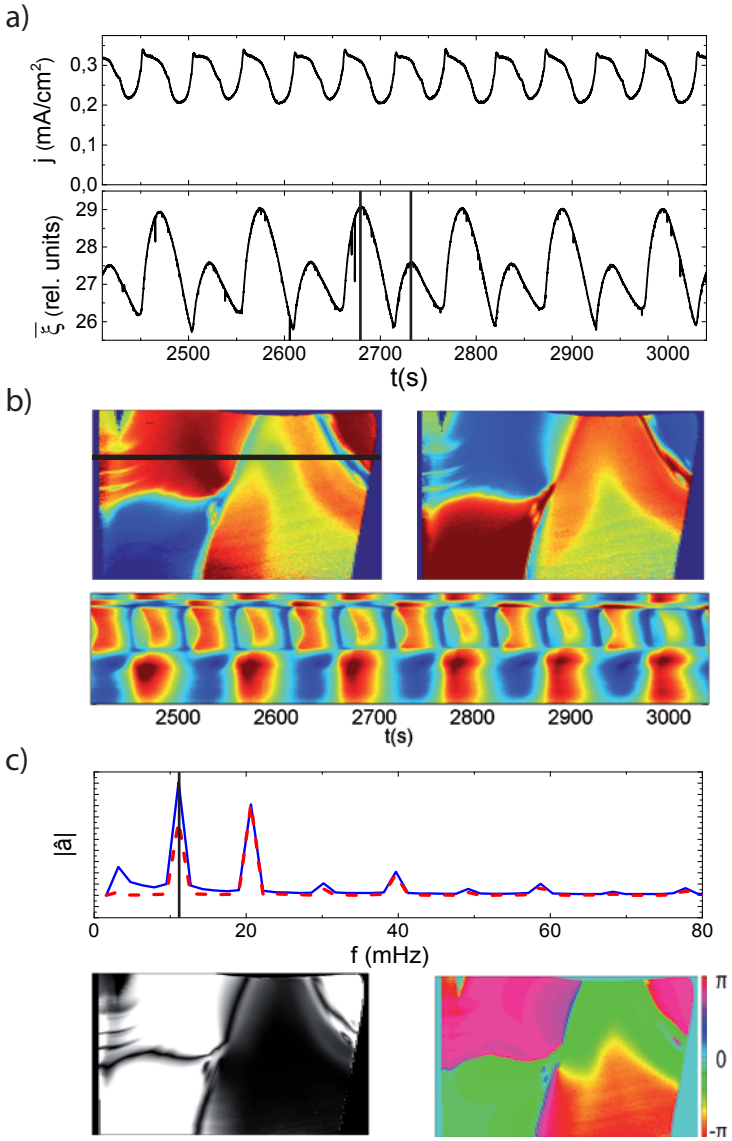

Figure 6.18: A pattern consisting of a 2-phase cluster and a desynchronized region (U = 8.65 V vs. SHE, c_F = 50 mM, pH = 1, $R_{ext}A$ = 2.61 kΩcm^2, I_{ill} = 0.4 mW/cm^2). a) Time series of j and $\overline{\xi}$; b) Ellipsometric intensity distribution on the electrode for the two times indicated by the vertical lines in a) and the temporal evolution of a 1d cut along the line indicated in the left electrode picture. Red indicates a relatively high and blue a relatively low ellipsometric intensity; c) Fourier analysis of the pattern shown in a). Spatial average of the absolute values of the pointwise Fourier spectra (blue) and Fourier spectrum of the spatially averaged signal $\overline{\xi}$ (red) and the spatial distribution of the absolute value (left) and phase (right) of the Fourier coefficient corresponding to the Fourier mode indicated by the vertical line in the Fourier spectra.

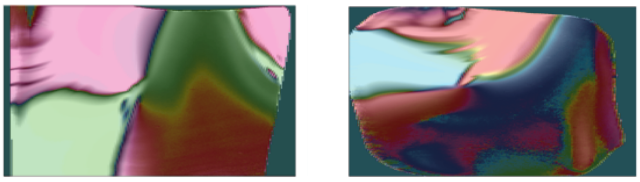

Figure 6.19: Comparison between the spatial distribution of absolute value and phase of the Fourier coefficients of a subharmonic cluster with different phase domain sizes and one with identical phase domain sizes.

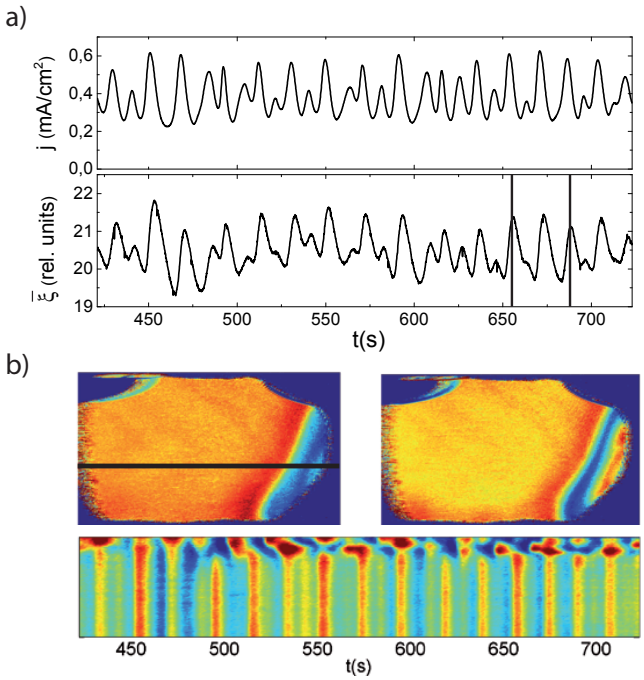

Figure 6.20: Analysis of a chimera type pattern occurring during an irregular $\overline{\xi}$ oscillation (8.65 V vs. SHE, $c_F = 75$ mM, pH $= 1$, $R_{ext}A = 6.51$ kΩcm^2, $I_{ill} = 3.0$ mW/cm^2). a) Time series of j and $\overline{\xi}$; b) Ellipsometric intensity distribution on the electrode for the two times indicated by the vertical lines in a) and the temporal evolution of a 1d cut along the line indicated in the left electrode picture. Red indicates a relatively high and blue a relatively low ellipsometric intensity.

6.4.3 Long term variations

The other two categories of patterns forming during oscillations of $\overline{\xi}$ with an irregular amplitude are qualitatively different from all other types of patterns considered so far and they introduce an additional level of complex structure formation, the last of these levels discussed in this work denoted 'long term variation' in Fig.(1.1). The most important new feature is that the regions spontaneously forming on the electrode, while still well distinguishable, show dynamical behavior slowly varying with time. A first example of such spatio-temporal pattern formation is shown in Fig.(6.21). One important feature the spatio-temporal pattern shown in Fig.(6.21) shares with all spatio-temporal patterns shown so far, is that the regions with distinct dynamical behavior do not change their shape, as is well visible in the temporal evolution of the cross section in Fig.(6.21) b). The important new feature is instead that the dynamical behavior in the region in the middle of the cross section changes significantly twice on a long time scale from a completely desynchronized oscillation pattern to a nearly synchronized oscillation pattern with a significantly lower amplitude and back. These profound

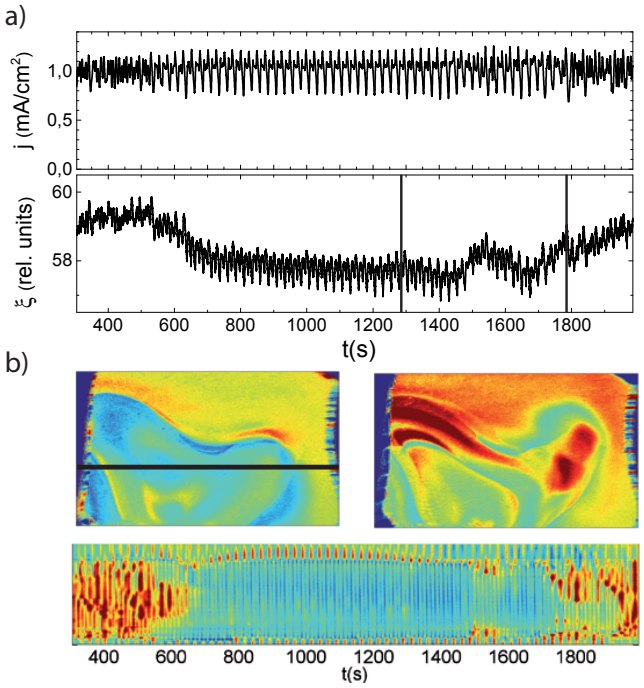

Figure 6.21: Analysis of a spatio-temporal pattern showing temporarily changing dynamical behavior within regions with stable walls (U = 8.65 V vs. SHE, c_F = 60 mM, pH = 2.3, $R_{ext}A$ = 2.41 kΩcm^2, I_{ill} = 1.0 mW/cm^2). a) Time series of j and $\overline{\xi}$; b) Ellipsometric intensity distribution on the electrode for the two times indicated by the vertical lines in a) and the temporal evolution of a 1d cut along the line indicated in the left electrode picture. Red indicates a relatively high and blue a relatively low ellipsometric intensity.

changes in the overall behavior are also visible in the time series of $\overline{\xi}$.

Another qualitatively different behavior where the walls of the regions themselves are moving is shown in Fig.(6.22). Most of the electrode forms a chimera state for most of the time as can be best seen in the 1d cut for example around t = 1000 s. The respective sizes of the coherent and the incoherent domains change, however, throughout the measurement. This is well visible in the two electrode images where the coherent and incoherent region have switched places between the two points in time the pictures were taken.

While the requirement for the theoretical simulations is not met by the irregularly oscillating spatially averaged signal, it is still interesting that long term variations of the oscillations quite similar to the experimental findings are also found there. An example for this are states which were called 'alternating chimera states' where the synchronized and the incoherent region switch places periodically in a rather similar fashion as in Fig.(6.22) [105]. These similarities then again lead to the picture that the long term variations in the spatially averaged signals are not themselves lowest order phenomena but inessential deviations from the ideal behavior described by the MCGLE.

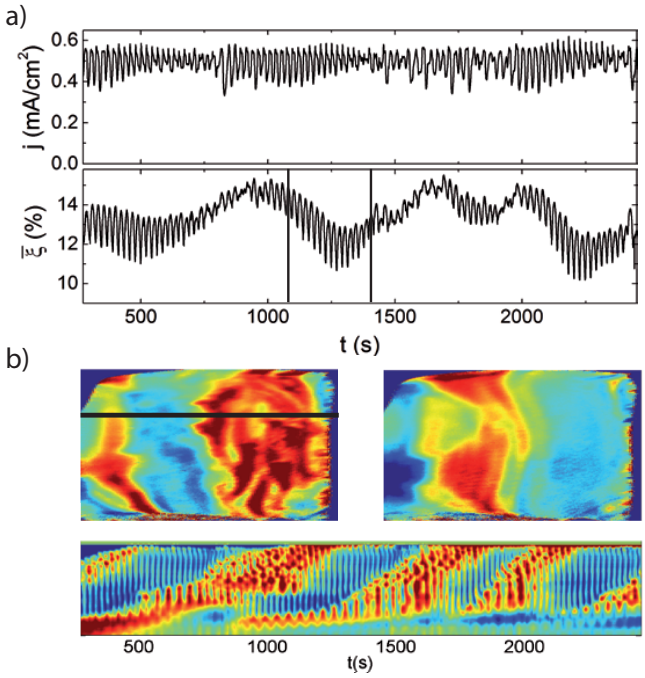

Figure 6.22: Analysis of a spatio-temporal pattern showing periodical changes in the region sizes ($U = 8.65$ V vs. SHE, $c_F = 75$ mM, pH $= 1$, $R_{ext}A = 1.6$ kΩcm^2, $I_{ill} = 1.7$ mW/cm^2). a) Time series of j and $\overline{\xi}$; b) Ellipsometric intensity distribution on the electrode for the two times indicated by the vertical lines in a) and the temporal evolution of a 1d cut along the line indicated in the left electrode picture. Red indicates a relatively high and blue a relatively low ellipsometric intensity.

6.5 Summary and discussion

We presented a variety of self-organized spatio-temporal patterns forming in the ellipsometric intensity during the oscillatory photo-electrodissolution of n-type silicon under limited illumination. Remarkably, different regions of distinct dynamical behavior formed spontaneously under spatially uniform experimental parameters which were kept constant in time. We classified these patterns according to the behavior of the spatially averaged signal of the ellipsometric intensity $\overline{\xi}$, the dominant case being a simple periodic oscillation of $\overline{\xi}$. In this case, the patterns included synchronized oscillations, subharmonic 2-phase clusters emerging from the uniform oscillation by a period doubling bifurcation and desynchronized oscillations. Any pairwise coexistence of such dynamical regions was found including the first experimental realizations of fully self-organized chimera states. These patterns could be reproduced quite well by a generic, normal form approach in theoretical simulations using a nonlinear global coupling. This leads us to two important conclusions. First, the patterns are dynamical phenomena and not caused by any irregularities in either electrode surface or experimental parameters. They are the natural outcome of the uniform parameters and driving forces exerted on the system and thus should challenge our intuition about such systems far away from equilibrium. Second, the good agreement between experiments and theory clearly corroborates the notion that the coupling range of the illumination-induced coupling is partially global and that this global component is responsible for the occurrence of the patterns. This might strain intuition which would rather see the patterns as an outcome of the interplay of local disturbances and a local coupling. In addition to the case of simple periodic oscillations in $\overline{\xi}$, patterns accompanied by period-2 and irregular oscillations in $\overline{\xi}$ have been presented. In the former case, unbalanced 2-phase clusters were always present on the electrode, linking the

period-2 oscillation of $\overline{\xi}$ to the lack of phase balance. The latter case opens a wide variety of possible patterns which were classified by the stability of the region walls and their long term behavior but not yet studied in detail. It is, however, remarkable here that again similar situations are found in theoretical simulations and that these types of patterns might thus also be caused by the nonlinearity of the global component of the coupling rather than by local effects.

The presented occurrence of patterns where different dynamical states coexist under completely uniform experimental parameters broadens the spectrum of self-organized patterns in oscillatory media. So far, mainly one particular state amongst these coexistence states, the chimera state, has received immense interest. Here, we demonstrate that this state is embedded in a series of related coexistence patterns, arguably showing a similar level of seemingly contradictory behavior in the coexisting regions. The wide variety of such patterns in the presence of a simple periodic global oscillation is remarkable. This conserved oscillation of the spatially averaged quantities seems to strongly promote the spontaneous emergence of the coexistence of different dynamical states on the electrode. In a wider sense, this can be seen as diversification of the dynamical behavior of a system with uniform parameters. The essential dynamical features responsible for this behavior remain unclear at this point. Considering our experiments, the assumption of a nonlinear global coupling as a necessary ingredient seems to be justified when considering the minority charge carrier dynamics in the silicon electrode. The lifetime of these charge carriers is several orders of magnitude shorter than any characteristic time scale of the observed oscillatory dynamics while the diffusion length is comparable to the system size within one order of magnitude. This should bring about a long-range if not effectively global coupling. In conclusion, the novel type of spatio-temporal patterns presented here sheds light on a number of fundamental questions concerning universal laws of pattern formation in oscillatory media, inviting future studies in both experiment and theory.

7 Summary & Outlook

If you try and take a cat apart to see how it works, the first thing you have on your hands is a non-working cat.

(Douglas Adams)

The photo-electrochemical dissolution of silicon exhibits a variety of spontaneous ordering phenomena, ranging from uniform oscillations to self-organized pattern formation of varying degrees of complexity [37, 39]. In this work we showed that this includes quite surprising phenomena as for example chimera states where the seemingly contradictory dynamics of perfect synchrony and incoherence coexist on the electrode [88, 89]. All these phenomena happen in the absence of any spatial variations in the parameters or initial conditions and pose a challenge to our intuition. They also reveal the silicon electrodissolution system as an interesting model system broadening the already wide scope of surprising phenomena arising in reaction-diffusion systems far from equilibrium [34, 36]. The analysis of these complex phenomena then poses questions on different levels and two questions stand out: First, why does the system oscillate at all and what is the underlying microscopical mechanism and, second, how do completely uniform parameters lead to complex patterns? The first question is treated in a more system specific way in this work while the tackling of the second one is aimed at showing in what way the system can be seen as a model for more general dynamical systems. Throughout this work the view that many phenomena are best described on a collective level rather than constructed from the individual behavior of the constituents is the guiding idea. Since silicon is an immensely important material such an understanding of the dynamics of its electrochemistry is also potentially meaningful for technological applications and might allow for new methods of controlling and manipulating the silicon surface.

The starting point for this work was next to the experimental setups which were mostly in place, studies on the uniform dynamics mostly of p-doped silicon from our and other groups and initial works on pattern formation from our group [38, 39, 40]. In these works the spatially uniform oscillations were already studied in some detail and a number of questions concerning the oscillations mechanism were raised and models proposed. A systematic approach to identify experimental tests for some of these models as well as the identification of necessary conditions for further, dynamical modeling attempts were thus the first central part of this work. The study of the formation of spatio-temporal patterns had only just started prior to this work and exclusively in our group. Consequently, the systematical study of these phenomena constituted the other central theme of the present work.

The spatially uniform oscillations are first investigated in a systematic manner. In this case the size of an external resistance R_{ext} connected in series with the working electrode is a central experimental parameter. Sinusoidal low amplitude current oscillations with and without a shoulder for relatively low values of R_{ext}, relaxational high amplitude current oscillations and chaotic oscillations for relatively high values of R_{ext} are identified as the prototypical oscillation forms. There is a strong indication that the high amplitude current oscillations and the chaotic oscillation are coexisting for the same experimental parameters and that only the

initial conditions decide which form is expressed. The four oscillation types show vastly differing behavior with the high amplitude current oscillations standing out in various respects. First, their temporally averaged electrode potential and current values show the strongest deviation from the quasi-steady state behavior of the electrodissolution system as identified by slow CV scans. Second, while for the low amplitude current oscillations the measured current and ellipsometric intensity are completely consistent with the assumption of both a constant etch rate and a uniform quality of the oxide layer in growth direction, this is not the case for the high amplitude current oscillations. Furthermore, the basic frequency is significantly higher for the high amplitude current oscillations than for all the others including the chaotic oscillations. In addition to this, the high amplitude current oscillations are accompanied by remarkably fine structured oscillations in the hydrogen production. This hydrogen production is furthermore found to be much lower on average than the corresponding quasi-stationary CV scans would suggest. Only with varying initial conditions, the R_{ext}-parameter regime can be fully captured and for very high values of R_{ext} the oscillation amplitude shrinks again and sinusoidal oscillations are again found. The overall picture is then that the high amplitude current oscillations are arising from Hopf-bifurcations for low as well as for high limiting values of R_{ext} and that the sinusoidal oscillations are thus the natural behavior of the system close to these bifurcations. The two limiting steady states are then found to be stable in the case of the low resistance limit and unstable in the case of the high resistance limit, a behavior in line with the quasi-stationary CV scans.

To study the mechanism which gives rise to the oscillations, first the electrode potential rather than the current is identified as an essential variable by a comparison with galvanostatic and mixed control measurements which all show an overall similar behavior. This means that the current oscillations found in the case of potentiostatic control with an external resistance are perhaps better viewed as electrode potential oscillations where the IR-drop across the external resistance is the means of the system to dynamically set its potential. The space charge layer of the electrode and variations of the etch rate due to changes in the chemical environment are identified as not being responsible for the oscillations leaving variations in oxide composition or structure as the places to look. For the study of these properties mostly etch-back measurements are employed which reveal a connection between the reaction valency, a property of the oxide formation, and the ellipsometric intensity, a property of the state of the oxide. This connection is then interpreted as a promising venue for further investigations of the oscillation mechanism. As opposed to the basic view of a continuous oscillatory medium presented here, the view of the oscillations arising from a synchronization effect of self-oscillating microdomains dominates the literature [76, 77, 78, 68]. Strong evidence that this view is not feasible to explain the oscillations is given by pointing out internal contradictions, most importantly the spatial uniformity of the oscillations on the measured scale down to ca. 10 µm regardless of the alleged degree of synchronization. This would mean that no local coupling component could be active in the system a peculiar assumption for an electrochemical system.

To broaden the scope of the experimental inquest a new measurement device is introduced which cuts off the current at a preset value j_{lim} and has otherwise no effect. This is then used to study the system under this restriction mimicking a similar current cut-off introduced by a limited illumination in the case of n-doped silicon samples. The latter has previously been identified as a necessary prerequisite for pattern formation. It turns out that the two methods of coupling share a variety of similarities and that the current limiter thereby becomes a valuable tool to study otherwise inaccessible properties of the silicon electrodissolution under limited illumination such as the relevant potential drops across the interface. Furthermore, the measurements substantiate the similarities between high amplitude potential oscillations

without a sharp cut-off and current limited oscillations leading to a unified picture of the basic oscillatory mechanism. In a next step, oscillations in presence of a sharp, current cut-off introduced by a limited illumination, especially those which show pattern formation, can then be incorporated in the picture gained by the study of uniform oscillations. Apart from the similarities between the two modes of current cut-off coupling there is also the important difference that the coupling range of an illumination induced coupling seems to have a local component while the range of the cut-off coupling induced by the external current limiter is purely global. This coincides with the patterns being found under the former but not the latter coupling. Nevertheless, there is strong evidence that the dynamical patterns themselves are brought about by the global rather than the local component of the coupling.

The patterns found in the oxide thickness distribution across the electrode surface are often accompanied by simple periodic oscillations of its spatial average. In this case a variety of patterns can be discerned many of which show the coexistence of different dynamical states at the electrode surface, amongst these two types of the already mentioned chimera state but also subharmonic cluster patterns. The patterns found experimentally are in good agreement with theoretical simulations which start from a very general assumption, namely that the system is in a certain sense close to the Hopf-bifurcation giving rise to the oscillations. Under these conditions a version of the Ginzburg-Landau equation fitting the coupling present in the experimental system is the appropriate normal form and thus suitable to identify the natural behavior of the oscillatory system from a nonlinear dynamical point of view. It is thus clearly shown that the patterns are genuinely dynamical phenomena and not brought about by irregularities in either the electrode or the experimental parameters. This finding is absolutely central to this work. In addition to this, further levels of complex structure formation are found involving variations of the spatially averaged oxide thickness. While these more complex structures can no longer be directly compared to the theoretical simulations a strong similarity in the behavior to both the less complex patterns and some theoretical simulations is still evident. This leads to the conclusion that these phenomena are dynamical in their nature as well and can again be incorporated in the overall picture of the system being an oscillatory medium showing various levels of complexity depending on their distance from equilibrium.

The overall task of gaining a full picture of the dynamics of the silicon electrodissolution system remains open and the two lines of inquiry pursued in this work can be followed further. The underlying mechanism of the uniform electrode potential oscillations remains central to this understanding. From the experimentalists point of view, a further inquest into the topic of multistability by varying the initial conditions systematically and also a broader application of etch-back measurements including the corresponding hydrogen evolution are highly desirable in this vein. This is a task for both uniform oscillations and oscillations accompanied by pattern formation. For the latter, the search for a link between experimental and theoretical parameters promises further insights into the dynamics of the system. It is also to be expected that future experimental studies reveal further layers of complexity in the pattern formation which have to be structured and categorized in light of the theoretical modeling efforts. Ideally, a model for the oscillations can then be used to refine the theoretical modeling, thus making a joining of the two main lines of inquiry presented here possible. The identification of a full dynamical model can then in turn be used to shed light on the broader class of systems for which the silicon electrodissolution can be seen as a model. The application of the intuition gained by the surprises the silicon electrodissolution system has proven to hold to other systems can thus be the contribution of this system to the understanding of dynamical systems in general. The role this understanding could play in the larger scientific effort can

be well summed up by the proverbial expression "*to not see the forest for the trees*" which warns us that the concentration on parts of a system might not tell us anything about the system at large. Quite the contrary, often the details of the parts of a system can only be understood by the role these parts play in the larger system as is the case for trees in the ecosystem forest.

List of Publications

[1] K. Krischer and K. Schönleber. *Physics of energy conversion.* de Gruyter, 2015.

[2] K. Schönleber and K. Krischer. High-amplitude versus low-amplitude current oscillations during the anodic oxidation of p-type silicon in fluoride containing electrolytes. *Chem. Phys. Chem.*, 13:2989, 2012.

[3] L. Schmidt, K. Schönleber, K. Krischer, and V. Garcia-Morales. Coexistence of synchrony and incoherence in oscillatory media under nonlinear global coupling. *Chaos*, 24(1):013102, 2014.

[4] K. Schönleber, C. Zensen, A. Heinrich, and K. Krischer. Pattern formation during the oscillatory photoelectrodissolution of n-type silicon: turbulence, clusters and chimeras. *New J. Phys.*, 16:063024, 2014.

[5] L. Schmidt, K. Schönleber, V. Garcia-Morales, and K. Krischer. *Engineering of chemical complexity 2 (World Scientific lecture notes in complex systems - Vol. 12)*, chapter 14, page 239. World Scientific, 2014.

[6] C. Zensen, K. Schönleber, F. Kemeth, and K. Krischer. A capacitance mediated positive differential resistance oscillator model for electrochemical systems involving a surface layer. *J. Phys. Chem. C*, 118:24407, 2014.

[7] Q. Li, K. Schönleber, P. Zeller, I. Höhlein, B. Rieger, J. Wintterlin, and K. Krischer. Activation of silicon surfaces for H_2 evolution by electrografting of pyridine molecules. *Surface Science*, 631:185, 2015.

Bibliography

[1] M. Ruse, *The Oxford Companion to Philosophy*, ch. reductionism, p. 750. Oxford University Press, 1995.

[2] P. W. Anderson, "More is different," *Science*, vol. 177, p. 393, 1972.

[3] C. R. Darwin and A. R. Wallace, "On the tendency of species to form varieties; and on the perpetuation of varieties and species by natural means of selection," *J. Proc. Linnean Society of London. Zoology*, vol. 3, p. 45, 1858.

[4] C. R. Darwin, *On the Origin of Species by Means of Natural Selection, or the Preservation of Favoured Races in the Struggle for Life.* John Murray (London), 1859.

[5] M. A. Nowak, *Evolutionary Dynamics.* Harvard University Press, 2006.

[6] M. Eigen and P. Schuster, "A principle of natural self-organization," *Naturwissenschaften*, vol. 64, p. 541, 1977.

[7] L. Campbell and W. Garnett, *The life of James Clerk Maxwell*, ch. 14, p. 434. Macmillian and Co. (London), 1882.

[8] R. M. May, "Simple mathematical model with very complicated dynamics," *Nature*, vol. 261, p. 459, 1976.

[9] H. Haken, *Advanced Synergetics.* Springer (Berlin, Heidelberg, New York, London, Paris, Tokyo), 1983.

[10] D. Kondepudi and I. Prigogine, *Modern Thermodynamics: from heat engines to dissipative structures.* John Wiley and Sons, inc., 1998.

[11] J. Argyris, G. Faust, M. Haase, and R. Friedrich, *Die Entstehung des Chaos.* Springer (Heidelberg, Dordrecht, London, New York), 2010.

[12] I. Prigogine, *The end of certainty.* Simon and Schuster, inc. (New York), 1997.

[13] M. M. Waldorp, *Complexity.* Simon and Schuster, inc. (New York), 1992.

[14] A. M. Turing, "The chemical basis of morphogenesis," *Phil. Trans. Roy. Soc. B*, vol. 237(641), p. 37, 1952.

[15] A. T. Winfree, "Varieties of spiral wave behavior: An experimentalists approach to the theory of excitable media," *Chaos*, vol. 1(3), p. 303, 1991.

[16] E. N. Lorenz, "Deterministic nonperiodic flow," *J. Atmos. Sci.*, vol. 20, p. 130, 1963.

[17] Y. Kuramoto, *Chemical oscillations, waves, and turbulence.* Dover Publications, Inc. (Mineola, New York), 1984.

[18] S. H. Strogatz, "From Kuramoto to Crawford: exploring the onset of synchronization in populations of coupled oscillators," *Physica D*, vol. 143, p. 1, 2000.

[19] S. H. Strogatz, *Sync.* Hyperion (New York), 2003.

[20] A. Gierer and H. Meinhardt, "A theory of biological pattern formation," *Kybernetik*, vol. 12, p. 30, 1972.

[21] J. Lechleiter, S. Girard, E. Peralta, and D. Clapham, "Spiral calcium wave propagation and annihilation in xenopus laevis oocytes," *Science*, vol. 252, p. 123, 1991.

[22] A. T. Winfree, "Electrical turbulence in three-dimensional heart muscle," *Science*, vol. 266, p. 1003, 1994.

[23] S. A. Gaeta, G. Bub, G. W. Abbott, and D. J. Christini, "Dynamical mechanism for subcellular alternans in cardiac myocytes," *Circ Res.*, vol. 105, p. 335, 2009.

[24] N. Tompkins, N. Lia, C. Girabawea, M. Heymann, B. Ermentrout, I. R. Epstein, and S. Fraden, "Testing Turings theory of morphogenesis in chemical cells," *Proc. Natl. Acad. Sci.*, vol. 111(12), p. 4397, 2014.

[25] B. Ermentrout, "Neural networks as spatio-temporal pattern-forming systems," *Rep. Prog. Phys.*, vol. 61, p. 353, 1998.

[26] M. E. Mann, J. Park, and R. S. Bradley, "Global interdecadal and century scale climate oscillations during the past five centuries," *Nature*, vol. 378, p. 266, 1995.

[27] A. L. Barabasi and R. Albert, "Emergence of scaling in random networks," *Science*, vol. 286, p. 509, 1999.

[28] S. N. Dorogovtsev, A. V. Goltsev, and J. F. F. Mendes, "Critical phenomena in complex networks," *Rev. Mod. Phys.*, vol. 80, p. 1275, 2008.

[29] S. V. Buldyrev, R. Parshani, G. Paul, H. E. Stanley, and S. Havlin, "Catastrophic cascade of failures in interdependent networks," *Nature*, vol. 464, p. 1025, 2010.

[30] M. Rohden, A. Sorge, M. Timme, and D. Witthaut, "Self-organized synchronization in decentralized power grids," *Phys. Rev. Lett.*, vol. 109, p. 064101, 2012.

[31] L. D. Landau, "On the problem of turbulence," *C.R.Acad.Sci.UESS*, vol. 44, p. 311, 1944.

[32] D. Ruelle and F. Takens, "On the nature of turbulence," *Commun. Math. Phys.*, vol. 20, p. 167, 1971.

[33] A. N. Zaikin and A. M. Zhabotinsky, "Concentration wave propagation in two-dimensional liquid-phase self-oscillating system," *Nature*, vol. 225, p. 535, 1970.

[34] I. R. Epstein and K. Showalter, "Nonlinear chemical dynamics: Oscillations, patterns, and chaos," *J. Phys. Chem.*, vol. 100, p. 13132, 1996.

[35] V. K. Vanag, L. Yang, M. Dolnik, A. M. Zhabotinsky, and I. R. Epstein, "Oscillatory cluster patterns in a homogeneous chemical system with global feedback," *Nature*, vol. 406, p. 389, 2000.

[36] G. Ertl, "Oscillatory kinetics and spatio-temporal selforganization in reactions at solid surfaces," *Science*, vol. 254, p. 1750, 1991.

[37] D. R. Turner, "Electropolishing silicon in hydrofluoric acid solutions," *J. Electrochem. Soc.*, vol. 105, pp. 402–408, 1958.

[38] X. G. Zhang, *Electrochemistry of silicon and its oxides.* Kluwer Academic, 2001.

[39] I. Miethe, V. Garcia-Morales, and K. Krischer, "Irregular subharmonic cluster patterns in an autonomous photoelectrochemical oscillator," *Phys. Rev. Lett.*, vol. 102, p. 194101, 2009.

[40] I. Miethe, *Spatio temporal pattern formation during the anodic electrodissolution of silicon in ammonium fluoride solution.* PhD thesis, Technische Universität München, 2010.

[41] A. Heinrich, "Mechanistische und dynamische Eigenschaften der Elektrodissolution von Silizium," Master's thesis, Technische Universität München, 2013.

[42] C. Zensen, "Mechanism of oscillation and spatio-temporal pattern formation in a semiconductor electrochemical system," Master's thesis, Technische Universität München, 2013.

[43] M. A. Green, "Intrinsic concentration, effective densities of states, and effective mass in silicon," *J. Appl. Phys.*, vol. 67(6), p. 2944, 1990.

[44] K. W. Frese, "Simple method for estimating energy levels of solids," *J. Vac. Sci. Technol.*, vol. 16(4), p. 1042, 1979.

[45] S. Trasatti, "The absolute electrode potential: an explanatory note," *Pure&Appl. Chem.*, vol. 58/7, p. 955, 1986.

[46] D. Tsiplakides, D. Archonta, and C. G. Vayenas, "Absolute potential measurements in solid and aqueous electrochemistry using two Kelvin probes and their implications for electrochemical promotion of catalysis," *Topics in Catalysis*, vol. 44, p. 469, 2007.

[47] R. Memming and G. Schwandt, "Anodic dissolution of silicon in hydrofluoric acid solutions," *Surface Science*, vol. 4, p. 109, 1966.

[48] D. J. Blackwood, A. Borazio, R. Greef, L. M. Peter, and J. Stumper, "Electrochemical and optical studies of silicon dissolution in ammonium fluoride solutions," *Electrochimica Acta*, vol. 37 (5), p. 898, 1992.

[49] H. Hasegawa, S. Arimoto, J. Nanjo, H. Yamamoto, and H. Ohno, "Anodic oxidation of hydrogenated amorphous silicon and properties of oxide," *J. Electrochem. Soc.*, vol. 135(2), p. 424, 1988.

[50] M. Matsumura and S. R. Morrison, "Anodic Properties of n-Si and n-Ge electrodes in HF solutions under illumination and in the dark," *J. Electroanal. Chem.*, vol. 147, p. 157, 1983.

[51] S. Cattarin, I. Frateur, M. Musiani, and B. Triboullet, "Electrodissolution of p-Si in acidic fluoride media," *J. Electrochem. Soc.*, vol. 147, p. 3277, 2000.

[52] J. N. Chazalviel, M. Etman, and F. Ozanam, "A voltammetric study of the anodic dissolution of p-Si in fluoride electrolytes," *J. Electroanal. Chem.*, vol. 297, p. 533, 1991.

[53] H. J. Lewerenz and M. Aggour, "On the origin of photocurrent oscillation at Si electrodes," *J. Electroanal. Chem.*, vol. 351, no. 1-2, pp. 159–168, 1993.

[54] A. J. Bard and L. R. Faulkner, *Electrochemical Methods - Fundamentals and Applications.* John Wiley & Sons, Inc., 2001.

[55] F. Linke and R. Merkel, "Quantitative ellipsometric microscopy at the glass water interface," *New J. Phys.*, vol. 7 (128), p. 1, 2005.

[56] J. R. Chelikowsky and M. L. Cohen, "Nonlocal pseudopotential calculations for the electronic structure of eleven diamond and zinc-blende semiconductors," *Phys. Rev. B*, vol. 14(2), p. 556, 1976.

[57] Ioffe Physico-Technical Institute, http://www.ioffe.rssi.ru/SVA/NSM/Semicond/, "NSM Archive: Physical properties of semiconductors."

[58] D. R. Lide (Editor), *CRC Handbook of Chemistry and Physics, Internet Version 2005.* CRC Press, Boca Raton, FL, 2005.

[59] M. J. Eddowes, "Anodic dissolution of p-type and n-type silicon - kinetic study of the chemical mechanism," *J. Electroanal. Chem.*, vol. 280 (2), p. 297, 1990.

[60] J. Stumper, R. Greef, and L. M. Peter, "Current oscillations during anodic dissolution of p-Si in ammonium fluoride: an investigation using ring disc voltammetry and ellipsometry," *J. Electroanal. Chem.*, vol. 310, p. 445, 1991.

[61] J. N. Chazalviel, F. Ozanam, M. Etman, F. Paolucci, L. M. Peter, and J. Stumper, "The p-Si/fluoride interface in the anodic region: Damped and/or sustained oscillations," *J. Electroanal. Chem.*, vol. 327, no. 1-2, pp. 343–349, 1992.

[62] F. Paolucci, L. M. Peter, and J. Stumper, "Wavelength-dependent photocurrent multiplication during the anodic dissolution of n-Si in ammonium fluoride solutions," *J. Electroanal. Chem.*, vol. 341, p. 165, 1992.

[63] I. Miethe and K. Krischer, "Ellipsomicroscopic studies of the anodic oxidation of p-type silicon in fluoride containing electrolytes during current oscillations," *J. Electroanal. Chem.*, vol. 666, p. 1, 2012.

[64] M. Aggour, M. Giersig, and H. J. Lewerenz, "Interface condition of n-Si(111) during photocurrent oscillations in NH_4F solutions," *J. Electroanal. Chem.*, vol. 383, no. 1-2, pp. 67–74, 1995.

[65] S. Böhm, L. M. Peter, G. Schlichthörl, and R. Greef, "Ellipsometric and microwave reflectivity studies of current oscillations during anodic dissolution of p-Si in fluoride solutions," *J. Electroanal. Chem.*, vol. 500, p. 178, 2001.

[66] J. N. Chazalviel, C. da Fonseca, and F. Ozanam, "In situ infrared study of the oscillating anodic dissolution of silicon in fluoride electrolytes," *J. Electrochem. Soc.*, vol. 145 (3), p. 964, 1998.

[67] F. Yahyaoui, T. Dittrich, M. Aggour, J. N. Chazalviel, F. Ozanam, and J. Rappich, "Etch rates of anodic silicon oxides in dilute fluoride solutions," *J. Electrochem. Soc.*, vol. 150, no. 5, p. B205, 2003.

[68] F. Blaffart, Q. V. Overmeere, F. V. Wonterghem, and J. Proost, "In situ monitoring of electrochemical oscillations during the transition between dense and porous anodic silica formation," *J. Electrochem. Soc.*, vol. 161(14), p. H874, 2014.

[69] V. Lehmann, "On the origin of electrochemical oscillations at silicon electrodes," *J. Electrochem. Soc.*, vol. 143, no. 4, pp. 1313–1318, 1996.

[70] J. Proost, F. Blaffart, S. Turner, and H. Idrissi, "On the origin of damped electrochemical oscillations at silicon anodes (revisited)," *Chem. Phys. Chem.*, vol. 15, p. 3116, 2014.

[71] J. Grzanna, H. Jungblut, and H. J. Lewerenz, "A model for electrochemical oscillations at the Si vertical bar electrolyte contact Part I. Theoretical development," *J. Electroanal. Chem.*, vol. 486, no. 2, pp. 181–189, 2000.

[72] J. Grzanna, H. Jungblut, and H. J. Lewerenz, "A model for electrochemical oscillations at the Si vertical bar electrolyte contact Part II. Simulations and experimental results," *J. Electroanal. Chem.*, vol. 486, no. 2, pp. 190–203, 2000.

[73] E. Foca, J. Carstensen, and H. Föll, "Modelling electrochemical current and potential oscillations at the Si electrode," *J. Electroanal. Chem.*, vol. 603, no. 2, pp. 175–202, 2007.

[74] J. Carstensen, R. Prange, and H. Föll, "A model for current-voltage oscillations at the silicon electrode and comparison with experimental results," *J. Electrochem. Soc.*, vol. 146/3, p. 1134, 1999.

[75] J. N. Chazalviel, "Ionic processes through the interfacial oxide in the anodic dissolution of silicon," *Electrochim. Acta*, vol. 37, p. 865, 1992.

[76] F. Ozanam, J. N. Chazalviel, A. Radi, and M. Etman, "Resonant and nonresonant behavior of the anodic dissolution of silicon in fluoride media: An impedance Study," *J. Electrochem. Soc.*, vol. 139/9, p. 2491, 1992.

[77] J. N. Chazalviel and F. Ozanam, "A theory for the resonant response of an electrochemical system: Self-oscillating domains, hidden oscillation, and ssynchronization impedance," *J. Electrochem. Soc.*, vol. 139/9, p. 2501, 1992.

[78] J. Carstensen, R. Prange, G. S. Popkirov, and H. Föll, "A model for current oscillations in the si-hf system based on a quantitative analysis of current transients," *Appl. Phys. A*, vol. 67, p. 459, 1998.

[79] S. H. Strogatz, *Nonlinear Dynamics and Chaos.* Perseus Books Publishing, LLC, 2000.

[80] S. Danö, P. G. Sörensen, and F. Hynne, "Sustained oscillations in living cells," *Nature*, vol. 402, p. 320, 1999.

[81] S. De Monte, F. d Ovidio, S. Danö, and P. G. Sörensen, "Dynamical quorum sensing: Population density encoded in cellular dynamics," *Proc. Natl. Acad. Sci.*, vol. 104(47), p. 18377, 2007.

[82] A. F. Taylor, M. R. Tinsley, F. Wang, Z. Huang, and K. Showalter, "Dynamical quorum sensing and synchronization in large populations of chemical oscillators," *Science*, vol. 323, p. 614, 2009.

[83] E. Mitterreiter, "Characterization and parameter dependence of current spikes occuring during the illumination-limited, oscillatory electrodissolution of n-type silicon." Bachelor Thesis, Technische Universität München, 2013.

[84] H. J. Lewerenz, J. Stumper, and L. M.Peter, "Deconvolution of charge injection steps in quantum yield multiplication on silicon," *Phys. Rev. Lett.*, vol. 61 (17), p. 1989, 1988.

[85] K. Krischer, N. Mazouz, and G. Flätgen, "Pattern formation in globally coupled electrochemical systems with s-shaped current-potential curve," *J. Phys. Chem. B*, vol. 104, p. 7545, 2000.

[86] N. Mazouz, K. Krischer, and I. G. Kevrekidis, "The impact of the operation mode on pattern formation in electrode reactions," *J. Electrochem. Soc.*, vol. 145(7), p. 2404, 1998.

[87] A. Mikhailov, *Foundations of Synergetics 1.* Springer (Berlin, Heidelberg, New York), 1994.

[88] Y. Kuramoto and D. Battogtokh, "Coexistence of coherence and incoherence in nonlocally coupled phase oscillators," *Nonlin. Phenom. in Complex Syst.*, vol. 5, p. 380, 2002.

[89] D. M. Abrams and S. H. Strogatz, "Chimera states for coupled oscillators," *Phys. Rev. Lett.*, vol. 93, p. 174102, 2004.

[90] S. Arimoto, H. A. Hasegawa, H. Yamamoto, and H. Ohno, "Anodic oxidation for enhancement of fabrication yield and efficiency of amorphous silicon solar cells," *J. Electrochem. Soc.*, vol. 135/2, p. 431, 1988.

[91] M. Wiegand, "Selbstorganisation und Wellenerscheinungen während des Elektropolierens von Si-Wafern." Bachelor Thesis, Technische Universität München, 2012.

[92] L. Schmidt, *Oscillatory systems with nonlinear global coupling: from clusters to chimeras.* PhD thesis, Technische Universität München, 2015.

[93] V. Garcia-Morales, A. Orlov, and K. Krischer, "Subharmonic phase clusters in the complex Ginzburg-Landau equation with nonlinear global coupling," *Phys. Rev. E*, vol. 82, p. 065202, 2010.

[94] A. M. Hagerstrom, T. E. Murphy, R. Roy, P. Hövel, I. Omelchenko, and E. Schöll, "Experimental observation of chimeras in coupled-map lattices," *Nature Phys.*, vol. 8, p. 658, 2012.

[95] M. R. Tinsley, N. Simbarashe, and K. Showalter, "Chimera and phase-cluster states in populations of coupled chemical oscillators," *Nature Phys.*, vol. 8, p. 662, 2012.

[96] E. A. Martens, S. Thutupalli, A. Fourrire, and O. Hallatschek, "Chimera states in mechanical oscillator networks," *Proc. Natl. Acad. Sci.*, vol. 110(26), p. 10563, 2013.

[97] M. Wickramasinghe and I. Z. Kiss, "Spatially organized dynamical states in chemical oscillator networks: Synchronization, dynamical differentiation, and chimera patterns," *PLoS One*, vol. 8, p. e80586, 2013.

[98] E. A. Viktorov, T. Habruseva, S. P. Hegarty, G. Huyet, and B. Kelleher, "Coherence and incoherence in an optical comb," *Phys. Rev. Lett.*, vol. 112, p. 224101, 2014.

[99] M. J. Panaggio and D. M. Abrams, "Chimera states: coexistence of coherence and incoherence in networks of coupled oscillators," *Nonlinearity*, vol. 28, p. R67, 2015.

[100] A. Smart, "Exotic chimera dynamics glimpsed in experiments," *Physics Today*, vol. 65(10), p. 17, 2012.

[101] I. S. Aranson and L. Kramer, "The world of the complex Ginzburg-Landau equation," *Rev. Mod. Phys.*, vol. 74, p. 99, 2002.

[102] V. Garcia-Morales and K. Krischer, "The complex Ginzburg-Landau equation: an introduction," *Contemporary Physics*, vol. 53(2), p. 79, 2012.

[103] A. Yeldesbay, A. Pikovsky, and M. Rosenblum, "Chimeralike states in an ensemble of globally coupled oscillators," *Phys. Rev. Lett.*, vol. 112, p. 144103, 2014.

[104] L. Schmidt and K. Krischer, "Clustering as a prerequisite for chimera states in globally coupled systems," *Phys. Rev. Lett.*, vol. 114, p. 034101, 2015.

[105] S. W. Haugland, L. Schmidt, and K. Krischer, "Self-organized alternating chimera states in oscillatory media," *Scientific Reports*, vol. 5, p. 9883, 2015.